SLAC-PUB-1694

INCLUSIVE PHOTOPRODUCTION OF CHARGED PARTICLES IN THE FORWARD HEMISPHERE

A. M. Boyarski *et al.*
Stanford Linear Accelerator Center
Stanford University, Stanford, California 94305

ERRATA

Page 58	"$\mu=\sqrt{p^2+m^2}$" should read "$\mu=\sqrt{p_\perp^2+m^2}$".
TABLE I.	For references 5,10,11, and 14 the lower limit of x should be -1. rather than 1.
TABLE X.	The units for parameters A and B should be $\mu b/(GeV)^2$ rather than $\mu b/GeV$.
Fig 15 caption	"p to p ratio" should read "p to $\bar{p}$ ratio".

January 1976

SLAC-PUB-1694
December 1975
(T/E)

INCLUSIVE PHOTOPRODUCTION OF CHARGED PARTICLES IN THE FORWARD HEMISPHERE*

A. M. Boyarski, D. H. Coward, S. D. Ecklund,**
B. Richter, D. J. Sherden, R. H. Siemann,***
and C. K. Sinclair

Stanford Linear Accelerator Center
Stanford University, Stanford, California 94305

Abstract:

We report measurements of the invariant cross section in the forward hemisphere for inclusive photoproduction of $\pi^{\pm}$, $K^{\pm}$, p, and $\bar{p}$ from hydrogen and deuterium with an incident photon energy of 18 GeV. A small amount of data was also taken at incident energies of 9 and 13 GeV. The measurements were made using the SLAC 20 GeV/c spectrometer, and a bremsstrahlung subtraction technique was used to obtain the cross sections at the specified incident energy. The data are compared with those from lower energy experiments and interpreted within the context of the Mueller-Regge model and the constituent interchange model.

---

* Work supported by the U. S. Energy Research and Development Administration

** Present address: Fermi National Laboratory, Batavia, Ill. 60510

*** Present address: Cornell University, Ithaca, N.Y. 14850

(Submitted to Phys. Rev.)

I. INTRODUCTION

The study of inclusive reactions has been of considerable interest for several years[1] and has received added impetus from the large center-of-mass energies now available at the ISR and FNAL.[2] Features predicted from several theoretical approaches, such as the asymptotic scaling of the invariant cross section with energy, the development of a plateau in the invariant cross section at small c.m. rapidity, and diffractive scattering consistent with triple-Regge models, at least qualitatively, have been verified. Furthermore, some unexpected features, such as the large cross sections at large transverse momentum, have been observed. This behavior at large transverse momentum is of considerable interest from the point of view of parton models.[3]

At lower energies it is of interest to obtain more detailed measurements of inclusive reactions to test theoretical models on a more quantitative basis. The s dependence and approach to scaling can be studied within the Mueller-Regge framework.[4] Relative yields of different particles and reactions can be used to study factorization, and inclusive sum rules offer some hope of correlating different coupling constants. At large values of transverse momentum one can explore a domain in which p/p_{max} is close to unity, where, at high energies, cross sections are prohibitively small.

Exclusive photoproduction processes have been found to be

hadronic in nature, and inclusive photoproduction data[5] in the target fragmentation region have been successfully related through factorization to the equivalent $K^{\pm}$ reactions.[6,7] It is then of interest to compare inclusive photoproduction processes in the photon fragmentation region with hadron induced reactions. Through charge symmetry, the Mueller-Regge model predicts that particle and antiparticle yields asymptotically should be equal in the photon fragmentation region. Thus the approach to asymptotic behavior can be studied in a manner relatively free of systematic errors by measuring the relative yields of particle and antiparticle. At large transverse momentum, important power law differences in the $p_{\perp}$ dependence between photon, meson, and baryon induced reactions are predicted by parton models. Such differences have already been observed in large angle exclusive processes.[8] In addition to its importance for comparison with hadron induced reactions, photoproduction is the $q^2=0$ limit of electroproduction, and thus provides an important tie point for electroproduction reactions. A summary of previous inclusive photoproduction experiments is given in Table I.[5,9-16]

In this paper we present the results of an experiment to measure inclusive photoproduction of $\pi^{\pm}$, $K^{\pm}$, p, and $\bar{p}$ from hydrogen and deuterium in the forward hemisphere for 18 GeV incident photons.[9] A small amount of data was also taken at 9 and 13 GeV. The deuterium data allow us to test the prediction common to several theoretical approaches that the

structure functions in the photon fragmentation region should be independent of target particle. This is of particular interest for K^- and $\bar{p}$ photoproduction, where, in the Mueller-Regge model, non-Pomeron exchange should be suppressed.

We describe the details of the experiment in Section II, and in Section III describe the analysis of and corrections to the data. The results and a qualitative description of the data are presented in Section IV, and an interpretation of the results is given Section V.

II. DESCRIPTION OF THE EXPERIMENT

The experiment used the SLAC 20 GeV/c spectrometer to momentum analyze, detect, and identify charged particles photoproduced by a bremsstrahlung beam incident on liquid hydrogen or deuterium targets.

A. The Photon Beam

A schematic of the experimental layout is shown in Fig. 1. The SLAC electron beam was incident on a .0285 radiation length aluminum radiator and deflected vertically out of the beam line by four bending magnets. The undeflected bremsstrahlung beam passed through two sets of collimators, each followed by a sweeping magnet, and struck a liquid hydrogen or deuterium target 51 m downstream of the radiator. The combination of electron beam optics, multiple scattering

in the radiator, and the first collimator size produced a beam spot size of $\simeq$ 2x2 cm at the target. The second set of collimators was shadowed by the first and did not intercept the primary beam. For the 2.85% radiator used, typically 2.3% of the electron beam energy was transmitted to the target in the bremsstrahlung beam, resulting in beams of up to 10^{10} equivalent quanta per 1.6 μsec long SLAC pulse (at 180 pulses/sec).

Two pairs of correction magnets upstream of the radiator were used to properly steer the beam to the target. The electron beam position just downstream of the radiator was monitored with a helium-filled Cerenkov monitor[17] viewed with a television camera. The photon beam position just upstream of the target could be monitored with removable zinc sulfide screens mounted behind variable thicknesses of copper and viewed with a television camera.

Because a bremsstrahlung beam has a continuous energy spectrum, it was not possible to directly measure cross sections for a fixed photon energy. Consequently data were taken with the electron beam set at energies above and below the desired photon energy. To the extent that the bremsstrahlung beam had a 1/k spectrum, the number of incident photons below the endpoint energy of the lower energy beam cancelled for the two beams. Hence by subtracting the yield of the lower energy beam from that of the higher energy beam, one obtained a yield due to photons of energies between the

two endpoints. A more realistic calculation of the effective beam spectrum after subtraction is shown in Fig. 2. For most of the 18 GeV data, endpoint energies of 17 vs 19 GeV were used to make the bremsstrahlung subtraction. At very low momenta, however, the subtracted yields were only a small fraction of the unsubtracted yields, so endpoints of 16 vs 20 GeV were used to enhance the subtracted effect. For several data points, endpoint energies of both 17 vs 19 GeV and 16 vs 20 GeV were used to check for systematic differences between the two. The 9 and 13 GeV data were taken with 8 vs 10 GeV and 12 vs 14 GeV endpoints, respectively.

At the lowest particle momenta measured, the subtracted cross sections were $\simeq 10\%$ of the unsubtracted cross sections. Hence small systematic differences between the measurements at the two energies could cause sizeable errors in the subtracted results. To minimize time-dependent systematic errors, it was therefore highly desirable to be able to switch frequently from one energy to the other. To accomplish this, two complete pulse patterns,[17] one for each of the desired energies, for all of the pulsed components of the accelerator (e.g. klystrons and pulsed steering magnets) were prepared. One of these patterns was always suppressed. The energy changes were controlled by the XDS 9300 computer used online in the experiment,[18] which initiated the following sequence of events: (i) both trigger patterns were suppressed to stop beam acceleration entirely; (ii) through a link to a remote XDS 925

computer,[17] the currents in the beam switchyard magnets were changed to values appropriate to the new energy; (iii) a rotating flip coil was read to check the value of the momentum defining magnets in the beam switchyard; (iv) the trigger pattern for the new energy was unsuppressed, delivering beam at the new energy. Approximately 40 seconds were required to complete the energy change.

The electron beam current was monitored by a precision toroid[19] located just upstream of the radiator. The photon beam was monitored by a helium filled Cerenkov monitor[20] and two hydrogen filled ion chambers of different thicknesses upstream of the target. A small secondary emission quantameter (SEQ)[20] located downstream of the target but upstream of the spectrometer served both as the primary photon beam monitor and as the beam dump.

B. Targets

The target assembly consisted of long (30.5 cm) and short (15.2 cm) hydrogen, deuterium, and dummy cells, as well as two "no target" positions, all contained within a common vacuum chamber. The long and short cells were used to check for absorption and double scattering effects. All cells were cylindrical (with axes along the beam direction) with a diameter of 8.9 cm. The mylar cylinder walls were 0.25 mm thick, while the aluminum endcaps were 0.13 mm thick. The scattering chamber had aluminum entrance and exit windows of

0.10 and 0.20 mm respectively. Forced circulation was used in the liquid targets to maintain stable target temperatures.

The cells were arranged in two vertical arrays, with the axes of one array perpendicular to those of the other. The entire assembly could be rotated about a vertical axis upstream of the targets to position one of the two arrays along the beam line. The assembly could be translated vertically to select one of four positions within the array. The target motion could be controlled by the computer to facilitate rapid target changes. The computer also read hydrogen vapor pressure thermometers used to monitor the target temperature.

C. The 20 GeV/c Spectrometer

The SLAC 20 GeV/c spectrometer[21] is shown in Fig. 3, and its first-order optics are illustrated in Fig. 4. Important parameters of the spectrometer are listed in Table II. Line-to-point focusing in the horizontal plane is used to measure the horizontal production angle, and point-to-point focusing with momentum dispersion in the vertical plane is used to measure the momentum of the detected particle. Momentum dispersion is provided by four bending magnets giving a total bend of 20.8°. Focusing is obtained from four quadrupoles, and three sextupoles are used to raise the momentum focal plane from 3° to 42° relative to the central ray. The optics in the vertical plane provides a crossover

midway up the spectrometer, so that the beam emerges from the spectrometer parallel to the floor.

The spectrometer rolls about the target on four concentric rails, and can be remotely driven to angles as large as 22°. The size and location of the SEQ limited the smallest spectrometer angle to $\simeq 1^{o}$. Detectors for the experiment were located in a concrete hut with walls 1.8 - 3.5 m thick mounted at the end of the spectrometer. The magnet currents were controlled by the computer and monitored by precision shunts and transductors for each magnet. When changing the magnet polarity of the spectrometer, the magnets were not degaussed. However, a fixed hysterisis pattern was followed and a small correction was applied to obtain the correct momentum.

D. Detection Scheme

The particle detection scheme used was similar to that of previous photoproduction experiments[22] with the 20 GeV/c spectrometer, and is shown schematically in Fig. 5. Incoming particles were detected by three scintillation trigger counters and their trajectories within the spectrometer acceptance were localized by two pairs of crossed scintillation counter hodoscopes. Two smaller "aperture" scintillation counters were used in determining the spectrometer acceptance. Particle identification was provided by a nitrogen filled threshold Cerenkov counter, a freon-13 differential Cerenkov counter, a lead-lucite shower counter,

and a scintillation counter - iron range telescope.

The momentum and angular resolution provided by the hodoscopes was not necessary to the experiment, and the results presented for each spectrometer setting are summed over all hodoscope elements. The hodoscopes were used to define the acceptance of the spectrometer and to obtain several corrections to the data. By rejecting events with multiple tracks in the hodoscopes, unambiguous particle identification in the Cerenkov counters was obtained. Additionally, only a limited portion of the hodoscope acceptance was used in order to reduce the divergence of particle trajectories, thus producing cleaner particle separation in the differential counter.

The threshold Cerenkov counter, used to identify pions, had a path length of 200 cm of nitrogen. Cerenkov light was deflected 90° by a plane aluminized mirror through an aluminized conical light guide to a single photomultiplier. The counter was operated at pressures ranging from 1.5 to 6.5 atm to give a pion Cerenkov angle of 28 mrad.

The differential Cerenkov counter, used to distinguish kaons and protons, had 0.95 cm aluminum entrance and exit windows and a path length of 231 cm of freon 13. Cerenkov light was focused by a spherical mirror onto two sets of photomultipliers. The inner "ring" consisted of two photomultipliers accepting Cerenkov angles between 40 and 60 mrad. The outer ring used four photomultipliers to accept

light with Cerenkov angles between 60 and 96 mrad. For most of the data taking the pressure was set to give a kaon Cerenkov angle of 50 mrad. Since the relative Cerenkov angle for pions and kaons is momentum dependent, this resulted in a pion Cerenkov angle of greater than 96 mrad for momenta below 5.8 GeV/c. At momenta greater than 9.7 GeV/c, corresponding to a pion Cerenkov angle of 70 mrad, the pressure was increased to give a kaon Cerenkov angle of slightly greater than 50 mrad to increase pion rejection. Pressures used in the differential counter ranged from 2.5 to 19 atm. The pressure and temperature of both the threshold and the differential Cerenkov counters were monitored remotely by the computer.

The 17.4 radiation length shower counter, used to veto electrons, consisted of 16 slabs of 1.27 cm UVT lucite interspersed with 0.64 cm lead slabs. Cerenkov light from the lucite was detected by a single Amperex 60AVP photomultiplier.

The range telescope, used to veto muons, consisted of nine 1.27 cm scintillation counters, interspersed with a total of seven 26 cm thick blocks of iron, giving a total thickness of 16 collision lengths. The first range counter was placed between the differential Cerenkov counter and the shower counter, and was used, in effect, as a fourth trigger counter. In addition to the shower counter there were 8 cm of tungsten between the first and second range counters.

E. Electronics and Triggering Scheme

Because of the high triggering rates obtained for much of the data, combined with the short 1.6 μsec pulse length of the SLAC beam, and because of the high ratio of photoproduced pions to other particles, it was desirable to use a triggering scheme in which pion events could be read by the computer on a sampling basis only, but in which kaon or proton events were read with as loose a trigger as possible. Therefore, the fast electronic logic was set up to measure pion cross sections using scaler information alone ("hardware yields"), while the kaon, proton, and sampled pion cross sections were obtained using the more detailed event information available to the computer ("software yields"). For the cross sections presented in this paper, all pion results were obtained from the hardware yields, while the kaon and proton yields were obtained from the software yields.

The hardware pion identification consisted of a coincidence between the three trigger counters, the threshold Cerenkov counter, and the first range counter. Additionally, events were vetoed by a signal from the last range counter or a large signal from the shower counter. Signals from the shower counter passed through a variable attenuator before entering the discriminator so that the effective discriminator threshold could be varied as a function of spectrometer momentum to match the expected electron shower pulse height.

The event trigger to the computer consisted simply of a

coincidence between the three trigger counters, which could be vetoed by some variable fraction of the hardware pion signals. For each triggered event the computer read the pulse heights of the threshold counter, the shower counter, and each of the photomultipliers of the differential counter. The hodoscope and range telescope information, as well as a variety of signals from the fast electronics logic, were read through gated latches.

F. Data Taking Procedure

For virtually all points data were taken with the short hydrogen and dummy targets for both positive and negative particles. In most cases data were also taken with the short deuterium target, and for a smaller number of points data were taken with the long targets. Targets and beam energy were cycled as frequently as was practical. At least two runs were taken for each target and energy setting, usually separated by one or more target or energy changes, thus allowing one to monitor the short term reproducibility of the measurements. As a check on the long term reproducibility of the measurements, several points were repeated at different times during the experiment.

In addition to reading event data and performing many of the frequently exercised control functions of the experiment, the computer read and logged the beam monitors, scalers, and a variety of slit settings, magnet settings, and status

indicators. Between 20 and 100% of the events (depending upon counting rate) were analyzed online to produce preliminary cross sections and a variety of diagnostic displays and printouts.

III. DATA REDUCTION

A list of corrections and estimated uncertainties in the data is given in Table III. In the following sections these corrections are discussed in detail. It is important to distinguish between uncertainties which are applied as a percentage of the unsubtracted cross sections and those which are applied as a percentage of the subtracted cross sections, since the former have a much larger effect on the final (subtracted) answers. We also distinguish between three general classes of uncertainties. We refer to errors which are not correlated from point to point as random errors. Those errors which vary in a systematic way with the kinematics are referred to as systematic errors, while those which are the same for all points are referred to as normalization errors. For each point, uncertainties from different sources within each class have been added in quadrature.

A. Beam Normalization

1. SEQ calibration: The SEQ used as the primary beam monitor in this experiment was frequently calibrated against two silver calorimeters[20] using the Cerenkov monitor as a transfer

standard. Consistent results using the two calorimeters were obtained early in the run, and use of the second was subsequently dropped.

Because of its small size, the SEQ is not quite a total absorption device, and consequently its calibration constant has some (0.7%/GeV) energy dependence. This energy dependence was found to be consistent with a linear behavior over the entire 8 to 20 GeV energy range used by this experiment.

The calibration constant was also observed to have a slow ($\simeq$1%/month) time dependence which could be adequately parametrized by two linear functions of run number. With the exception of runs taken very early in the experiment (which were erratic for a known reason), the calibrated values had an rms deviation of 0.5% from the assumed form. This error is included in the random errors as a percentage of the subtracted cross sections. Similarly the energy dependence of the calibration constant showed an rms deviation of 0.1%/GeV, which has been included in the systematic errors as a percentage of the unsubtracted cross sections. Slightly larger errors were assigned to the early runs to account for the erratic behavior of the SEQ.

No dependence of the SEQ calibration constant upon beam power was observed, although the range over which the calorimeter could conveniently be operated was smaller than the range over which data was actually taken.

2. Calorimeter calibration: The calorimeters were calibrated using internal electric heaters to deposit a known amount of energy. A 1-2% correction based on shower calculations was applied to account for shower leakage. SEQ calibrations against the two calorimeters agreed to 0.5%, and heater calibrations of the same calorimeter were consistent to 0.2%. However, an earlier calibration of the calorimeters against a Faraday cup, using an electron beam, gave a 2% discrepancy between beam and heater calibrations.[20] The heater calibration value obtained in this experiment was also 1% different from the original value. We have assigned a 3% normalization error to the overall calorimeter calibration.

3. Bremsstrahlung correction: To the extent that the bremsstrahlung spectrum deviates from a 1/k behavior (where k is the photon energy), the cancellation of lower energy primary photons is not exact. To correct for this one must know the shape of the bremsstrahlung spectrum, which is readily calculated,[23] and the energy dependence of the cross section for fixed spectrometer setting. As will be discussed later, an empirical fit was made to the 18 GeV results as a function of the transverse momentum $p_\perp$, and a modified Feynman scaling variable[24] $x' = p^*_\parallel / p^*_{\parallel\,max}(p_\perp)$. Here $p^*_\parallel$ is the c.m. longitudinal momentum of the observed particle, and $p^*_{\parallel\,max}$ is its maximum kinematically allowed value. To the extent that Feynman scaling is valid, the invariant cross section is a

function of x' and $p_\perp$, independent of incident energy. Thus the fits to the 18 GeV subtracted data could be used to roughly calculate the energy dependence of the laboratory cross section. (Note that for fixed laboratory kinematics, the effect of decreasing k is to increase x', leaving $p_\perp$ fixed.) In this way a correction was made for low energy photons and for the variation in kinematics at energies between the two endpoints. (Thus the final cross sections are always quoted for the nominal energy and its associated c.m. kinematics.)

As will be seen, Feynman scaling is a poor approximation at large transverse momentum. A measure of this inadequacy could be obtained by using the fits to the subtracted 18 GeV data to calculate the unsubtracted yields, assuming Feynman scaling. The correction for low energy photons was then modified by the ratio of the observed to calculated unsubtracted yield. At large transverse momenta this ratio was as small as 0.5. For the $\gamma p \to p\ X$ data, the assumption of Feynman scaling proved to be a particularly poor approximation, and better results were obtained by assuming scaling in $p_\parallel$ in the laboratory system, with a kinematic cut-off. Thus the energy dependence of this reaction was calculated using the form

$$E\frac{d^3\sigma}{dp^3}(p_{\parallel lab}, p_\perp, k) = E\frac{d^3\sigma}{dp^3}(p_{\parallel lab}, p_\perp, 18)\frac{(1 - e^{-4.33[1-x'(k)]^2})}{(1 - e^{-4.33[1-x'(18)]^2})}$$

In spite of the somewhat <u>ad hoc</u> nature of the kinematic

cut-off term, the use of this form gave better results in calculating the unsubtracted yields than were obtained for the pion and kaon yields.

The bremsstrahlung correction ranged from 0 to 25% of the subtracted yields, and three terms were added in quadrature to the systematic error: (i.) 1% of the subtracted yield, (ii.) 20% of the bremsstrahlung correction, and (iii.) 100% of the correction for deviation from Feynman scaling. The uncertainties thus obtained ranged from 1 to 10% of the subtracted yields. An additional 3% of the subtracted yields has been included in the normalization error to account for collimation effects and uncertainties in the bremsstrahlung calculation.

B. Target Corrections

1. Target length: Target cell lengths were measured at room temperature, and a correction of 0.4% was applied to the data to account for shrinkage in going to liquid hydrogen temperatures.

2. Target density: Target temperatures were monitored by hydrogen vapor pressure thermometers in thermal contact with the liquid cells. The temperature of the targets over the entire experiment remained stable to $\pm 0.1^{\circ}$K, corresponding to a density change of ±0.2%, which has been included in the random error as a percentage of the subtracted yields. An additional 0.7% of the subtracted yields has been included in

the normalization error to account for the uncertainties in the pressure calibration and conversion from pressure to density.

3. Target contamination: Gas samples from the target cells were taken periodically and analyzed with a mass spectrometer. The only significant finding was a hydrogen contamination of the deuterium samples which varied between 0.2 and 1.6% by volume. We have applied a 0.4±0.3% correction to the deuterium data to account for this, where the uncertainty has been applied to the random error as a percentage of the subtracted cross sections.

4. Dummy target correction: When using the short targets, dummy target data were always taken, resulting in typical corrections of ≃10%. Long dummy target data were not always taken, and a parametrization of the ratio of long to short dummy target rates as a function of angle was used for points in which direct measurements were not made. (Note that this ratio is determined by the spectrometer acceptance, which is angle, but not momentum, dependent.)

5. Electromagnetic absorption in the target: Correction was made for the loss of photons by pair production in material upstream of and in the target. The electron pairs contribute to the beam flux measured by the SEQ, but give a negligible

contribution to the cross section. There were $\simeq 0.01$ radiation lengths of material upstream of the target, and the half-length of the short target was $\simeq 0.01$ radiation length.

6. Hadronic absorption in the target: A 1-5% correction was made for hadronic absorption in the target, taking into account the dependence of path length in the target upon scattering angle. A momentum dependent parametrization of the particle cross sections per nucleon was used. No correction was made for double scattering of particles into the spectrometer acceptance. While double scattering must be present at some level, its neglect can be justified by the agreement obtained for long and short target data. An uncertainty of 50% of the correction has been included in the systematic error as a percentage of the subtracted cross section.

C. Acceptance Determination:

In an earlier test of the 20 GeV/c spectrometer,[25] the first and second order matrix elements at the momentum and angle foci were determined using an unscattered electron beam with the spectrometer at 0°. This, however, is insufficient to determine the acceptance of the spectrometer since one must know the matrix elements at each of the possible apertures of the system. Because of the large number of elements in the system, and because several of the magnets differ noticeably

from ideal elements, a correct detailed model of the spectrometer optics does not exist. To determine the acceptance of the spectrometer a "living Monte Carlo" technique was adopted. Using the hodoscopes one can define a smaller acceptance which is not limited by apertures in the spectrometer. The acceptance of this "stringent" region can then be calculated from the final matrix elements alone. By then operating the spectrometer at a momentum with high counting rate and negligible angular and momentum dependence over the spectrometer aperture, one can determine the "normal" acceptance of the spectrometer by comparing the number of particles detected within the normal acceptance to the number detected in the stringent acceptance. Similarly the trigger counter hardware acceptance was determined by comparing the trigger counter rates to those in the smaller aperture counters, which in turn were compared to the stringent software acceptance.

To calculate the acceptance of the stringent region, two independent Monte Carlo programs were used, which included the effects of beam size, target length, scattering angle, and hodoscope bin size. One program used only the matrix elements from the spectrometer optics test, while the second used a model of the spectrometer[25] based on data from the optics test. Both calculations agreed that for angles less than 15°, the aperture counter and stringent software acceptances were independent of target length and beam spot size. Beyond 15°,

the spectrometer model indicated that for the long targets (but not the short targets for which most of the data were taken) these acceptances were being limited by apertures in the spectrometer. (The program using only the final matrix elements, of course, had no knowlege of these apertures and consequently gave no information on the subject.) At 18°, the largest angle for which long target data were taken, this was calculated to be a 1.0% effect for the aperture counters and a 2.4% effect for the stringent hodoscope acceptance. We have applied this correction to the long target data, and have assigned a systematic uncertainty rising linearly from 0. at 12° to 100% of the correction itself at 18°.

The two calculations disagreed by 5% in the absolute value of the stringent acceptance, which is barely consistent with the estimated ±3% uncertainty in the individual calculations. We have used the value obtained from the matrix elements, which is felt to be the more reliable of the two calculations, and have assigned a 3% normalization uncertainty to the stringent acceptance. An additional 1.5% uncertainty in the determination of the aperture counter acceptance is present for the hardware yields.

The normal hardware and software acceptances are functions of scattering angle because the effective width of the target normal to the spectrometer is angle dependent. The ratio of the normal to stringent acceptances was therefore determined from the data as a function of angle. This ratio was found to

be adequately described by a constant at small angles and a linearly falling function at larger angles. The total change in the normal software acceptance from 0° to 21° was 6% for the short targets and 10% for the long targets. For the hardware acceptance, the comparable changes were 10 and 20% respectively. The rms deviation, in excess of statistical counting uncertainties, of the measurements from the assumed form was 0.9%, which has been included in the systematic uncertainty. No dependence was found upon spectrometer momentum or upon whether hydrogen or deuterium targets were used. The spectrometer model was able to reproduce the changes in acceptance in a qualitative but not quantitative manner.

The "living Monte Carlo" technique assumes the absence of nonlinear variation of the cross section across the spectrometer acceptance. The empirical fits to the 18 GeV data were used to correct for the presence of such effects. These corrections ranged from 0 to 3.7% for the angular acceptance and 0 to 1.4% for the momentum acceptance. The fits were also used to calculate the systematic uncertainty in cross section due to the estimated 0.015° uncertainty in spectrometer angle and 0.010 GeV/c uncertainty in spectrometer momentum. These resulted in cross section uncertainties of 0 to 2.7% and 0 to 2.5% for the angular and momentum uncertainties respectively. The effect of an additional 0.003 GeV/c tolerance in setting the spectrometer momentum has been

included in the random errors.

D. Shower Counter Losses

The variable attenuator on the shower counter discriminator input was set to trigger the discriminator at a level which varied linearly with momentum and which conservatively triggered for virtually all electrons and consequently for ≃5% of the hadrons. The shower counter discriminator was flagged and read by the computer, which also read the shower counter pulse height. From the flagged discriminator information an electron cut was placed on the pulse height distribution which matched the hardware definition.

A correction was applied to the data for hadrons which were misidentified as electrons. At large angles electron contamination is negligible (≃0.2%), and one may determine the correction simply by assuming the absence of real electrons and plotting the fraction of counted "electrons" as a function of momentum. A noticeable dependence upon particle type and, to a lesser extent, charge was observed in this correction. The correction varied between 1 and 10%, depending upon momentum and particle type. The data were found to be consistent with the assumed parametrization to 0.3% of the measured yields, which has been included in the systematic uncertainty. For the hardware pion yields an additional 0.5% error has been included in the random uncertainty to account

for differences between the hardware shower counter attenuator and the software pulse height cut.

E. Absorption and Hodoscope Corrections

1. Absorption in the differential Cerenkov counter: Because of the thick windows and high pressure required in the differential Cerenkov counter at low momenta, a sizeable fraction of the hadrons interacted and failed to reach the first range counter located in front of the shower counter. A correction to the software yields was easily obtained by plotting, as a function of momentum and particle type, the fraction of events with good hodoscope codes which failed to trigger the first range counter. The good hodoscope code requirement was necessary for the very low triggering rate points in order to eliminate random coincidences. (This is also the reason the first range counter was required in the hardware pion definition.) Similarly comparison with scaler data in regions of moderate triggering rates showed that the correction thus determined was the same for hardware and software yields. An uncertainty of 1% has been included in the systematic error of the hardware yields to account for differences between the hardware and software electron correction, differential counter absorption correction, and threshold Cerenkov counter efficiency.

The absorption correction for pions varied from 4 to 25% depending upon momentum. The correction was observed to be

≃20% (of itself) larger for protons than for pions. For kaons (and, to a lesser extent, also for protons) the correction cannot be well isolated since kaon identification will be ambiguous for particles interacting in the differential counter. We have assumed the K^+, K^-, p, and $\bar{p}$ corrections to be 76, 90, 130, and 156%, respectively, of the pion correction, independent of momentum, on the basis of total absorption measurements from nuclei.[26] The rms deviation of the pion data from the assumed parametrization was 0.6%, which has been included in the systematic uncertainty as a percentage of the subtracted yields. An additional 10% of the correction has been included in the systematic uncertainty for kaons and protons.

2. Absorption in the hodoscopes and trigger counters: Corrections were made to the data for events which failed to reach the third trigger counter and consequently failed to trigger the computer. These corrections were based on a previous spectrometer study[27] in which varying amounts of absorber were inserted along the detection system, and were checked by relating this absorption correction to that for the differential counter. The correction is momentum dependent and varied from 7 to 14% for pions. As with the differential counter, the correction for kaons and protons was related to that for pions by the total absorption cross section. We have added an estimated 2% error to the normalization uncertainty

and 30% of the momentum dependent term in the correction to the systematic uncertainty.

3. Corrections for bad hodoscope codes: Good events giving multiple tracks in the hodoscopes were due to delta rays, accidental coincidences, and to interactions in the hodoscopes and trigger counters. The rate dependent correction will be discussed below. The rate independent correction was determined as a function of momentum by examining the fraction of bad hodoscope events for runs with moderate counting rate. The hodoscope correction varied between 5 and 8% at 3 and 15 GeV/c respectively, with an estimated uncertainty of 1% which has been included in the normalization error.

4. Miscellaneous hodoscope corrections. Cuts placed on the particle trajectories were used to eliminate spurious events which could not have come directly from the target. With one exception these cuts eliminated a negligible fraction of events not already eliminated by other criteria. This exception was a result of having placed an overly stringent cut such that, at low momenta, multiple scattering in the hodoscopes caused the loss of real events. A correction was therefore made to undo this loss.

F. Decay and Muon Corrections

1. Decay corrections: Pions which decayed in flight either

failed to reach the detectors or were counted as muons by the range telescope. The effective decay path was therefore the distance between the target and the mean penetration distance in the range telescope. Using a decay path of 46.8 m, this resulted in corrections between 6 and 30%. No error has been assigned to this correction.

Some kaons which decayed between the differential Cerenkov counter and the range telescope could still be identified as kaons. Hence a slightly smaller decay path was used (46.0±0.4 m), resulting in corrections between 50.±0.5% to 890.±17.%, where the uncertainties have been included in the systematic error.

2. Muon corrections: Below 5 GeV/c it is possible for muons from pion decay to fail to penetrate the last range counter. In the software yields one could account for this by not requiring the rear-most counters of the range telescope in the muon definition. For the hardware pion yields, only the last range counter was used for muon identification, so a correction was necessary to account for muons which were misidentified as pions. This correction was obtained from the software information and ranged from 0 to 10%, with a systematic uncertainty of 10% of itself.

G. Rate Dependent Corrections:

1. Fast Electronics Dead Time: On the basis of several runs

made at varying intensities, an empirical formula using the singles and coincidence rates in the trigger counters was used to account for dead time in the fast electronics trigger. Because the relative singles and coincidence rates varied widely as a function of spectrometer setting, this formula did not adequately describe the rate dependence for all settings. Hence we have assigned an uncertainty to the correction of 100% of itself. However, counting rates in the spectrometer were kept sufficiently low that this correction was almost always less than 2%, and, for a given point, the counting rates at the high and low energies were nearly identical. We have applied the difference in the rate correction between high and low energies as a percentage of the unsubtracted cross sections, and the average rate correction as a percentage of the subtracted cross section to the random error.

2. Hodoscope rate corrections: The increase in bad hodoscope codes due to rate effects was found to be 2.7 times as large as the electronics dead-time. Again an uncertainty of 100% of the correction has been assigned, and the uncertainties have been handled in the same manner as the electronics dead time.

3. Computer dead time: Because of the short 1.6 μsec length of the SLAC beam pulses, the computer was able to read at most one event per pulse. The computer dead time correction was made by normalizing the total number of computer sampled

events to the total number of triggers in the fast electronics. The correction thus obtained ranged from 0 to 30%.

4. Accidentals corrections: The largest correction for accidental coincidences was for hadron events which were vetoed by a random count in the last range counter, which, owing to a weakness in the shielding at the rear of the spectrometer, had a rather high singles rate. This correction, which was as large as 10%, was made only to the hardware yields, since the software yields used the first blank range telescope counter to define the particle range. Corrections for random coincidences in the shower counter or Cerenkov counters were less than 1% and were not applied.

H. Cerenkov Counter Efficiencies

1. Threshold Cerenkov counter: Pion identification in the hardware yields was determined by the threshold Cerenkov counter discrimination level, while the software yields used the pulse height information. Using data from the differential counter, the threshold counter was determined to be 99.5% efficient in the software yields. Because of dead-times in the gated latches, the hardware efficiency was not determined as accurately; however, the overall discrepancy between hardware and software identification, including differences in the Cerenkov counter efficiency, shower counter

vetoes, and absorption in the differential Cerenkov counter, was less than 1%, which, as has already been mentioned, is included in the systematic errors. The threshold counter had an efficiency of 2.5% for detecting non-pions in the software yields. The same figure (with an assigned 1% systematic uncertainty) was assumed for the hardware yields to correct for non-pion contamination.

2. Differential Cerenkov counter: Events for which the threshold counter failed to trigger were classified as pions, kaons, or ambiguous on the basis of the pulse heights in the inner and outer rings of the differential counter. The pulse heights from the two inner ring counters and the four outer ring counters were summed to form the inner and outer ring pulse heights respectively. The inner vs. outer pulse height plane was then divided into different regions to make the particle identification. Because the divergence of particle trajectories in the spectrometer is greater in the vertical plane than in the horizontal, ambiguities between kaon and pion identification were in some cases resolved on the basis of the two outer ring counters which lay in the horizontal plane (i.e. ignoring the two outer ring counters in the vertical plane).

Efficiencies and contaminations for proton and kaon identification were determined by lowering the pressure of the differential counter such that Cerenkov light from pions fell

in the inner ring. Particle identification in the kaon and proton regions could then be directly compared to the threshold counter identifications of pion and non-pion events. The cuts used and the resulting efficiencies were somewhat momentum dependent. Efficiencies for kaons and protons (including the inefficiency due to misidentification in the threshold counter) were typically 90 and 93% respectively. The assigned systematic uncertainties in the kaon and proton efficiencies were typically 2%, but, at the lowest momenta were as large as 10% for kaons.

3. Particle contaminations: Because the proton signature depends upon a null signal in the Cerenkov counters, and because of the small $\bar{p}/\pi^-$ ratio (typically 1/60), the $\bar{p}$ yields were susceptible to contamination by other particles. However, the requirements placed on the software yields were quite stringent. We feel confident that the quadruple trigger counter coincidence requirement combined with the hodoscope single track requirement and particle trajectory restrictions were adequate to eliminate spurious events not coming directly from the target. Consequently we concern ourselves only with contamination from "real" pions and kaons.

Near the kinematic boundary, relative $\pi^-/\bar{p}$ ratios larger than 1000/1 were measured at the lower of the two beam energies, giving us confidence that any reasonably momentum independent effects, such as pion interactions in the

apparatus, are unimportant. Below 5.8 GeV/c, however, the pion Cerenkov angle in the differential counter was larger than the acceptance of the outer ring. Consequently the 0.5% pion inefficiency in the threshold counter caused a contamination which was as large as 50% of the p yield. We have corrected the $\bar{p}$ yields assuming a threshold counter inefficiency of $0.5 \pm 0.25\%$, where the uncertainty has been included in the systematic errors. (For momenta between 5 and 6 GeV/c it was also necessary to parametrize the efficiency for pions to count as protons in the differential counter.)

For momenta below $\simeq 3.5$ GeV/c, one must also consider the effect of kaons which decay in flight, particularly between the threshold counter and the differential counter. A reasonable fraction of the decays will be eliminated by the threshold counter and the muon telescope and, because of the relatively large opening angles involved in the decay, the trajectory restrictions. The fraction of such events which count as $\bar{p}$'s is difficult to calculate, and we have not made a correction for this effect, but have included a contribution to the systematic errors assuming that 50% of the kaons which decayed between the last bending magnet and the differential counter were counted as $\bar{p}$'s.

In spite of the large systematic uncertainties in the $\bar{p}$ yields, we note that they are severe only at very low momenta where the statistical errors resulting from the bremsstrahlung subtraction are already large. The only other serious

contamination occurred in the K^+ yields at very low momenta where, because of the large fraction of kaons which decay before reaching the detectors, the observed proton to kaon yield was as large as 85/1. We have corrected for the estimated 0.4±0.2% of the proton yield which was counted as kaons.

I. Consistency Checks

1. Short term reproducibility: Because long term drifts in the measuring system tend to cancel in the bremsstrahlung subtraction, they are less important than short term random errors, where a small error in the unsubtracted yield results in a substantial percentage error in the subtracted yield. For almost all data points, more than one run was taken for each setting. One could then determine the rms non-statistical error, which we define as the percentage error which must be added in quadrature with the statistical counting error for each point in order to obtain a chi-squared of 1.0 per degree of freedom for agreement of the individual measurements with the mean for all points at the same setting. The error thus determined was 0.27%. This error is larger than can be accounted for on the basis of rate effects, and, for some points, is comparable to the statistical error. We have therefore included this figure in the random error as a percentage of the unsubtracted cross sections.

2. Long term reproducibility: Several points were repeated at different times throughout the experiment, and a large number of points were also taken with both 16 vs 20 and 17 vs 19 GeV endpoints. Comparison of the 18 GeV average of these runs indicated a non-statistical error 0.7% of the unsubtracted yields, while the errors in the subtracted yields were consistent with counting statistics. The 0.7% figure is consistent with that expected from rate effects and time-dependence of the SEQ calibration, and has not been included in the uncertainty in the subtracted cross sections.

3. Comparison of hardware and software pion yields: For those points in which the pion software data were taken on a sampling basis, small inefficiencies in some of the gated latch signals from the fast electronics caused the software pion yields to be unreliable. However, only the hardware yields were used for the final pion cross sections, and sufficient data were taken in the non-sampling mode to determine all the necessary corrections to the data. The kaon and proton yields were unaffected by the sampling process. Pion yields determined from the software analysis for those runs taken in the non-sampling mode agreed with those determined from the hardware identification to, on average, 0.3%, with an rms deviation of 1.5%, consistent with the systematic uncertainties of the two analyses.

4. Comparison of long and short target yields: The unsubtracted yields determined from the long and short targets were consistent overall to ±0.6%, although at the largest angles systematic differences of ≃2% were discernable. This is consistent with uncertainties in the long target solid angle and double scattering and absorption effects in the target, and has a negligible effect on the subtracted yields, for which the two targets gave results consistent to within counting statistics.

IV. PRESENTATION OF THE DATA

A. The Data

The kinematic points at which the 18 GeV pion data were taken are shown in the Peyrou plot of Fig. 6. Here the vertical axis represents the transverse momentum $p_\perp$ of the detected pion. The horizontal axis shows the c.m. longitudinal momentum $p^*_\parallel$ of the pion and, equivalently, the Feynman scaling variable x, which we define here as $x=2p^*_\parallel/\sqrt{s}$, where s is the total center of mass energy squared. Since the kaon and proton data were taken at the same laboratory momenta and angles as the pion data, the corresponding proton and kaon points are shifted to slightly smaller values of x and $p^*_\parallel$.

The measured values of the invariant cross section

$$E\frac{d^3\sigma}{dp^3} = \frac{E}{p^2}\frac{d\sigma}{d\Omega dp}$$

and the associated random and systematic uncertainties are presented in Tables IV-IX. (The random errors are those listed in Table III added in quadrature with the uncertainty due to counting statistics.) The tables also give the laboratory angle θ, the laboratory momentum p_{lab}, the transverse momentum $p_\perp$, the Feynman scaling variable x, and the "projectile frame" rapidity $y_p = Y - y^*$ of the detected particle. Here y^* is the c.m. rapidity defined by

$$E^* = \mu \cosh y^*$$

$$p^*_\parallel = \mu \sinh y^*$$

where E^* is the c.m. energy of the detected particle and $\mu = \sqrt{p_\perp^2 + m^2}$ is the longitudinal mass of the detected particle with rest mass m. The maximum c.m. rapidity Y is defined (for incident photons) by[28]

$$e^Y = \frac{s - M_p^2}{\mu\sqrt{s}}$$

where M_p is the nucleon mass.

Because of the profusion of kinematic variables commonly used in the analysis of inclusive reactions, and because the data were taken at discrete kinematic points, it was frequently desirable to interpolate the data to fixed values of some variable. To this end, an empirical fit was made to the 18 GeV results. The measured points could then be kinematically shifted small amounts by multiplying the measured cross section by the ratio of the fitted value at the

desired kinematic point to the fitted value at the measured point. These fits were also used in determining the bremsstrahlung corrections and the corrections for the finite momentum and angle acceptance of the spectrometer. In all of the subsequent figures the data have, where necessary, been interpolated to constant values of the appropriate transverse or longitudinal variable.

The fitted function had the form

$$E\frac{d^3\sigma}{dp^3}(x',p_\perp) = 1000\sum_{n=1}^{4}\left(A_n + B_n e^{-(C_n p_\perp)^2}\right)(1-x')^n e^{-D\mu}$$

where A_n, B_n, C_n, and D are free parameters. Here $x' = p^*_\parallel/p^*_{\parallel\,max}(p_\perp)$, where $p^*_{\parallel\,max}(p_\perp)$ is the maximum longitudinal c.m. momentum allowed for the specified value of $p_\perp$, calculated assuming a three body final state with the minimum possible masses. For π^+ production, for example, $p^*_{\parallel\,max}(p_\perp)$ is the maximum π^+ longitudinal momentum allowed for the reaction $\gamma p \rightarrow \pi^+\pi^0 n$. In fitting the pion data, all the parameters were allowed to vary. For the other reactions some parameters were set to zero (i.e. not used), and a common value of the parameter C was used for all powers of (1-x'). The fitted values of the parameters thus obtained are given in Table X. While the resulting chi-squares are rather poor, particularly for the π^+ reactions, the fits provide a qualitative representation of the data and are adequate for purposes of interpolation.

B. Transverse Momentum Dependence

Fig. 7 shows the 18 GeV invariant cross sections for target protons and detected $\pi^{\pm}$, $K^{\pm}$, p, and $\bar{p}$ at a fixed value of x as a function of the transverse momentum $p_{\perp}$. The values of x shown are 0.22, 0.20, and 0.15 for the pion, kaon and proton data respectively. In Fig. 7, as well as all subsequent figures, only the random errors are shown. As with inclusive cross sections for hadron induced reactions, the cross sections at large $p_{\perp}$ values fall exponentially in $p_{\perp}$ with slopes $\simeq 7$ $(GeV/c)^{-1}$. At small values of $p_{\perp}$, the cross sections deviate from an exponential, particularly for heavier mass particles.

As has been observed elsewhere,[29] the differences in the transverse momentum dependence of the different detected particles can be noticeably reduced by using the transverse variable $\mu = \sqrt{p_{\perp}^2 + m^2}$ rather than $p_{\perp}$. Data for a variety of fixed x values are shown plotted against μ in Figs. 8 and 9. For small x and $p_{\perp}$, the $\pi^{\pm}$ data show some deviation from an exponential, while the $K^{\pm}$, p, and $\bar{p}$ data show none. At large values of x, all of the reactions deviate from an exponential for small values of $p_{\perp}$. No significant difference in slope is seen between $\pi^{\pm}$ or between $K^{\pm}$, nor is there any significant x dependence of the slope, except at the largest values of x where the exponential character of the data is questionable.

The data corresponding to a pion x value of 0.22 were fit to an exponential in μ, and the resulting slopes are given in

Table XI. For the pion data, points with $p_\perp$ <0.5 GeV/c were excluded from the fit. The fitted exponentials are shown in Figs. 8 and 9 and, for comparison, are repeated for each value of x. The curves for detected π^+ are also shown as the dashed curves on the corresponding figures for kaons and protons.

C. Longitudinal Momentum Dependence

The 18 GeV invariant cross sections for target protons are shown as a function of x for fixed $p_\perp$ in Figs. 10 and 11. Note the changes in scale for the different $p_\perp$ values. The figures also show the empirical fits used in interpolating the data. As in other non-leading particle hadronic inclusive reactions, the $\pi^\pm$, $K^\pm$ and $\bar{p}$ data at small $p_\perp$ tend to be sharply peaked toward x=0, while at larger $p_\perp$ they show a broader maximum, slightly off-set from x=0. The data for detected protons rise for negative x as expected in the proton fragmentation region. Particularly at large values of $p_\perp$, the π^+ and K^+ yields tend to be noticeably more flat in x than for the corresponding π^- and K^- reactions.

D. Deuterium to Hydrogen Ratios

The ratios (D/H) of the invariant cross sections for target deuterons to those for target protons at 18 GeV are shown in figures 12 and 13 as functions of x and $p_\perp$. Typical D/H ratios for negatively charged detected particles appear to be slightly larger and closer to 2 than the corresponding

ratios for positive particles. At large x the D/H ratio for detected π^- increases with increasing $p_\perp$, while that for π^+ shows a decreasing trend.

One would like to interpret the cross sections from deuterium as the sum of those from the proton and neutron. This naive view is known to be modified by shadowing[30] and smearing[31] corrections. The smearing corrections, which arise from the Fermi motion of the nucleons within the deuterium nucleus, have very little effect on the transverse momentum dependence of the cross section, but, in effect, smear the c.m. energy of the collision. Because of the small energy dependence of the observed cross sections, this effect should be small except perhaps at the largest values of x. Shadowing corrections in γN total cross sections have been calculated to be $\simeq 7\%$ of the nucleon cross section,[32] while for the exclusive photoproduction processes $\gamma p \rightarrow \pi^+ n$ and $\gamma p \rightarrow K^+ \Lambda^0$, where a direct comparison of hydrogen and deuterium data can be made, no shadowing effects at the level of $\lesssim 3\%$ have been observed at comparable energies (except at very small $|t|$, where Pauli exclusion principle effects are important).[33] In this analysis we have neglected shadowing and smearing corrections, and have defined the neutron target cross sections to be the difference between the deuterium and hydrogen target cross sections. In the absence of such corrections, and in view of the near equality of cross sections for neutron and proton targets, one cannot accurately determine, for example, the

difference between π^+ yields from protons and neutrons. On the other hand, because the π^+ and π^- yields are quite similar, one expects nearly equal shadowing corrections. Hence, for example, the uncertainty in the difference between π^+ and π^- cross sections from neutrons should be dominated by counting statistics rather than shadowing effects.

E. Particle to Antiparticle Ratios

The detected π^+ to π^-, K^+ to K^-, and p to $\bar{p}$ cross section ratios at 18 GeV for target proton and neutron are shown in Figs. 14 and 15 as functions of $p_\perp$ and x. For small values of $p_\perp$ or x the π^+/π^- ratio for target protons is greater than but close to unity. At large x, however, this ratio rises with increasing $p_\perp$, reaching a value $\simeq 2$. In contrast, the π^+/π^- ratio for target neutrons is approximately equal to or slightly less than unity everywhere. The K^+/K^- ratios show a similar behavior, except the deviations from unity are larger and at large x the K^+/K^- ratio is greater than unity for target neutrons as well as protons. At large x and $p_\perp$, the K^+/K^- ratio for target protons reaches a value of $\simeq 9$, and the ratio for target neutrons shows a similar rise to a value of $\simeq 3$. The $p/\bar{p}$ ratio rises for either large or negative values of x, and is typically $\simeq 7$ at moderate x values. The rise at large x is presumably due to the difference in the kinematic limit for the two reactions, or to baryon exchange processes leading to a detected proton. The rise at small x is

presumably due to the tail of the proton fragmentation region. The relatively constant value of the $p/\bar{p}$ ratio at intermediate values of x is perhaps indicative of behavior unique to the photon fragmentation region.

V. INTERPRETATION

A. The Mueller-Regge Model in the Photon Fragmentation Region

Mueller[4] has utilized the fact that, in analogy to the optical theorem, the invariant cross section for the inclusive reaction $a + b \rightarrow c + X$ is related to the discontinuity of the forward scattering amplitude for $a + b + \bar{c} \rightarrow a + b + \bar{c}$. For incident particle (projectile) a, target particle b, and detected particle c, this amplitude may be appropriately Reggeized in the projectile fragmentation region (large u, where u is the square of the invariant momentum transfer between b and c) to give the Regge exchange diagram of Fig. 16. The expression for the invariant cross section thus obtained is given by

$$E\frac{d^3\sigma}{dp^3}(y_p,\mu,s) = \sum_i \beta_i(y_p,\mu)\left(\frac{s}{s_0}\right)^{\alpha_i(0)-1}$$

where the sum is over the possible Regge exchanges, β_i is the Regge residue, and $\alpha_i(0)$ is the Regge trajectory intercept. If, asymptotically, the amplitude is dominated by Pomeron exchange, with $\alpha(0)=1$, then for fixed $p_\perp$ and y_p the invariant cross section becomes independent of s, in agreement with the

limiting fragmentation (scaling) hypothesis of Benecke, Chou, Yang, and Yen.[34] At finite energies meson Regge exchanges with intercepts $\alpha(0)=1/2$ give an $s^{-1/2}$ contribution to the invariant cross section.

Even in the absence of direct measurements of the energy dependence of inclusive cross sections, information on the relative contributions of different exchanges may be gained from a comparison of related reactions. From charge symmetry, differences between the photoproduction of particle and antiparticle must be due to exchanges of odd charge conjugation. Similarly, for a given detected particle, differences between target proton and target neutron must be due to exchanges of non-zero isospin. Since the Pomeron carries the vacuum quantum numbers, one then expects that asymptotically the invariant cross section for production of particle and antiparticle for target proton and target neutron should all be equal. Thus the measurement of differences in the invariant cross sections for these reactions provides a measure of the deviation from asymptotic behavior.

By taking the appropriate sums and differences of the invariant cross sections for target proton, target neutron, detected particle, and detected antiparticle, one may isolate the exchanges of different isospin and charge conjugation (or, equivalently, G-parity). In Table XII we list the four possible combinations of isospin, I, (neglecting I>1) and charge conjugation, C. For each set of exchanged quantum

numbers we list the relative sign of its contribution to the cross section for the four combinations of detected particle sign and target. The associated exchange amplitudes have been labelled by the most common Regge exchanges: P, f, A_2, ρ, and ω. (Even if one adopts a more complicated set of Regge exchanges, these serve as useful mnemonics to identify the exchanged quantum numbers.) To illustrate the relative sizes of the different exchanges, the P+f, ρ, and ω contributions to the amplitude for detected pions at $p_\perp$=1 GeV/c are shown in Fig. 17 as a function of y_p. In the absence of deuterium shadowing corrections the A_2 exchange contribution cannot be determined.

The ρ and ω contributions for detected pion and kaon at 18 GeV are shown in Fig. 18 as a function of y_p for different values of $p_\perp$. We note here the interpretation, within the Mueller-Regge picture, of the large π^+/π^- ratio at large x and $p_\perp$ for target protons compared to the near unity value for target neutrons (see Fig. 14). At large x, the ρ and ω contributions have the same sign and are approximately equal in magnitude. The deviation from unity of the π^+/π^- ratio is determined by the ρ and ω exchanges, which add constructively for target protons but approximately cancel for target neutrons.

Because the quantum numbers of the $ab\bar{c}$ system are exotic for detected K^- or $\bar{p}$, some theories predict early scaling in these reactions.[35,36] In the Mueller-Regge picture this is accomplished by the cancellation through exchange degeneracy

of the meson Regge exchanges, leaving only the background (Pomeron) exchange contribution. This would then predict the equality of target proton and target neutron invariant cross sections for these reactions. In Figs. 12 and 13 the D/H ratios for K^- and $\bar{p}$ are seen to be consistent with 2, but with poor statistical accuracy. Because the equality of target proton and target neutron cross sections should be valid over the entire photon fragmentation region, however, one can gain better statistical accuracy by using the unsubtracted rather than subtracted bremsstrahlung yields. This, of course, results in a measurement which spans a range in incident energy and x. Fig. 19 shows the D/H ratios for detected $K^{\pm}$, p, and $\bar{p}$ for $x_{min} = 0.2$ as a function of $p_{\perp}$. The D/H ratios for K^- and $\bar{p}$ appear independent of $p_{\perp}$. If the points are averaged over $p_{\perp}$, one obtains average D/H ratios of 1.90±0.03 and 1.94±0.05 for the K^- and $\bar{p}$ reactions respectively, which should be compared to ratios of 1.74±0.03 and 1.82±0.03 for the K^+ and p reactions. If, on the basis of total cross section and exclusive reaction measurements,[32,33] one assumes deuterium corrections of less than 10% of the nucleon cross sections, then the results are consistent with the equality of target proton and target neutron cross sections for detected K^- and $\bar{p}$, but not for detected K^+ and p. We note, however, that the non-exotic reaction $\gamma p \rightarrow \pi^- X$ shows a D/H ratio similarly closer to 2 than the corresponding ratio for detected $\pi^{\pm}$.

B. Energy Dependence

Figs. 20-22 show the invariant cross sections for target protons obtained in this experiment, compared to other experiments at lower energies.[5,12,13] For the detected pion and kaon reactions the contributions from the two-body reactions $\gamma p \rightarrow \rho p$ and $\gamma p \rightarrow \phi p$ respectively are shown as the solid (18 GeV) and dashed (6 GeV) curves. These were obtained from a calculation of the decay spectrum using the measured ρ and ϕ differential cross section data of Anderson et al.[37] The small differences in the decay spectra at the two energies are due primarily to the energy dependence of the differential cross sections. For the ϕ cross sections in particular this energy dependence is comparable to the uncertainties of the measurements.

Duality arguments require that in a simple Regge model, invariant cross sections should approach their asymptotic values from above.[36] For detected $\pi^{\pm}$ and K^{+} this appears consistent with the data at small values of $p_{\perp}$. At large values of $p_{\perp}$, however, the cross sections for detected $\pi^{\pm}$, K^{-}, and to a lesser extent, K^{+} are seen to be rising with energy. Furthermore, if one attempts to describe the data with only contributions of s^{0} and $s^{-1/2}$, then at large $p_{\perp}$, the Pomeron contribution would have to be almost entirely absent in order to accomodate the observed energy dependence between 6 and 18 GeV. Thus it appears likely that at large $p_{\perp}$, the simple Regge picture must be modified by, for example, kinematic

effects[36,38] with a larger energy dependence than the simple $s^{-1/2}$ given by meson Regge exchange.

The prediction of early scaling[35,36] for the detected K^- reaction appears moderately satisfied at low $p_\perp$, but clearly fails at larger $p_\perp$. No measurements exist from other experiments for detected $\bar{p}$. The limited measurements at lower energy from this experiment indicate that at large $p_\perp$, the $\bar{p}$ cross sections are rising rapidly as a function of energy.

When plotted against y_p for fixed $p_\perp$, the cross sections for detected protons show a rapid fall with increasing energy. Because the data at 6 GeV have a somewhat limited range of rapidity, and in view of the fact that the most obvious source of protons is from fragmentation of the target, we have plotted the detected proton cross sections in Fig. 23 against laboratory rapidity rather than projectile rapidity. The maximum allowed rapidities (y_p = 0.) at 6 and 18 GeV are indicated by the arrows in Fig. 22. In the limited region near y_{lab} =2, where overlap exists between the 6 and 18 GeV experiments, the cross sections are quite comparable. This is consistent with the generally accepted range of the target fragmentation region of $y_{lab} \simeq 2$.

While deviations from the predicted Mueller-Regge behavior are clearly present for large values of $p_\perp$, it has been argued that these effects enter only the vacuum quantum number exchanges.[38] By isolating the exchange contributions with

non-vacuum quantum numbers one may therefore still hope to observe the simple $s^{-1/2}$ energy dependence given by conventional meson Regge exchange. In Fig. 23 we have plotted the difference between detected particle and antiparticle invariant cross sections for detected pions and kaons with proton target, multiplied by $s^{1/2}$, for this experiment and the DESY experiment at 6 GeV.[12] The qualitative agreement in shape between the two experiments is quite good, particularly considering the very low missing mass values of some of the data of the 6 GeV experiment.

The large rise in the cross section difference between π^+ and π^- at large x (small y_p) and $p_\perp$ is similar to the large π^+/π^- ratio observed in exclusive pion photoproduction at large t, and suggests the applicability of a triple-Regge model. Unfortunately our data are not sufficiently finely spaced at large x to permit such an analysis. In particular, the data do not establish a range over which the logarithm of the cross section is linear in the logarithm of the missing mass squared, as required by the model.

C. The Mueller-Regge Model in the Central Region

In the central region (t and u large) the Mueller-Regge model with factorization predicts cross sections of the form[4]

$$E\frac{d^3\sigma}{dp^3}(y^*,\mu,s) = \sum_{i,j} \gamma_i^b \beta_{ij}^{\bar{c}}(\mu)\gamma_j^a e^{[\alpha_i(0)-\alpha_j(0)]y^*}\left(\frac{s}{s_0}\right)^{[\alpha_i(0)+\alpha_j(0)-2]/2}$$

corresponding to the Regge exchange diagram of fig 24. Here the γ's give the coupling between the exchanged Reggeon and the target or projectile; these may be determined from total cross section data. The β's give the coupling between the two Reggeons and the detected particle c. For given exchanges i and j and detected particle c, the coupling β_{ij} is a function only of $p_\perp$. Thus, assuming conventional Regge exchanges with trajectory intercepts $\alpha(0)=1$ (Pomeron) or 1/2 (meson), one expects contributions to the cross section of s^0 (Pomeron-Pomeron), $s^{-1/4}$ (Pomeron-meson), and $s^{-1/2}$ (meson-meson) for fixed $p_\perp$ and y*.

Ferbel[39] has shown that for a variety of inclusive reactions at y*=0, the invariant cross sections integrated over $p_\perp$ are consistent with an $s^0 + s^{-1/4}$ dependence, where the data extend to remarkably low incident energies. However, several features have arisen in the central region which are somewhat disturbing from the point of view of the most naive Mueller-Regge models. There is some evidence that $p\,p \rightarrow \pi^{\pm}X$ data, at fixed values of $p_\perp$, fail to extrapolate to a common value at $s^{-1/4} = 0$ when assumed to be linear in $s^{-1/4}$.[40] Relations between different reactions demanded by factorization appear to be badly violated.[41] Inclusive cross sections in the central region usually approach their asymptotic values from below, in contradiction to the simplest duality arguments.[36,38] Reactions such as $p\,p \rightarrow K^- X$ or $p\,p \rightarrow \bar{p}\,X$, for which one expects early scaling, show larger

energy dependences than reactions such as $p\,p \rightarrow \pi^{\pm}X$. The latter two points are again frequently attributed to kinematic effects, and it has been argued that these effects cancel if one treats the differences between particle and antiparticle cross sections.[38] Inami[42] has further emphasized the importance of investigating the energy dependence for fixed values of $p_{\perp}$. For the reaction $p\,p \rightarrow \pi^{\pm}X$ he has shown that the detected $\pi^{\pm}$ cross section difference is consistent with an $s^{-1/4}$ behavior at large $p_{\perp}$, but not at small $p_{\perp}$.

If only $s^{-1/4}$ terms are included, our data for the difference between particle and antiparticle yields may be compared to the corresponding pp data through factorization. Noting that only exchanges of even charge conjugation couple to the photon vertex of Fig. 24, and keeping only meson-Pomeron terms, we may write

$$\Delta^{c}_{pp}(y^*,\mu,s) \equiv E\frac{d^3\sigma}{dp^3}(pp \rightarrow cX) - E\frac{d^3\sigma}{dp^3}(pp \rightarrow \bar{c}X)$$

$$= 4\sum_i \gamma^p_P \gamma^p_i \beta^{\bar{c}}_{iP}(\mu)\cosh(y^*/2)\left(\frac{s}{s_0}\right)^{-1/4}$$

$$= 4\,\sigma_{pp}\sum_i \frac{\gamma^p_i}{\gamma^p_P}\,\beta^{\bar{c}}_{iP}(\mu)\cosh(y^*/2)\left(\frac{s}{s_0}\right)^{-1/4}$$

and

$$\Delta^{c}_{\gamma p}(y^*,\mu,s) \equiv E\frac{d^3\sigma}{dp^3}(\gamma p \rightarrow cX) - E\frac{d^3\sigma}{dp^3}(\gamma p \rightarrow \bar{c}X) = 2\sum_i \gamma^{\gamma}_P \gamma^p_i \beta^{\bar{c}}_{iP}(\mu)e^{-y^*/2}\left(\frac{s}{s_0}\right)^{-1/4}$$

$$= 2\,\sigma_{\gamma p}\sum_i \frac{\gamma^p_i}{\gamma^p_P}\,\beta^{\bar{c}}_{iP}(\mu)e^{-y^*/2}\left(\frac{s}{s_0}\right)^{-1/4}$$

where the sum is over allowed odd charge conjugation exchanges ($i=\rho,\omega$ for $c=K$; $i=\rho$ for $c=\pi$), and $\sigma_{pp} = (\gamma_P^p)^2$ and $\sigma_{\gamma p} = \gamma_P^p \gamma_P^\gamma$ are the asymptotic total cross sections. Hence

$$\Delta^c_{\gamma p}(y^*,\mu,s) = \frac{1}{2}\frac{\sigma_{\gamma p}}{\sigma_{pp}}\Delta^c_{pp}(0,\mu,s_1)e^{-y^*/2}\left(\frac{s}{s_1}\right)^{-1/4}$$

Thus to leading order in s the photoproduction cross section differences are related to the equivalent pp cross section differences solely through the ratio of the asymptotic total cross sections. Using values of 40 and 0.1 mb for the pp and γp total cross sections respectively, the predicted results for the γp reactions are shown in Fig. 23. The dashed curves are obtained from the 12 and 24 GeV data of the Bonn-Hamburg-Munchen collaboration,[43] while the solid curves are obtained from the ISR data of the British-Scandinavian (BS) collaboration.[40] For detected pions, the prediction is seen to fail at both large and small values of $p_\perp$.

Noting that at 18 GeV there is only a factor of 2.5 difference between $s^{-1/4}$ and $s^{-1/2}$, it is difficult to justify the neglect of $s^{-1/2}$ terms. In fact, from our data alone we can see from Fig. 18 that, if one accepts the simplest Mueller-Regge model, then $s^{-1/2}$ terms must be present in the pion production reaction. The ρ and ω exchange amplitudes extracted in the previous section for the single Regge model give, in the double Regge model, the ρ and ω exchanges between the pion and proton vertices of Fig. 24. In order to conserve

G-parity at the pion vertex, the ω exchange must be accompanied by A_2 exchange between the pion and gamma legs of Fig. 24, which would contribute an $s^{-1/2}$ dependence. From Fig. 18 the ω exchange contribution appears to be non-zero near $y^*=0$. We note further that the signs of the ω contribution are consistent with the discrepancies between the high energy pp prediction and the observed data. An additional $s^{-1/2}$ contribution, on which we have no information, can come from ρ-f exchange.

The problem of $s^{-1/2}$ terms may be circumvented by comparing $\Delta^K_{\gamma p}$ and Δ^K_{pp}, and imposing exchange degeneracy requirements. We note that for $\gamma p \rightarrow K^- X$ (or $p\,p \rightarrow K^- X$) the fact that K^+p is exotic in the s channel should result in the cancellation of non-Pomeron exchanges between the kaon and proton. For $\gamma p \rightarrow K^+ X$ (or $p\,p \rightarrow K^+ X$), while neither K^-p nor $K^-\gamma$ is exotic, meson-meson terms should nonetheless be suppressed,[44] as can be seen from the quark diagram of Fig. 25. To the extent that the photon may be treated as a non-strange quark - anti-quark pair, the presence of the strange quark in the K^- requires Pomeron exchange in one leg or the other of Fig. 24. Thus for the detected kaon cross sections, the neglect of $s^{-1/2}$ terms is more plausible. Meson-meson terms can arise from the strange quark - anti-quark component of the photon, but this (ϕ) component is considerably more weak than the non-strange (ρ,ω) components

of the photon. The prediction obtained from the BS data[40] shown in Fig. 23 for kaon production is in noticeably better agreement with the data than the corresponding prediction for pions.

D. The Constituent Interchange Model

One of the unexpected features which emerged from inclusive reactions at high energies was the observation of cross sections at large $p_\perp$ which are larger than would be expected from extrapolation of the exponential behavior of lower $p_\perp$ data.[45] This has given rise to much theoretical activity in parton models, which predict invariant cross sections of the form[3]

$$E\frac{d^3\sigma}{dp^3} = \frac{1}{(p_\perp^2)^N} f(\epsilon,\theta^*)$$

$$\epsilon \equiv 1 - \frac{E^*}{E^*_{max}}$$

where N is an integer power, E^* is the c.m. energy of the detected particle, E^*_{max} is its maximum kinematically allowed value, and f is an arbitrary function of ϵ and the c.m. angle θ^* of the detected particle.

In the constituent interchange model (CIM) of Blankenbecler, Brodsky, and Gunion,[46] the ϵ dependence of the cross section is further specified. In the CIM, large $p_\perp$ inclusive processes $A + B \rightarrow C + X$ are assumed to arise from basic hard scattering sub-processes $a + b \rightarrow c + d$ in which the particles a, b, c, and d may be hadrons, quarks, or

di-quarks, and C is is either identical to or a fragment of c. The basic sub-process is masked by the "hadronic bremsstrahlung" of particles A, B, and c, the products of which do not participate in the basic sub-process.

Through dimensional counting rules, the invariant cross section is then given by a sum of terms of the form

$$E\frac{d^3\sigma}{dp^3} = \sum_i \frac{\epsilon^{P_i}}{\left(p_\perp^2 + M_i^2\right)^{N_i}} f_i(\theta^*) \tag{1}$$

where P_i and N_i are integer powers, M_i is a fixed parameter to account for finite mass effects, and f_i is (in practice) an arbitrary function of the c.m. angle θ^*. The subscript i refers to the specific sub-process and bremsstrahlung products. For a given sub-process, the powers N and P are given by

$$N = n_{active} - 2$$

$$P = 2n_{passive}^{hadronic} + n_{passive}^{e.m.} - 1$$

where n_{active} is the number of elementary fields participating in the basic sub-process, and $n_{passive}$ is the number of "passive" fields which do not take part in the basic sub-process. The superscripts "hadronic" and "e.m." refer to the number of passive quarks coupling to hadrons or photons respectively.

In the absence of knowlege of which are the important

sub-processes, the number of possible values of N and P is large, as is shown in Fig. 26 for the photoproduction reactions considered here.[47] For comparable strengths $f_i(\theta^*)$, terms with minimal values of N and/or P will dominate.

As is traditional in the absence of high precision data over a broad kinematic range, we shall make the optimistic assumption that a single term of the form of eq. 1 dominates the cross section. In order to conveniently use the data of this experiment and that of ref. 12, we utilize the fact that the measured cross sections for small x are relatively slowly varying in θ^* and consequently use data for fixed $x \simeq 0.2$ rather than for fixed c.m. angle. We have therefore fit all $x \simeq 0.2$ data (including 9 and 13 GeV points near x=0.2) with $p_\perp > 0.5$ GeV/c to the form of eq. 1. The values of the parameters obtained are given in Table XIII, and the preferred values of P and N are shown as the solid squares in Fig. 26. The π^- data and the corresponding fit are shown in Fig. 27. The resulting chi-squares are rather poor, but, considering the liberties taken in matching the data and the theory, may be considered acceptable. With the exception of the K^+ reaction, the preferred values of N and P lie near the boundary of minimal N+P values. The large value of N obtained for the K^+ reaction is probably an artifact of the strong correlation between the parameters M and N, and the anomolously large value obtained for M.

For all reactions the data prefer smaller values of P in

preference to smaller values of N. The values N=6, P=1, favored for the pion reactions, correspond to sub-processes of the form quark + baryon → meson + di-quark or meson + di-quark → meson + di-quark. (In either case the photon acts as a vector meson rather than an elementary field. The values N=5, P=1, would correspond to the sub-process photon + di-quark → meson + di-quark, with the photon as an elementary field.)

Because of the strong correlations in the fitted parameters, the statistical weighting of the data toward small $p_\perp$, and the larger number of points at the highest energy, it is of some interest to attempt to determine the parameters P and N separately. In Fig. 28 we show the $p_\perp$=1. GeV/c data as a function of E^*/E^*_{max}. These data were fit separately to integer powers of P, and the 18 GeV data alone, with fixed values of P, were then fit to integer powers of N. The range for P and N over which acceptable fits could be obtained are shown as the shaded areas in Fig. 26. While the K^- and $\bar{p}$ data appear to prefer slightly larger values of P than do the $\pi^\pm$ and K^+ data, the quality of the data are not sufficient to establish the larger values of P and/or N predicted by the model for these two reactions. In fact, the data for all reactions are consistent with the values N=5-7, P=1. We note that had we defined ϵ as $1-2p^*/\sqrt{s}$ rather than $1-E^*/E^*_{max}$, higher values of P would have been obtained for the $\bar{p}$ and, to a lesser extent, kaon reactions.

Eisner et al.[16] have analysed π^0 photoproduction data at

larger values of x and obtained values of P ($\simeq$.5) and N ($\simeq$6-7) quite similar to those obtained here. In contrast, Carey et al.[48] have analysed pp data using a value of N=4.5 and obtained values for P of 4, 4, 5, and 7 for π^0, π^-, K^-, and $\bar{p}$ production respectively.

VI. SUMMARY

Inclusive photoproduction of charged particles in the photon fragmentation region show qualitative features similar to those of hadron induced inclusive reactions: Invariant cross sections fall exponentially with $\mu = \sqrt{p^2+m^2}$ for sufficiently large μ and small x, with slopes ~ 6.5 - 9.5 $(GeV/c)^{-1}$. Dependence upon longitudinal momentum is noticeably weaker than upon transverse momentum, and x distributions are broader at large $p_\perp$ than at small $p_\perp$.

Within the context of the Mueller-Regge model we find:

1. Except in the reaction $\gamma p \rightarrow p\ X$, invariant cross sections for small $p_\perp$ are consistent with Mueller-Regge predictions of a dominant energy-independent Pomeron term, although differences between particle and antiparticle yields and a finite s-dependence indicate the presence of non-leading Regge terms. At large $p_\perp$ a more pronounced energy dependence requires modification of the most simple Regge model by, for example, introduction of kinematic terms. At small $p_\perp$ invariant cross sections are decreasing with energy, as

expected from duality arguments, while at large $p_\perp$ cross sections are increasing with energy.

2. The invariant cross sections for detected K^-, which are expected to show early scaling, are consistent with the absence of energy dependence at small $p_\perp$, but are increasing with energy at large $p_\perp$.

3. The reaction $\gamma p \rightarrow p X$ for fixed y_p and $p_\perp$ shows a strong falling s dependence when compared to data at 6 GeV, indicating that a Regge expansion of this reaction in the photon fragmentation region is not valid for $y_{lab} \lesssim 2$.

4. For the detected K^- and $\bar{p}$ reactions, the expected equality of target proton and target neutron cross sections appears to be satisfied to within the uncertainties of deuterium corrections.

5. For large x and large $p_\perp$, the large π^+/π^- and K^+/K^- ratios for target proton, combined with the smaller ratios for target neutron require both ρ and ω exchange.

6. The difference between detected π^+ and π^- cross sections and between detected K^+ and K^- cross sections, when compared to data at 6 GeV data, are in reasonable agreement with the predicted $s^{-1/2}$ dependence for fixed y_p and $p_\perp$.

7. Predictions to leading order in s of the $\pi^{\pm}$ cross section difference in the central region obtained from high energy pp data are in poor agreement with the data. The combination of proton and deuteron target data indicate the presence of $s^{-1/2}$ terms of the correct sign to account for the discrepancy. A similar prediction for the $K^{\pm}$ cross section difference, where $s^{-1/2}$ terms should be suppressed, is in better agreement with the data.

The data for $x \simeq 0.2$, $p_{\perp} \gtrsim 0.5$ GeV/c were fit to the form

$$E\frac{d^3\sigma}{dp^3} = \frac{\epsilon^P}{(p_{\perp}^2 + M^2)^N} f$$

given by the constituent interchange model. The data prefer small values of P in preference to small values of N. The powers of N and P obtained are consistent with those obtained from π^0 photoproduction data at a comparable energy, and differ noticeably from those obtained from pp reactions (mostly at higher energies).

VII. ACKNOWLEGEMENTS

We are indebted to A. Golde, R. Eisele, S. Dyer, A. Filippi, and L. Boyer of the spectrometer facilities group at SLAC for the set-up of the experiment, to G. Sherden for dogged pursuit of many of the problems encountered during the

run, to J. Mark and the hydrogen target group for the design, construction, and maintainance of the target system, and to the entire SLAC operations crew. Particular thanks are due to R. Miller for development of the rapid energy change capability, and to R. Johnson, J. Piccioni, and P. Brickey for programming work on the 9300/925 computer link. We gratefully acknowlege a number of helpful discussions with G. Goldstein, R. Blankenbecler, and D. Sivers concerning the interpretation of the data.

REFERENCES

1. For general reviews of inclusive phenomenology see, for example, W.R. Frazer, L. Ingber, C.H. Mehta, C.H. Poon, D. Silverman, K. Stowe, P.D. Ting, and H.J. Yesian, Rev. Mod. Phys. 44, 284 (1972); D. Horn and F. Zachariason, Hadron Physics at Very High Energies, (Benjamin, Reading, Mass., 1973).

2. For reviews of recent high energy experiments see, for example, E.L. Berger, CERN Preprint TH. 1737 (1973, unpublished) ; R. Slansky, Phys. Reports 11C,99 (1974).

3. For a review of parton models of large transverse momenta phenomena see, for example, D. Sivers, S. Brodsky, and R. Blankenbecler, SLAC-PUB-1595 (1975, submitted to Physics Reports).

4. A.H. Mueller, Phys. Rev. D2, 2963 (1970).

5. K.C. Moffeit, J. Ballam, G.B. Chadwick, M. Della-Negra, R. Gearhart, J.J. Murray, P. Seyboth, C.K. Sinclair, I.O. Skillicorn, H. Spitzer, G. Wolf, H.H. Bingham, W.B. Fretter, W.J. Podolsky, M.S. Rabin, A.H. Rosenfeld, R. Windmolders, G.P. Yost, and R.H. Milburn, Phys Rev. D5, 1603 (1972).

6. Chan Hong-Mo, H.I. Miettinen, and W.S. Lam, Phys. Lett. 40B,112 (1972).

7. J.R. Fry, R. Matthews, H. Muirhead, C. Brankin, A. Angelopoulos, A. Apostolakis, P. Theocharopoulos, G. Vasiliades, T.A. Filippas, E. Simopoulou, P. Tsilimigras, A. Vayaki, B. Buschbeck, D. Dallman, G. Otter, P. Schmid, and H.I. Miettinen, Nucl. Phys. B58,420 (1973).

8. R.L. Anderson, B. Gottschalk, D.B. Gustavson, D.M. Ritson, G.A. Weitsch, H.J. Halpern, R. Prepost, and D.H. Tompkins, Phys. Rev. Lett. 30, 627 (1973).

9. Preliminary results of this experiment for pions and kaons were reported as a contribution to the 1971 International Symposium on Electron and Photon Interactions at High Energies, (Cornell Univ. Press, Ithaca, N.Y., 1972).

10. W.P. Swanson, M. Davier, I. Derado, D.C. Fries, F.F. Liu, R.F. Mozley, A.C. Odian, J. Park, F. Villa, and D.E. Yount, Phys. Rev. Lett. 27, 1472 (1971).

11. W. Struczinski, P. Dittmann, V. Eckardt, P. Joos, A. Ladage, H. Meyer, B. Naroska, D. Notz, S. Yellin, G. Hentschel, J. Knobloch, E. Rabe, S. Brandt, M. Grimm, D. Pollmann, I. Derado, R. Meinke, P. Schacht, and H. Strobl, contribution to the XVI International Conference on High Energy Physics, 1972 (NAL, Batavia, Ill., 1973).

12. H. Burfeindt, G. Buschhorn, H. Genzel, P. Heide, U. Kotz, K.H. Mess, P. Schmuser, B. Sonne, G. Vogel, and B.H. Wiik, Phys. Lett. 43B, 345 (1973), and Nucl. Phys. B74, 189 (1974).

13. W. Kaune, G. Miller, W. Oliver, R.W. Williams, and K.K. Young, Phys. Rev. D11, 478 (1975).

14. J. Gandsman, G. Alexander, S. Dagan, L.D. Jacobs, A. Levy, D. Lissauer, and L.M. Rosenstein, Nucl. Phys. B61, 32 (1973); G. Alexander, O. Benary, S. Dagan, J. Gandsman, J. Grunhaus, P. Katz, A. Levy, and D.A. Lissauer, Phys. Rev. D8, 712 (1973).

15. Ch. Berger, G. Dick, W. Erlewein, K. Lubelsmeyer, L. Paul, H. Meyer-Wachsmuth, and A. Schultz von Dratzig, Phys. Lett. 47B, 377 (1973).

16. A.M. Eisner, D.O. Caldwell, J.P. Cumalat, B.N. Kendall, T.P. McPharlin, R.J. Morrison, and F.V. Murphy, Phys. Rev. Lett. 33, 865 (1974).

17. The Stanford Two-Mile Accelerator, R.B. Neal, ed., (Benjamin, New York, 1968).

18. A.M. Boyarski, SLAC-PUB-559 (1969) or Proceedings of the Conference on Computer Systems in Experimental Physics, Skytop, Penn., (1969) pp.139-72.

19. R.S. Larsen and D. Horelick, SLAC-PUB-398 (1968) or Proceedings of the Symposium on Beam Intensity Measurement, Daresbury, (1968) pp. 260-79.

20. G.E. Fischer and Y. Murata, Nucl. Inst. and Meth. 78, 25 (1970).

21. SLAC Users' Manual and L. Mo, SLAC-TN-65-40 (1965, unpublished).

22. See, for example, R.F. Schwitters, J. Leong, D. Luckey, L.S. Osborne, A.M. Boyarski, S.D. Ecklund, R. Siemann, and B. Richter, Phys. Rev. Lett. 27,120 (1971); A.M. Boyarski, F. Bulos, W. Busza, R. Diebold, S.D. Ecklund, G.E. Fischer, J.R. Rees, and B. Richter, Phys. Rev. Lett. 20,300 (1968); D. H. Tompkins, SLAC Report 109 (thesis, 1970,unpublished).

23. R.A. Early, SLAC-TN-66-15 (1966, unpublished).

24. R. P. Feynman, Phys. Rev. Lett. 23, 1415 (1969).

25. E. Taylor, SLAC, private communication.

26. S.P. Denisov, S.V. Donskov, Yu. P. Gorin, R.N. Krasnokutsky, A.I. Petrukhin, Yu. D. Prokoshkin, and D.A. Stoyanova, Nucl. Phys. B61, 62 (1973).

27. R. Diebold, SLAC Group C private communication.

28. The more conventional definition of Y is given by $e^{2Y} = s/m_a^2$, where m_a is the mass of the incident beam particle. With incident photons the factor $(s-M_p^2)/\sqrt{s}$ in our definition results in the four momentum transfer, t, between incident and detected particle being independent of s for fixed y_p and μ. The use of μ rather than the

clearly inappropriate m_a results in $\mathcal{M}^2/s$ asymptotically approaching 0 at $y_p=0$, where $\mathcal{M}^2$ is the missing mass squared.

29. E. Leader and M.R. Pennington, Phys. Rev. Lett. 27,1325 (1971); R.C. Arnold and E.L. Berger, Phys. Rev. D5, 2733 (1972); M. Deutschmann, H. Grassler, H. Kirk, P. Sixel, R. Speth, W. Sturm, H. Novak, U. Kundt, G.J. Bossen, E. Propach, M. Rost, B.U. Stocker, T. Besliu, P. Duinker, D.R.O. Morrison, R. Stroynowski, H. Wahl, J. Zaorska, T. Hirose, J. Stiewe, A.A. Azooz, P. Schmid, B. Buschbeck, H.P. Gerhold, and H. Blalkowska, Nucl. Phys. B70, 189 (1974).

30. R.J. Glauber, Phys. Rev. 100, 242 (1955); V. Franco and R.J. Glauber, Phys. Rev. 142, 1195 (1966).

31. G.B. West, Ann. Phys. 74,464 (1972); W.B. Atwood and G.B. West, Phys. Rev. D7, 773 (1973).

32. D.O. Caldwell, V.B. Elings, W.P. Hesse, R.J. Morrison, and F.V. Murphy, Phys. Rev. D7, 1362 (1973).

33. A.M. Boyarski, R. Diebold, S.D. Ecklund, G.E. Fischer, Y. Murata, B. Richter, and M. Sands, Phys. Rev. Lett. 25,695 (1970).

34. J. Benecke, T.T. Chou, C.N. Yang, and E. Yen, Phys. Rev. 188,2159 (1969).

35. Chan Hong-Mo, C.S. Hsue, C. Quigg, and J.M. Wang, Phys. Rev. Lett. 26,672 (1971).

36. For a simplified discussion of duality in inclusive reactions and its implications for exoticity conditions and direction of approach to scaling, see, for example, R.G. Roberts, Rutherford report RL-73-095 (1973, unpublished). For more rigorous, and sometimes conflicting, treatments see M.B. Einhorn, M.B. Green, and M.A. Virasoro, Phys. Rev. D6,1675(1972); S-H.H. Tye and G. Veneziano, Nuovo Cim. 14A,711(1973).

37. R. Anderson, D. Gustavson, J. Johnson, D. Ritson, B.H. Wiik, W.G.Jones, D. Kreinick, F. Murphy, and R. Weinstein, Phys. Rev. D1,27 (1970).

38. Chan Hong-Mo, H.I. Miettinen, D.P. Roy, and P. Hoyer, Phys. Lett. 40B,406 (1972).

39. T. Ferbel, Phys. Rev. Lett. 29,441 (1972); Phys. Rev. D8, 2321 (1973).

40. B. Alper, H. Boggild, P. Booth, F. Bulos, L.J. Carroll, G. Von Dardel, G. Damgaard, B. Duff, F. Heymann, J.N. Jackson, G. Jarlskog, L. Jonsson, A. Klovning, L. Leistam, E. Lillethun, G. Lynch, S. Olgaard-Nielsen, M. Prentice, D. Quarrie, and J.M. Weiss, Phys. Lett. 47B,75 (1973); Phys. Lett. 47B,275 (1973); Nucl. Phys. B87, 19 (1975).

41. S. Rai Choudhury, Lett. Nuovo Cim. 5,7 (1972); R.F. Amann and M.L. Blackmon, Phys. Lett. 44B,266 (1973).

42. T. Inami, Nucl. Phys. B77, 337 (1974).

43. V. Blobel, G.W. Brandenburg, H. Fesefeldt, H. Franz, B. Hellwig, U. Idschok, D. Monkemeyer, H.J. Muck, H.F. Neumann, M. Schachter, N. Schmitz, W. Schrankel, B. Schwarz, B.M. Schwarzschild, F. Selonke, P. Soding, and B. Wessels, Nucl. Phys. B69,454 (1974).

44. We are indebted to G. Goldstein for pointing this out to us.

45. See, for example, F.W. Busser, L. Camilleri, L. Di Lella, G. Gladding, A. Placci, B.G. Pope, A.M. Smith, J.K. Yoh, E. Zavattini, B.J. Blumenfeld, L.M. Lederman, R.L. Cool, L. Litt, and S.L. Segler, Phys. Lett. 46B, 471 (1973).

46. J.F. Gunion, S.J. Brodsky, and R. Blankenbecler, Phys. Rev. D6,2652 (1972); R. Blankenbecler and S.J. Brodsky, Phys. Rev. D10, 2973 (1974).

47. See ref. 3 for details of the determination of the allowed values of N and P. The allowed values shown treat the photon both as an elementary field (N+P even) and as a vector meson (N even, P odd). Values with N odd and P even are not allowed. Because of the apparantly stronger effect of the target fragmentation region on the 6 GeV data compared to the 18 GeV data, we have not attempted to fit the data for detected protons.

48. D.C. Carey, J.R. Johnson, R. Kammerud, M. Peters, D.J. Ritchie, A. Roberts, J.R. Saver, R. Shafer, D. Theriot, J.K. Walker, and F.E. Taylor, Phys. Rev. Lett. 33,327(1974); Phys. Rev. Lett. 33,330 (1974).

TABLE I. Inclusive photoproduction experiments.

Group	Beam	Detector	Reactions	Energy (GeV)	x	$p_\perp$ (GeV/c)
SLAC (this experiment)[9]	Subtracted bremsstrahlung	Spectrometer	$\left.\begin{matrix}\gamma p\\ \gamma D\end{matrix}\right\} \rightarrow \left\{\begin{matrix}\pi^\pm X\\ K^\pm X\\ p\ X\end{matrix}\right.$	9,13,18	0. to 0.8	0.2 to 2.0
SLAC-Berkeley-Tufts[5]	Backscattered Compton	Bubble chamber	$\gamma p \longrightarrow \pi^- X$	2.8,4.7,9.3	-1. to 1.	0. to 1.0
SLAC[10]	Unsubtracted bremsstrahlung	Streamer chamber	$\gamma p \longrightarrow \pi^- X$	5.-18.	-1. to 0.1	0. to 0.8
Aachen-Hamburg-Heidelberg-Munchen[11]	Tagged photon	Streamer chamber	$\gamma p \longrightarrow \left\{\begin{matrix}\pi^\pm X\\ p\ X\end{matrix}\right.$	3.-6.3	-1. to 1.	0. to 1.0
DESY[12]	Subtracted bremsstrahlung	Spectrometer	$\gamma p \longrightarrow \left\{\begin{matrix}\pi^\pm X\\ K^\pm X\\ p\ X\end{matrix}\right.$	3.2,6.	.2 to 0.8	0.3 to 1.0
U. Wash.[13]	Collimated coherent bremsstrahlung	Spectrometer	$\gamma p \longrightarrow \left\{\begin{matrix}\pi^\pm X\\ p\ X\end{matrix}\right.$	9.8,13.8	-.3 to 0.0	0.2 to 1.0
Tel Aviv[14]	Backscattered Compton	Bubble chamber	$\gamma D \longrightarrow \left\{\begin{matrix}\pi^\pm X\\ \Delta\ X\\ \rho\ X\end{matrix}\right.$	7.5	-1. to 1.	0.0 to 1.
DESY[15]	Subtracted bremsstrahlung	Counter	$\gamma p \longrightarrow \pi^0 X$	6.	.2 to 0.8	0.2 to 1.3
UCSB[16]	Unsubtracted bremsstrahlung	Counter	$\gamma p \longrightarrow \pi^0 X$	21.	.3 to 1.	0.8 to 1.7

TABLE II. 20 GeV/c Spectrometer Parameters. The acceptance listed is that measured for this experiment. Other measured and calculated quantities are taken from the optics tests of ref. 25. These data were taken with the following source conditions: $\delta x=\pm 3$ cm, $\delta y=\pm 0.15$ cm, $\delta\theta=\pm 4.5$ mrad, $\delta\phi=\pm 8$ mrad, $\delta p/p=\pm 2\%$.

Length (target to p-focus):	43 m
Maximum momentum:	21 GeV
Momentum acceptance (nominal):	±1.75%
Momentum dispersion (measured):	3.26 cm/%
Momentum resolution (calculated):	± 0.06%
Horiz. angle (θ) range:	0. - 22.
θ acceptance (nominal):	±4.5 mrad
θ dispersion (measured):	1.62 cm/mrad
θ resolution (calculated):	± 0.25 mrad
Vertical angle acceptance (nominal):	±8 mrad
Acceptance ($d\Omega\, dp/p$, measured):	$6 \cdot 10^{-4}$ ster-%
(Hardware yields, $\theta=0$)	

THIS PAGE LEFT BLANK.

TABLE III. Corrections and uncertainties as a percentage of the final (subtracted) cross sections.

NORMALIZATION ERRORS:

Source	Correction	Uncertainty
SEQ-calorimeter calibration:	-	3.%
Bremsstrahlung calculation and collimation:	-	3.%
Target length and density:	-	0.7%
Electromagnetic absorption in target:	2.%	-
Stringent software acceptance:	-	3.%
Aperture counter vs stringent acceptance:	-	1.5%
Hodoscope and trigger counter absorption:	-	2.%
Bad hodoscope codes (software only):	5.-8.%	1.%
Total normalization error:		6.%

RANDOM ERRORS:

Source	Correction	Uncertainty
SEQ time dependence:	-	0.5%
Target density:	-	0.2%
Target contamination (D_2 only):	0.4%	0.3%
Tolerance in magnet settings:	-	0.-0.8%
Shower counter attenuator setting:	-	0.5%
Hardware dead-time:	0.-2.1%	0.-3.1%
Software rate dependence:	0.-5.7%	0.-8.4%
Muon accidentals (hardware yields only):	0.-10.%	-
Short-term reproducibility:	-	0.4-3.%
Computer sampling efficiency:	0.-30%	-
Total random errors		
$\pi^{\pm}$:		1.-4.%
$K^{\pm}$, p, and $\bar{p}$:		1.-10.%

TABLE III (continued)

SYSTEMATIC ERRORS:

Source	Correction	Uncertainty
SEQ energy dependence:	1.-3.%	0.2-2.7%
Bremsstrahlung subtraction:	0.-25.%	1.-10.%
Hadronic absorption in target:	1.-5.%	0.5-2.5%
Stringent and aperture counter acceptances (long targets, $\theta > 12^{o}$):	0.-2.5%	0.-2.5%
Relative acceptances:	0.-20.%	0.9%
Cross section variation over θ-acceptance:	0.-3.7%	-
Cross section variation over p-acceptance:	0.-1.5%	-
Uncertainty in spectrometer angle:	-	0.-2.7%
Uncertainty in spectrometer momentum:	-	0.-2.5%
Shower counter losses:	1.-10.%	0.3%
Differential counter absorption:	3.-40.%	0.6-4.0%
Hardware-software differences:	-	1.%
Hodoscope and trigger counter absorption:	7.-22.%	1.-3.%
Decay correction (pions):	6.-30.%	-
Decay corrections (kaons):	50.-890.%	0.4-1.9%
Muon identification (pions, <5 GeV/c):	0.-9.%	0.-0.9%
Kaon and proton detection efficiency:	7.-25%	2.-10.%
Proton contamination of pion yields:	0.-3.0%	0.-1.3%
Proton contamination of kaon yields:	0.-34%	0.-17%
Pion contamination of $\bar{p}$ yields:	0.-50.%	0.-25.%
Kaon contamination of $\bar{p}$ yields:	-	0.-20%
Total systematic errors		
$\pi^{\pm}$:		2.-7.%
p:		3.-10.%
K^{-}:		3.-16.%
$K^{+}, \bar{p}$:		3.-25.%

TABLE IV. Invariant cross sections for π^+ photoproduction from hydrogen and deuterium. See text for the definitions of the kinematic variables. The first uncertainty quoted with each cross section is that due to random errors; the second is that due to systematic errors.

k = 9 GeV

θ_{lab} (deg)	p_{lab} (GeV/c)	$p_\perp$ (GeV/c)	x	y_p	hydrogen (μb/GeV^2)	deuterium (μb/GeV^2)
1.486	4.159	0.11	0.44	0.77	(6.57+/-0.10+/-0.17) 10** 1	(1.18+/-0.02+/-0.03) 10** 2
5.985	4.773	0.50	0.47	0.64	(1.79+/-0.02+/-0.05) 10** 1	(3.04+/-0.05+/-0.08) 10** 1
9.986	5.749	1.00	0.51	0.46	(6.52+/-0.10+/-0.18) 10**-1	(1.06+/-0.02+/-0.03) 10** 0
17.985	3.226	1.00	0.16	1.05	(7.42+/-0.18+/-0.28) 10**-1	(1.29+/-0.04+/-0.05) 10** 0

k = 13 GeV

θ_{lab} (deg)	p_{lab} (GeV/c)	$p_\perp$ (GeV/c)	x	y_p	hydrogen (μb/GeV^2)
1.486	4.159	0.11	0.30	1.14	(6.88+/-0.28+/-0.21) 10** 1
1.486	9.415	0.24	0.69	0.32	(3.47+/-0.04+/-0.08) 10** 1
5.984	9.557	1.00	0.65	0.31	(5.62+/-0.08+/-0.15) 10**-1
17.984	5.168	1.60	0.10	0.95	(9.09+/-1.85+/-0.32) 10**-3

k = 18 GeV

θ_{lab} (deg)	p_{lab} (GeV/c)	$p_\perp$ (GeV/c)	x	y_p	hydrogen (μb/GeV^2)	deuterium (μb/GeV^2)
1.485	4.159	0.11	0.22	1.46	(8.08+/-0.17+/-0.37) 10** 1	(1.46+/-0.07+/-0.06) 10** 2
1.485	6.390	0.17	0.34	1.04	(5.91+/-0.28+/-0.16) 10** 1	(1.06+/-0.04+/-0.03) 10** 2
2.983	4.248	0.22	0.22	1.44	(7.45+/-0.16+/-0.31) 10** 1	(1.38+/-0.03+/-0.06) 10** 2
1.485	9.415	0.24	0.51	0.65	(4.29+/-0.08+/-0.10) 10** 1	(8.12+/-0.16+/-0.21) 10** 1
1.485	11.790	0.31	0.63	0.42	(3.08+/-0.04+/-0.08) 10** 1	(5.93+/-0.09+/-0.16) 10** 1
2.985	6.390	0.33	0.33	1.04	(4.40+/-0.22+/-0.11) 10** 1	
4.485	4.405	0.34	0.22	1.41	(4.91+/-0.13+/-0.19) 10** 1	(8.97+/-0.21+/-0.37) 10** 1
1.485	14.309	0.37	0.77	0.23	(1.46+/-0.01+/-0.04) 10** 1	(2.62+/-0.03+/-0.07) 10** 1
2.985	9.616	0.50	0.51	0.63	(1.47+/-0.04+/-0.04) 10** 1	(2.56+/-0.11+/-0.07) 10** 1
4.485	6.363	0.50	0.32	1.04	(1.83+/-0.06+/-0.05) 10** 1	(3.14+/-0.10+/-0.09) 10** 1
5.985	4.773	0.50	0.23	1.33	(2.11+/-0.04+/-0.07) 10** 1	(3.82+/-0.16+/-0.13) 10** 1
7.985	3.583	0.50	0.15	1.62	(2.49+/-0.09+/-0.12) 10** 1	(4.23+/-0.11+/-0.20) 10** 1
9.985	2.869	0.50	0.10	1.84	(2.28+/-0.11+/-0.15) 10** 1	(4.45+/-0.17+/-0.26) 10** 1
2.985	11.990	0.62	0.63	0.41	(5.62+/-0.19+/-0.15) 10** 0	
7.985	5.142	0.71	0.22	1.26	(5.76+/-0.11+/-0.19) 10** 0	(1.00+/-0.02+/-0.03) 10** 1
2.985	14.615	0.76	0.77	0.21	(1.57+/-0.04+/-0.05) 10** 0	(2.65+/-0.06+/-0.08) 10** 0
4.485	9.971	0.78	0.51	0.59	(2.88+/-0.06+/-0.08) 10** 0	(4.87+/-0.10+/-0.14) 10** 0
17.985	2.902	0.90	-0.00	1.85	(1.33+/-0.08+/-0.09) 10** 0	(2.41+/-0.14+/-0.16) 10** 0
3.832	14.900	1.00	0.77	0.19	(4.22+/-0.07+/-0.14) 10**-1	
4.485	12.736	1.00	0.65	0.35	(5.78+/-0.23+/-0.17) 10**-1	(1.02+/-0.02+/-0.03) 10** 0
4.967	11.504	1.00	0.57	0.45	(7.10+/-0.19+/-0.20) 10**-1	
5.985	9.557	1.00	0.46	0.64	(7.31+/-0.24+/-0.20) 10**-1	(1.40+/-0.03+/-0.04) 10** 0
6.802	8.414	1.00	0.39	0.76	(8.46+/-0.33+/-0.23) 10**-1	
7.985	7.175	1.00	0.31	0.92	(8.55+/-0.13+/-0.24) 10**-1	
9.985	5.749	1.00	0.21	1.15	(8.41+/-0.23+/-0.27) 10**-1	(1.55+/-0.04+/-0.05) 10** 0
11.985	4.800	1.00	0.14	1.33	(7.33+/-0.41+/-0.28) 10**-1	(1.60+/-0.09+/-0.06) 10** 0
14.984	3.854	1.00	0.06	1.56	(8.03+/-0.45+/-0.37) 10**-1	(1.43+/-0.06+/-0.07) 10** 0
17.984	3.226	1.00	-0.00	1.74	(7.34+/-0.28+/-0.43) 10**-1	(1.30+/-0.05+/-0.08) 10** 0
20.987	2.780	1.00	-0.05	1.90	(7.57+/-0.55+/-0.53) 10**-1	(1.23+/-0.07+/-0.09) 10** 0
4.485	15.154	1.19	0.77	0.17	(1.02+/-0.02+/-0.04) 10**-1	(1.69+/-0.03+/-0.06) 10**-1
10.762	6.408	1.20	0.22	1.04	(2.41+/-0.12+/-0.07) 10**-1	
17.986	3.873	1.20	0.00	1.56	(2.07+/-0.10+/-0.12) 10**-1	
5.985	13.190	1.38	0.63	0.31	(3.64+/-0.16+/-0.12) 10**-2	(6.14+/-0.18+/-0.20) 10**-2
11.539	6.980	1.40	0.22	0.96	(5.85+/-0.38+/-0.17) 10**-2	(1.06+/-0.06+/-0.03) 10**-1
17.987	4.520	1.40	0.00	1.41	(5.10+/-0.64+/-0.25) 10**-2	
7.986	11.486	1.60	0.50	0.45	(1.19+/-0.05+/-0.04) 10**-2	(2.13+/-0.07+/-0.08) 10**-2
9.986	9.204	1.60	0.34	0.68	(1.80+/-0.12+/-0.05) 10**-2	(2.97+/-0.24+/-0.09) 10**-2
11.985	7.686	1.60	0.23	0.86	(1.76+/-0.10+/-0.05) 10**-2	(3.32+/-0.14+/-0.10) 10**-2
14.984	6.172	1.60	0.10	1.09	(1.85+/-0.21+/-0.06) 10**-2	
17.987	5.168	1.60	0.00	1.27	(1.52+/-0.19+/-0.06) 10**-2	(2.31+/-0.23+/-0.09) 10**-2
20.985	4.455	1.60	-0.08	1.43	(1.25+/-0.22+/-0.07) 10**-2	
12.702	8.166	1.80	0.22	0.80	(4.67+/-0.46+/-0.14) 10**-3	
13.148	8.773	2.00	0.22	0.73	(1.38+/-0.18+/-0.05) 10**-3	
17.987	6.462	2.00	0.00	1.05	(7.82+/-2.89+/-0.29) 10**-4	

TABLE V. Invariant cross sections for π^- photoproduction from hydrogen and deuterium.

k = 9 GeV

θ_{lab} (deg)	p_{lab} (GeV/c)	$p_\perp$ (GeV/c)	x	y_p	hydrogen (μb/GeV^2)	deuterium (μb/GeV^2)
1.486	4.159	0.11	0.44	0.77	(6.00+/-0.09+/-0.16) 10** 1	(1.13+/-0.02+/-0.03) 10** 2
5.985	4.773	0.50	0.47	0.64	(1.49+/-0.02+/-0.04) 10** 1	(2.78+/-0.04+/-0.08) 10** 1
9.986	5.749	1.00	0.51	0.46	(4.08+/-0.07+/-0.12) 10**-1	(8.29+/-0.21+/-0.24) 10**-1
17.985	3.226	1.00	0.16	1.05	(5.84+/-0.17+/-0.21) 10**-1	(1.35+/-0.04+/-0.05) 10** 0

k = 13 GeV

θ_{lab} (deg)	p_{lab} (GeV/c)	$p_\perp$ (GeV/c)	x	y_p	hydrogen (μb/GeV^2)
1.486	4.159	0.11	0.30	1.14	(6.10+/-0.26+/-0.20) 10** 1
1.486	9.415	0.24	0.69	0.32	(3.24+/-0.04+/-0.08) 10** 1
5.984	9.557	1.00	0.65	0.31	(3.02+/-0.05+/-0.08) 10**-1
9.985	5.749	1.00	0.33	0.82	(6.85+/-0.29+/-0.19) 10**-1
17.984	3.226	1.00	0.06	1.42	(6.69+/-0.47+/-0.26) 10**-1
17.984	5.168	1.60	0.10	0.95	(1.16+/-0.17+/-0.04) 10**-2

k = 18 GeV

θ_{lab} (deg)	p_{lab} (GeV/c)	$p_\perp$ (GeV/c)	x	y_p	hydrogen (μb/GeV^2)	deuterium (μb/GeV^2)
1.485	4.159	0.11	0.22	1.46	(7.32+/-0.16+/-0.31) 10** 1	(1.34+/-0.08+/-0.06) 10** 2
1.485	6.390	0.17	0.34	1.04	(5.81+/-0.26+/-0.15) 10** 1	(1.05+/-0.04+/-0.03) 10** 2
2.983	4.248	0.22	0.22	1.44	(6.87+/-0.13+/-0.26) 10** 1	(1.32+/-0.02+/-0.05) 10** 2
1.485	9.415	0.24	0.51	0.65	(4.23+/-0.10+/-0.10) 10** 1	(8.02+/-0.17+/-0.20) 10** 1
1.485	11.790	0.31	0.63	0.42	(2.81+/-0.04+/-0.07) 10** 1	(5.69+/-0.08+/-0.16) 10** 1
2.985	6.390	0.33	0.33	1.04	(3.88+/-0.22+/-0.10) 10** 1	
4.485	4.405	0.34	0.22	1.41	(4.45+/-0.13+/-0.16) 10** 1	(8.67+/-0.22+/-0.34) 10** 1
1.485	14.309	0.37	0.77	0.23	(1.26+/-0.01+/-0.04) 10** 1	(2.47+/-0.03+/-0.08) 10** 1
2.985	9.616	0.50	0.51	0.63	(1.28+/-0.03+/-0.03) 10** 1	(2.45+/-0.09+/-0.07) 10** 1
4.485	6.363	0.50	0.32	1.04	(1.51+/-0.07+/-0.04) 10** 1	(3.01+/-0.10+/-0.09) 10** 1
5.984	4.773	0.50	0.23	1.33	(1.89+/-0.03+/-0.06) 10** 1	(3.55+/-0.07+/-0.12) 10** 1
7.985	3.583	0.50	0.15	1.62	(2.15+/-0.07+/-0.09) 10** 1	(4.00+/-0.12+/-0.18) 10** 1
9.985	2.869	0.50	0.10	1.84	(2.29+/-0.09+/-0.12) 10** 1	(4.27+/-0.13+/-0.23) 10** 1
2.985	11.990	0.62	0.63	0.41	(4.34+/-0.15+/-0.12) 10** 0	
7.985	5.142	0.71	0.22	1.26	(4.90+/-0.09+/-0.15) 10** 0	(9.27+/-0.21+/-0.30) 10** 0
2.985	14.615	0.76	0.77	0.21	(9.75+/-0.24+/-0.31) 10**-1	(1.94+/-0.07+/-0.06) 10** 0
4.485	9.971	0.78	0.51	0.59	(2.14+/-0.05+/-0.06) 10** 0	(4.21+/-0.08+/-0.12) 10** 0
17.985	2.902	0.90	-0.00	1.85	(1.19+/-0.05+/-0.08) 10** 0	(2.58+/-0.13+/-0.15) 10** 0
3.832	14.900	1.00	0.77	0.19	(2.17+/-0.05+/-0.07) 10**-1	
4.485	12.736	1.00	0.65	0.35	(3.69+/-0.09+/-0.11) 10**-1	(7.75+/-0.13+/-0.23) 10**-1
4.967	11.504	1.00	0.57	0.45	(4.97+/-0.13+/-0.14) 10**-1	
5.985	9.557	1.00	0.46	0.64	(6.22+/-0.19+/-0.17) 10**-1	(1.22+/-0.03+/-0.03) 10** 0
6.802	8.414	1.00	0.39	0.76	(7.25+/-0.27+/-0.19) 10**-1	
7.986	7.175	1.00	0.31	0.92	(7.48+/-0.20+/-0.21) 10**-1	
9.985	5.749	1.00	0.21	1.15	(7.91+/-0.20+/-0.23) 10**-1	(1.62+/-0.04+/-0.05) 10** 0
11.985	4.800	1.00	0.14	1.33	(7.35+/-0.30+/-0.25) 10**-1	(1.56+/-0.09+/-0.05) 10** 0
14.984	3.854	1.00	0.06	1.56	(7.07+/-0.39+/-0.31) 10**-1	(1.56+/-0.06+/-0.07) 10** 0
17.984	3.226	1.00	-0.00	1.74	(6.61+/-0.20+/-0.41) 10**-1	(1.43+/-0.05+/-0.08) 10** 0
20.985	2.780	1.00	-0.05	1.90	(6.14+/-0.51+/-0.49) 10**-1	(1.21+/-0.06+/-0.09) 10** 0
4.485	15.154	1.19	0.77	0.17	(5.12+/-0.13+/-0.18) 10**-2	(1.14+/-0.02+/-0.04) 10**-1
10.762	6.408	1.20	0.22	1.04	(2.16+/-0.09+/-0.06) 10**-1	
17.986	3.873	1.20	0.00	1.56	(1.79+/-0.10+/-0.10) 10**-1	
5.985	13.190	1.38	0.63	0.31	(2.76+/-0.14+/-0.09) 10**-2	(6.04+/-0.17+/-0.19) 10**-2
11.539	6.980	1.40	0.22	0.96	(6.21+/-0.37+/-0.18) 10**-2	(1.29+/-0.05+/-0.04) 10**-1
17.987	4.520	1.40	0.00	1.41	(4.52+/-0.59+/-0.22) 10**-2	
7.986	11.486	1.60	0.50	0.45	(1.01+/-0.05+/-0.03) 10**-2	(2.28+/-0.08+/-0.08) 10**-2
9.986	9.204	1.60	0.34	0.68	(1.44+/-0.13+/-0.04) 10**-2	(2.58+/-0.30+/-0.08) 10**-2
11.985	7.686	1.60	0.23	0.86	(1.54+/-0.09+/-0.05) 10**-2	(3.50+/-0.15+/-0.10) 10**-2
14.984	6.172	1.60	0.10	1.09	(1.37+/-0.21+/-0.04) 10**-2	
17.986	5.168	1.60	0.00	1.27	(1.30+/-0.14+/-0.05) 10**-2	(2.83+/-0.23+/-0.11) 10**-2
20.985	4.455	1.60	-0.08	1.43	(5.99+/-2.57+/-0.35) 10**-3	(2.84+/-0.51+/-0.16) 10**-2
12.702	8.166	1.80	0.22	0.80	(3.80+/-0.55+/-0.11) 10**-3	
13.148	8.773	2.00	0.22	0.73	(1.33+/-0.16+/-0.04) 10**-3	
17.987	6.462	2.00	0.00	1.05	(7.18+/-3.04+/-0.25) 10**-4	

TABLE VI. Invariant cross sections for K^+ photoproduction from hydrogen and deuterium.

k = 9 GeV

θ_{lab} (deg)	p_{lab} (GeV/c)	$p_\perp$ (GeV/c)	x	y_p	hydrogen (μb/GeV^2)	deuterium (μb/GeV^2)
1.486	4.159	0.11	0.41	0.77	(8.16+/-0.64+/-0.30) 10** 0	(1.69+/-0.14+/-0.06) 10** 1
5.985	4.773	0.50	0.45	0.63	(2.34+/-0.15+/-0.08) 10** 0	(4.21+/-0.30+/-0.15) 10** 0
9.986	5.749	1.00	0.49	0.45	(1.88+/-0.11+/-0.06) 10**-1	(2.98+/-0.23+/-0.10) 10**-1
17.985	3.226	1.00	0.13	1.04	(1.56+/-0.25+/-0.20) 10**-1	(7.37+/-5.51+/-0.97) 10**-2

k = 13 GeV

θ_{lab} (deg)	p_{lab} (GeV/c)	$p_\perp$ (GeV/c)	x	y_p	hydrogen (μb/GeV^2)
1.486	4.159	0.11	0.28	1.14	(4.81+/-2.43+/-0.19) 10** 0
1.486	9.415	0.24	0.68	0.32	(2.03+/-0.13+/-0.06) 10** 0
5.984	9.557	1.00	0.64	0.31	(1.91+/-0.08+/-0.06) 10**-1
17.984	5.168	1.60	0.08	0.94	(-1.85+/-3.24+/-0.08) 10**-3

k = 18 GeV

θ_{lab} (deg)	p_{lab} (GeV/c)	$p_\perp$ (GeV/c)	x	y_p	hydrogen (μb/GeV^2)	deuterium (μb/GeV^2)
1.485	4.159	0.11	0.19	1.46	(1.10+/-0.14+/-0.04) 10** 1	(1.91+/-0.53+/-0.08) 10** 1
1.485	6.390	0.17	0.32	1.03	(8.49+/-1.88+/-0.28) 10** 0	(1.02+/-0.22+/-0.04) 10** 1
2.983	4.248	0.22	0.19	1.44	(7.26+/-0.93+/-0.30) 10** 0	(1.29+/-0.12+/-0.06) 10** 1
1.485	9.415	0.24	0.49	0.65	(5.21+/-0.36+/-0.16) 10** 0	(8.31+/-0.53+/-0.27) 10** 0
1.485	11.790	0.31	0.62	0.42	(2.06+/-0.16+/-0.06) 10** 0	(3.54+/-0.23+/-0.11) 10** 0
2.985	6.390	0.33	0.32	1.03	(4.57+/-1.18+/-0.15) 10** 0	
4.485	4.405	0.34	0.20	1.41	(5.22+/-0.94+/-0.23) 10** 0	(9.12+/-1.15+/-0.43) 10** 0
1.485	14.309	0.37	0.76	0.23	(1.38+/-0.06+/-0.04) 10** 0	(2.26+/-0.10+/-0.06) 10** 0
2.985	9.616	0.50	0.49	0.63	(2.28+/-0.21+/-0.07) 10** 0	(2.79+/-0.58+/-0.09) 10** 0
4.485	6.363	0.50	0.30	1.04	(2.97+/-0.49+/-0.10) 10** 0	(3.29+/-0.65+/-0.12) 10** 0
5.985	4.773	0.50	0.20	1.33	(2.45+/-0.27+/-0.11) 10** 0	(2.64+/-1.25+/-0.14) 10** 0
7.985	3.583	0.50	0.12	1.61	(3.37+/-0.68+/-0.20) 10** 0	(3.16+/-0.72+/-0.24) 10** 0
9.985	2.869	0.50	0.06	1.84	(1.72+/-1.14+/-0.23) 10** 0	(3.37+/-1.37+/-0.45) 10** 0
2.985	11.990	0.62	0.62	0.41	(1.05+/-0.07+/-0.03) 10** 0	
7.985	5.142	0.71	0.20	1.26	(7.82+/-0.98+/-0.40) 10**-1	(1.41+/-0.18+/-0.08) 10** 0
2.985	14.615	0.76	0.76	0.21	(5.30+/-0.16+/-0.17) 10**-1	(8.89+/-0.28+/-0.29) 10**-1
4.485	9.971	0.78	0.49	0.59	(6.47+/-0.52+/-0.22) 10**-1	(1.01+/-0.09+/-0.03) 10** 0
17.985	2.902	0.90	-0.04	1.84	(1.80+/-0.98+/-0.29) 10**-1	(4.08+/-1.75+/-0.62) 10**-1
3.832	14.900	1.00	0.76	0.19	(1.71+/-0.08+/-0.06) 10**-1	
4.485	12.736	1.00	0.64	0.35	(2.01+/-0.40+/-0.07) 10**-1	(3.13+/-0.14+/-0.11) 10**-1
4.967	11.504	1.00	0.56	0.45	(1.62+/-0.19+/-0.06) 10**-1	
5.985	9.557	1.00	0.45	0.64	(2.07+/-0.24+/-0.07) 10**-1	(3.70+/-0.32+/-0.13) 10**-1
6.802	8.414	1.00	0.38	0.76	(1.43+/-0.33+/-0.05) 10**-1	
7.985	7.175	1.00	0.29	0.92	(1.90+/-0.11+/-0.07) 10**-1	
9.985	5.749	1.00	0.19	1.15	(2.13+/-0.24+/-0.08) 10**-1	(2.93+/-0.34+/-0.12) 10**-1
11.985	4.800	1.00	0.12	1.33	(1.50+/-0.47+/-0.07) 10**-1	(2.73+/-0.96+/-0.13) 10**-1
14.984	3.854	1.00	0.03	1.55	(2.84+/-0.62+/-0.16) 10**-1	(4.22+/-0.69+/-0.25) 10**-1
17.984	3.226	1.00	-0.04	1.74	(1.06+/-0.40+/-0.15) 10**-1	(1.56+/-0.65+/-0.23) 10**-1
20.987	2.780	1.00	-0.10	1.89	(7.85+/-8.33+/-1.83) 10**-2	(2.08+/-1.00+/-0.48) 10**-1
4.485	15.154	1.19	0.76	0.17	(4.82+/-0.22+/-0.18) 10**-2	(6.95+/-0.28+/-0.26) 10**-2
10.762	6.408	1.20	0.20	1.04	(5.91+/-1.33+/-0.22) 10**-2	
17.985	3.873	1.20	-0.03	1.56	(6.92+/-1.21+/-0.50) 10**-2	
5.985	13.190	1.38	0.63	0.31	(1.37+/-0.18+/-0.05) 10**-2	(2.66+/-0.21+/-0.09) 10**-2
11.539	6.980	1.40	0.21	0.96	(2.49+/-0.45+/-0.09) 10**-2	(3.35+/-0.69+/-0.12) 10**-2
17.987	4.520	1.40	-0.02	1.40	(1.57+/-0.93+/-0.08) 10**-2	
7.986	11.486	1.60	0.49	0.45	(4.22+/-0.63+/-0.15) 10**-3	(8.13+/-0.81+/-0.30) 10**-3
9.986	9.204	1.60	0.33	0.68	(5.96+/-1.38+/-0.21) 10**-3	(9.46+/-2.70+/-0.34) 10**-3
11.985	7.686	1.60	0.22	0.86	(5.42+/-1.13+/-0.19) 10**-3	(1.04+/-0.16+/-0.04) 10**-2
14.984	6.172	1.60	0.08	1.09	(8.40+/-3.08+/-0.32) 10**-3	
17.987	5.168	1.60	-0.02	1.27	(5.24+/-2.68+/-0.24) 10**-3	(8.10+/-3.04+/-0.39) 10**-3
20.985	4.455	1.60	-0.11	1.43	(4.93+/-2.59+/-0.30) 10**-3	
12.702	8.166	1.80	0.21	0.80	(7.24+/-6.68+/-0.27) 10**-4	
13.148	8.773	2.00	0.21	0.73	(4.23+/-2.00+/-0.15) 10**-4	
17.987	6.462	2.00	-0.01	1.05	(-0.15+/-4.09+/-0.02) 10**-4	

TABLE VII. Invariant cross sections for K^- photoproduction from hydrogen and deuterium.

k = 9 GeV

θ_{lab} (deg)	p_{lab} (GeV/c)	$p_\perp$ (GeV/c)	x	y_p	hydrogen (μb/GeV^2)	deuterium (μb/GeV^2)
1.486	4.159	0.11	0.41	0.77	(4.69+/-0.42+/-0.17) 10** 0	(1.05+/-0.09+/-0.04) 10** 1
5.985	4.773	0.50	0.45	0.63	(1.09+/-0.06+/-0.04) 10** 0	(1.76+/-0.14+/-0.06) 10** 0
9.986	5.749	1.00	0.49	0.45	(4.44+/-0.38+/-0.16) 10**-2	(8.11+/-0.98+/-0.29) 10**-2
17.985	3.226	1.00	0.13	1.04	(4.63+/-1.51+/-0.52) 10**-2	(1.33+/-0.35+/-0.15) 10**-1

k = 13 GeV

θ_{lab} (deg)	p_{lab} (GeV/c)	$p_\perp$ (GeV/c)	x	y_p	hydrogen (μb/GeV^2)
1.486	4.159	0.11	0.28	1.14	(2.02+/-1.82+/-0.08) 10** 0
1.486	9.415	0.24	0.68	0.32	(8.44+/-0.61+/-0.24) 10**-1
5.984	9.557	1.00	0.64	0.31	(3.92+/-0.24+/-0.13) 10**-2
9.985	5.749	1.00	0.31	0.82	(7.41+/-1.96+/-0.25) 10**-2
17.984	3.226	1.00	0.03	1.41	(2.81+/-4.95+/-0.32) 10**-2
17.984	5.168	1.60	0.08	0.94	(-2.52+/-1.35+/-0.10) 10**-3

k = 18 GeV

θ_{lab} (deg)	p_{lab} (GeV/c)	$p_\perp$ (GeV/c)	x	y_p	hydrogen (μb/GeV^2)	deuterium (μb/GeV^2)
1.485	4.159	0.11	0.19	1.46	(5.78+/-1.09+/-0.23) 10** 0	(1.13+/-0.60+/-0.05) 10** 1
1.485	6.390	0.17	0.32	1.03	(2.26+/-1.35+/-0.08) 10** 0	(5.89+/-1.60+/-0.21) 10** 0
2.983	4.248	0.22	0.19	1.44	(5.50+/-0.60+/-0.21) 10** 0	(1.03+/-0.09+/-0.04) 10** 1
1.485	9.415	0.24	0.49	0.65	(3.50+/-0.28+/-0.10) 10** 0	(6.36+/-0.40+/-0.19) 10** 0
1.485	11.790	0.31	0.62	0.42	(1.12+/-0.10+/-0.03) 10** 0	(1.80+/-0.14+/-0.05) 10** 0
2.985	6.390	0.33	0.32	1.03	(2.49+/-0.94+/-0.08) 10** 0	
4.485	4.405	0.34	0.20	1.41	(2.92+/-0.72+/-0.11) 10** 0	(7.30+/-0.93+/-0.28) 10** 0
1.485	14.309	0.37	0.76	0.23	(5.46+/-0.26+/-0.15) 10**-1	(1.13+/-0.04+/-0.03) 10** 0
2.985	9.616	0.50	0.49	0.63	(1.08+/-0.11+/-0.03) 10** 0	(2.21+/-0.26+/-0.07) 10** 0
4.485	6.363	0.50	0.30	1.04	(1.72+/-0.39+/-0.05) 10** 0	(3.37+/-0.52+/-0.11) 10** 0
5.984	4.773	0.50	0.20	1.33	(1.70+/-0.20+/-0.06) 10** 0	(3.22+/-0.33+/-0.12) 10** 0
7.985	3.583	0.50	0.12	1.61	(1.73+/-0.44+/-0.08) 10** 0	(3.66+/-0.60+/-0.18) 10** 0
9.985	2.869	0.50	0.06	1.84	(2.13+/-6.94+/-0.35) 10**-1	(2.20+/-0.83+/-0.28) 10** 0
2.985	11.990	0.62	0.62	0.41	(4.26+/-0.34+/-0.13) 10**-1	
7.985	5.142	0.71	0.20	1.26	(6.69+/-0.62+/-0.24) 10**-1	(1.20+/-0.13+/-0.04) 10** 0
2.985	14.615	0.76	0.76	0.21	(1.24+/-0.06+/-0.04) 10**-1	(2.65+/-0.19+/-0.09) 10**-1
4.485	9.971	0.78	0.49	0.59	(2.65+/-0.31+/-0.08) 10**-1	(5.94+/-0.35+/-0.19) 10**-1
17.985	2.902	0.90	-0.04	1.84	(4.96+/-3.96+/-0.76) 10**-2	(2.03+/-0.92+/-0.31) 10**-1
3.832	14.900	1.00	0.76	0.19	(2.93+/-0.30+/-0.11) 10**-2	
4.485	12.736	1.00	0.64	0.35	(7.17+/-0.51+/-0.24) 10**-2	(1.26+/-0.07+/-0.04) 10**-1
4.967	11.504	1.00	0.56	0.45	(6.60+/-0.72+/-0.21) 10**-2	
5.985	9.557	1.00	0.45	0.64	(9.74+/-1.26+/-0.31) 10**-2	(1.87+/-0.17+/-0.06) 10**-1
6.802	8.414	1.00	0.38	0.76	(1.22+/-0.18+/-0.04) 10**-1	
7.986	7.175	1.00	0.29	0.92	(1.13+/-0.14+/-0.04) 10**-1	
9.985	5.749	1.00	0.19	1.15	(1.35+/-0.15+/-0.05) 10**-1	(2.62+/-0.24+/-0.09) 10**-1
11.985	4.800	1.00	0.12	1.33	(1.54+/-0.24+/-0.06) 10**-1	(4.53+/-6.28+/-0.30) 10**-2
14.984	3.854	1.00	0.03	1.55	(1.36+/-0.36+/-0.08) 10**-1	(1.44+/-0.47+/-0.10) 10**-1
17.984	3.226	1.00	-0.04	1.74	(6.96+/-2.18+/-0.92) 10**-2	(2.09+/-0.49+/-0.29) 10**-1
20.985	2.780	1.00	-0.10	1.89	(7.57+/-5.47+/-1.27) 10**-2	(1.29+/-0.67+/-0.21) 10**-1
4.485	15.154	1.19	0.76	0.17	(5.50+/-0.59+/-0.21) 10**-3	(1.25+/-0.08+/-0.05) 10**-2
10.762	6.408	1.20	0.20	1.04	(4.27+/-0.66+/-0.14) 10**-2	
17.986	3.873	1.20	-0.03	1.56	(3.34+/-0.90+/-0.24) 10**-2	
5.985	13.190	1.38	0.63	0.31	(4.94+/-0.84+/-0.17) 10**-3	(8.82+/-0.93+/-0.33) 10**-3
11.539	6.980	1.40	0.21	0.96	(1.45+/-0.30+/-0.05) 10**-2	(1.99+/-0.33+/-0.07) 10**-2
17.987	4.520	1.40	-0.02	1.40	(9.95+/-6.16+/-0.52) 10**-3	
7.986	11.486	1.60	0.49	0.45	(1.50+/-0.32+/-0.05) 10**-3	(2.50+/-0.44+/-0.10) 10**-3
9.986	9.204	1.60	0.33	0.68	(3.62+/-0.91+/-0.13) 10**-3	(5.03+/-2.10+/-0.18) 10**-3
11.985	7.686	1.60	0.22	0.86	(3.08+/-0.71+/-0.11) 10**-3	(6.37+/-1.06+/-0.23) 10**-3
14.984	6.172	1.60	0.08	1.09	(4.12+/-1.61+/-0.15) 10**-3	
17.986	5.168	1.60	-0.02	1.27	(2.62+/-1.13+/-0.10) 10**-3	(3.04+/-1.72+/-0.13) 10**-3
20.985	4.455	1.60	-0.11	1.43	(3.54+/-3.13+/-0.25) 10**-3	(5.34+/-5.16+/-0.28) 10**-3
12.702	8.166	1.80	0.21	0.80	(1.17+/-0.42+/-0.04) 10**-3	
13.148	8.773	2.00	0.21	0.73	(3.05+/-1.14+/-0.11) 10**-4	
17.987	6.462	2.00	-0.01	1.05	(1.38+/-1.54+/-0.06) 10**-4	

TABLE VIII. Invariant cross sections for proton photoproduction from hydrogen and deuterium.

k = 9 GeV

θ_{lab} (deg)	p_{lab} (GeV/c)	$p_\perp$ (GeV/c)	x	y_p	hydrogen (μb/GeV^2)	deuterium (μb/GeV^2)
1.486	4.159	0.11	0.33	0.76	(7.31+/-0.33+/-0.41) 10** 0	(1.30+/-0.07+/-0.08) 10** 1
5.985	4.773	0.50	0.38	0.63	(3.06+/-0.09+/-0.17) 10** 0	(5.37+/-0.22+/-0.31) 10** 0
9.986	5.749	1.00	0.43	0.45	(2.41+/-0.08+/-0.08) 10**-1	(4.46+/-0.19+/-0.16) 10**-1
17.985	3.226	1.00	0.03	1.03	(7.14+/-0.28+/-0.34) 10**-1	(1.28+/-0.07+/-0.06) 10** 0

k = 13 GeV

θ_{lab} (deg)	p_{lab} (GeV/c)	$p_\perp$ (GeV/c)	x	y_p	hydrogen (μb/GeV^2)	deuterium (μb/GeV^2)
1.486	4.159	0.11	0.20	1.13	(1.01+/-0.12+/-0.05) 10** 1	
1.486	9.415	0.24	0.65	0.32	(9.11+/-0.60+/-0.26) 10**-1	
5.984	9.557	1.00	0.60	0.31	(1.20+/-0.04+/-0.04) 10**-1	
17.984	5.168	1.60	0.02	0.94	(1.13+/-0.32+/-0.04) 10**-2	

k = 18 GeV

θ_{lab} (deg)	p_{lab} (GeV/c)	$p_\perp$ (GeV/c)	x	y_p	hydrogen (μb/GeV^2)	deuterium (μb/GeV^2)
1.485	4.159	0.11	0.12	1.45	(8.41+/-0.67+/-0.52) 10** 0	(1.29+/-0.25+/-0.09) 10** 1
1.485	6.390	0.17	0.27	1.03	(5.24+/-0.93+/-0.16) 10** 0	(9.30+/-1.07+/-0.31) 10** 0
2.984	4.248	0.22	0.12	1.43	(6.66+/-0.55+/-0.41) 10** 0	(1.26+/-0.08+/-0.08) 10** 1
1.485	9.415	0.24	0.46	0.65	(2.51+/-0.18+/-0.07) 10** 0	(4.59+/-0.28+/-0.14) 10** 0
1.485	11.790	0.31	0.60	0.42	(1.18+/-0.07+/-0.03) 10** 0	(1.93+/-0.11+/-0.06) 10** 0
2.985	6.390	0.33	0.27	1.03	(4.12+/-0.68+/-0.13) 10** 0	
4.485	4.405	0.34	0.12	1.40	(5.67+/-0.52+/-0.34) 10** 0	(9.16+/-0.78+/-0.57) 10** 0
1.485	14.309	0.37	0.74	0.23	(3.60+/-0.19+/-0.10) 10**-1	(6.50+/-0.30+/-0.20) 10**-1
2.985	9.616	0.50	0.46	0.63	(1.81+/-0.12+/-0.05) 10** 0	(3.08+/-0.34+/-0.10) 10** 0
4.485	6.363	0.50	0.25	1.04	(2.91+/-0.30+/-0.09) 10** 0	(4.41+/-0.45+/-0.15) 10** 0
5.985	4.773	0.50	0.14	1.32	(3.06+/-0.17+/-0.18) 10** 0	(5.92+/-0.82+/-0.34) 10** 0
7.985	3.583	0.50	0.03	1.60	(3.40+/-0.53+/-0.24) 10** 0	(7.20+/-0.69+/-0.49) 10** 0
9.985	2.869	0.50	-0.05	1.82	(4.81+/-0.82+/-0.49) 10** 0	(8.28+/-1.32+/-0.76) 10** 0
2.985	11.990	0.62	0.59	0.41	(6.11+/-0.35+/-0.19) 10**-1	
7.985	5.142	0.71	0.14	1.25	(1.37+/-0.07+/-0.06) 10** 0	(2.37+/-0.16+/-0.10) 10** 0
2.985	14.615	0.76	0.74	0.21	(1.44+/-0.05+/-0.05) 10**-1	(2.49+/-0.09+/-0.08) 10**-1
4.485	9.971	0.78	0.46	0.59	(5.75+/-0.30+/-0.18) 10**-1	(9.70+/-0.53+/-0.33) 10**-1
17.985	2.902	0.90	-0.15	1.82	(1.21+/-0.10+/-0.12) 10** 0	(2.40+/-0.18+/-0.21) 10** 0
3.832	14.900	1.00	0.74	0.19	(4.39+/-0.26+/-0.15) 10**-2	
4.485	12.736	1.00	0.61	0.35	(9.80+/-1.12+/-0.33) 10**-2	(1.72+/-0.07+/-0.06) 10**-1
4.967	11.504	1.00	0.54	0.45	(1.43+/-0.12+/-0.05) 10**-1	
5.985	9.557	1.00	0.41	0.63	(1.64+/-0.15+/-0.05) 10**-1	(3.85+/-0.21+/-0.13) 10**-1
6.802	8.414	1.00	0.34	0.76	(2.47+/-0.25+/-0.08) 10**-1	
7.985	7.175	1.00	0.25	0.92	(2.56+/-0.09+/-0.09) 10**-1	
9.985	5.749	1.00	0.14	1.14	(3.07+/-0.20+/-0.11) 10**-1	(6.04+/-0.36+/-0.23) 10**-1
11.985	4.800	1.00	0.05	1.32	(3.50+/-0.41+/-0.17) 10**-1	(6.23+/-0.91+/-0.30) 10**-1
14.984	3.854	1.00	-0.05	1.54	(5.07+/-0.62+/-0.30) 10**-1	(1.04+/-0.09+/-0.06) 10** 0
17.984	3.226	1.00	-0.14	1.72	(6.45+/-0.44+/-0.48) 10**-1	(1.28+/-0.08+/-0.09) 10** 0
20.987	2.780	1.00	-0.21	1.87	(1.03+/-0.11+/-0.08) 10** 0	(1.75+/-0.18+/-0.13) 10** 0
4.485	15.154	1.19	0.74	0.17	(1.17+/-0.08+/-0.04) 10**-2	(2.12+/-0.10+/-0.08) 10**-2
10.762	6.408	1.20	0.15	1.04	(9.61+/-1.29+/-0.33) 10**-2	
17.986	3.873	1.20	-0.11	1.55	(1.95+/-0.15+/-0.10) 10**-1	
5.985	13.190	1.38	0.60	0.31	(4.54+/-1.08+/-0.16) 10**-3	(1.42+/-0.12+/-0.05) 10**-2
11.539	6.980	1.40	0.16	0.95	(2.91+/-0.43+/-0.10) 10**-2	(6.09+/-0.74+/-0.22) 10**-2
17.987	4.520	1.40	-0.10	1.40	(5.50+/-0.93+/-0.25) 10**-2	
7.986	11.486	1.60	0.46	0.45	(3.17+/-0.41+/-0.11) 10**-3	(6.84+/-0.57+/-0.31) 10**-3
9.986	9.204	1.60	0.30	0.68	(6.15+/-1.09+/-0.22) 10**-3	(6.59+/-2.22+/-0.25) 10**-3
11.985	7.686	1.60	0.17	0.86	(8.98+/-1.04+/-0.31) 10**-3	(1.62+/-0.16+/-0.06) 10**-2
14.984	6.172	1.60	0.03	1.08	(1.42+/-0.28+/-0.05) 10**-2	
17.987	5.168	1.60	-0.08	1.26	(1.23+/-0.29+/-0.05) 10**-2	(2.62+/-0.36+/-0.11) 10**-2
20.985	4.455	1.60	-0.18	1.42	(1.47+/-0.41+/-0.08) 10**-2	
12.702	8.166	1.80	0.17	0.80	(2.62+/-0.58+/-0.09) 10**-3	
13.148	8.773	2.00	0.17	0.73	(6.86+/-2.05+/-0.24) 10**-4	
17.987	6.462	2.00	-0.07	1.04	(1.97+/-0.40+/-0.07) 10**-3	

TABLE IX. Invariant cross sections for $\bar{p}$ photoproduction from hydrogen and deuterium.

k = 9 GeV

θ_{lab} (deg)	p_{lab} (GeV/c)	$p_\perp$ (GeV/c)	x	y_p	hydrogen (μb/GeV^2)	deuterium (μb/GeV^2)
1.486	4.159	0.11	0.33	0.76	(6.09+/-0.95+/-1.72) 10**-1	(6.93+/-2.19+/-2.85) 10**-1
5.985	4.773	0.50	0.38	0.63	(1.86+/-0.17+/-0.48) 10**-1	(4.31+/-0.39+/-1.06) 10**-1
9.986	5.749	1.00	0.43	0.45	(3.49+/-0.62+/-0.16) 10**-3	(7.15+/-1.72+/-0.37) 10**-3
17.985	3.226	1.00	0.03	1.03	(9.24+/-2.63+/-2.58) 10**-3	(1.93+/-0.64+/-0.57) 10**-2

k = 13 GeV

θ_{lab} (deg)	p_{lab} (GeV/c)	$p_\perp$ (GeV/c)	x	y_p	hydrogen (μb/GeV^2)
1.486	4.159	0.11	0.20	1.13	(1.22+/-0.44+/-0.25) 10** 0
1.486	9.415	0.24	0.65	0.32	(8.49+/-1.19+/-0.29) 10**-2
5.984	9.557	1.00	0.60	0.31	(3.04+/-0.44+/-0.11) 10**-3
9.985	5.749	1.00	0.25	0.82	(2.32+/-0.50+/-0.08) 10**-2
17.984	3.226	1.00	-0.07	1.40	(1.16+/-0.92+/-0.31) 10**-2
17.984	5.168	1.60	0.02	0.94	(-1.70+/-3.57+/-0.15) 10**-4

k = 18 GeV

θ_{lab} (deg)	p_{lab} (GeV/c)	$p_\perp$ (GeV/c)	x	y_p	hydrogen (μb/GeV^2)	deuterium (μb/GeV^2)
1.485	4.159	0.11	0.12	1.45	(1.67+/-0.28+/-0.34) 10** 0	(6.73+/-1.65+/-1.26) 10** 0
1.485	6.390	0.17	0.27	1.03	(8.62+/-3.24+/-0.27) 10**-1	(2.49+/-0.41+/-0.10) 10** 0
2.983	4.248	0.22	0.12	1.43	(1.48+/-0.18+/-0.27) 10** 0	(2.73+/-0.27+/-0.52) 10** 0
1.485	9.415	0.24	0.46	0.65	(4.84+/-0.78+/-0.14) 10**-1	(8.50+/-0.99+/-0.31) 10**-1
1.485	11.790	0.31	0.60	0.42	(1.68+/-0.26+/-0.05) 10**-1	(3.32+/-0.37+/-0.13) 10**-1
2.985	6.390	0.33	0.27	1.03	(6.60+/-2.77+/-0.21) 10**-1	
4.485	4.405	0.34	0.12	1.40	(1.25+/-0.23+/-0.20) 10** 0	(2.21+/-0.30+/-0.37) 10** 0
1.485	14.309	0.37	0.74	0.23	(2.13+/-0.42+/-0.08) 10**-2	(5.43+/-0.56+/-0.30) 10**-2
2.985	9.616	0.50	0.46	0.63	(2.66+/-0.32+/-0.08) 10**-1	(5.68+/-0.81+/-0.20) 10**-1
4.485	6.363	0.50	0.25	1.04	(6.16+/-1.28+/-0.19) 10**-1	(1.21+/-0.17+/-0.04) 10** 0
5.984	4.773	0.50	0.14	1.32	(7.07+/-0.67+/-1.10) 10**-1	(1.38+/-0.11+/-0.23) 10** 0
7.985	3.583	0.50	0.03	1.60	(6.23+/-1.20+/-0.95) 10**-1	(8.82+/-1.61+/-1.56) 10**-1
9.985	2.869	0.50	-0.05	1.82	(3.24+/-1.55+/-0.61) 10**-1	(6.02+/-1.81+/-1.18) 10**-1
2.985	11.990	0.62	0.59	0.41	(7.61+/-0.84+/-0.25) 10**-2	
7.985	5.142	0.71	0.14	1.25	(2.47+/-0.20+/-0.11) 10**-1	(4.23+/-0.41+/-0.21) 10**-1
2.985	14.615	0.76	0.74	0.21	(7.05+/-0.46+/-0.25) 10**-3	(1.41+/-0.14+/-0.06) 10**-2
4.485	9.971	0.78	0.46	0.59	(1.05+/-0.11+/-0.03) 10**-1	(1.87+/-0.11+/-0.07) 10**-1
17.985	2.902	0.90	-0.15	1.82	(3.59+/-0.79+/-0.70) 10**-2	(4.68+/-1.92+/-0.99) 10**-2
3.832	14.900	1.00	0.74	0.19	(1.39+/-0.37+/-0.06) 10**-3	
4.485	12.736	1.00	0.61	0.35	(1.07+/-0.13+/-0.04) 10**-2	(2.04+/-0.17+/-0.08) 10**-2
4.967	11.504	1.00	0.54	0.45	(1.39+/-0.21+/-0.05) 10**-2	
5.985	9.557	1.00	0.41	0.63	(2.70+/-0.40+/-0.09) 10**-2	(5.29+/-0.52+/-0.20) 10**-2
6.802	8.414	1.00	0.34	0.76	(3.96+/-0.60+/-0.13) 10**-2	
7.986	7.175	1.00	0.25	0.92	(3.52+/-0.46+/-0.13) 10**-2	
9.985	5.749	1.00	0.14	1.14	(3.07+/-0.44+/-0.11) 10**-2	(7.94+/-0.74+/-0.32) 10**-2
11.985	4.800	1.00	0.05	1.32	(4.09+/-0.72+/-0.71) 10**-2	(9.92+/-2.08+/-1.66) 10**-2
14.984	3.854	1.00	-0.05	1.54	(2.01+/-0.94+/-0.40) 10**-2	(7.16+/-1.43+/-1.17) 10**-2
17.984	3.226	1.00	-0.14	1.72	(1.57+/-0.44+/-0.37) 10**-2	(3.69+/-1.04+/-0.78) 10**-2
20.985	2.780	1.00	-0.21	1.87	(-0.23+/-1.16+/-0.15) 10**-2	(2.30+/-1.47+/-0.46) 10**-2
4.485	15.154	1.19	0.74	0.17	(1.54+/-1.06+/-0.09) 10**-4	(2.12+/-0.58+/-0.17) 10**-4
10.762	6.408	1.20	0.15	1.04	(8.75+/-1.98+/-0.31) 10**-3	
17.986	3.873	1.20	-0.11	1.55	(1.74+/-2.10+/-0.57) 10**-3	
5.985	13.190	1.38	0.60	0.31	(4.87+/-1.47+/-0.20) 10**-4	(8.37+/-1.80+/-0.37) 10**-4
11.539	6.980	1.40	0.16	0.95	(2.22+/-0.73+/-0.08) 10**-3	(5.82+/-0.94+/-0.24) 10**-3
17.987	4.520	1.40	-0.10	1.40	(2.19+/-1.31+/-0.52) 10**-3	
7.986	11.486	1.60	0.46	0.45	(2.01+/-0.76+/-0.08) 10**-4	(6.08+/-1.29+/-0.33) 10**-4
9.986	9.204	1.60	0.30	0.68	(8.78+/-2.83+/-0.34) 10**-4	(2.01+/-0.66+/-0.08) 10**-3
11.985	7.686	1.60	0.17	0.86	(4.34+/-1.99+/-0.17) 10**-4	(1.19+/-0.30+/-0.05) 10**-3
14.984	6.172	1.60	0.03	1.08	(7.53+/-3.23+/-0.34) 10**-4	
17.986	5.168	1.60	-0.08	1.26	(3.82+/-2.43+/-0.24) 10**-4	(8.91+/-4.31+/-0.54) 10**-4
20.985	4.455	1.60	-0.18	1.42	(-7.19+/-4.09+/-0.36) 10**-4	(-1.35+/-6.67+/-1.02) 10**-4
12.702	8.166	1.80	0.17	0.80	(1.38+/-0.93+/-0.05) 10**-4	
13.148	8.773	2.00	0.17	0.73	(-1.29+/-5.19+/-0.05) 10**-5	
17.987	6.462	2.00	-0.07	1.04	(7.04+/-4.41+/-0.29) 10**-5	

TABLE X. Parameters obtained from the empirical fits to the 18 GeV invariant cross sections. The fits were of the form

$$E\frac{d^3\sigma}{dp^3}(x', p_\perp) = 1000 \sum_{n=1}^{4} \left(A_n + B_n\, e^{-(C_n p_\perp)^2}\right)(1-x')^n\, e^{-D\mu}$$

Parameters indicated with a * were constrained to a common value. The column labelled Reaction specifies hydrogen (H) or deuterium (D) target and the detected particle.

Reaction	A1	B1	C1	A2	B2	C1	A3	B3	C3	A4	B4	C4	D	χ^2/d.f.
	$\frac{\mu b}{GeV^2}$	$\frac{\mu b}{GeV^2}$	GeV^{-1}	$\frac{\mu b}{GeV^2}$	$\frac{\mu b}{GeV^2}$	GeV^{-1}	$\frac{\mu b}{GeV^2}$	$\frac{\mu b}{GeV^2}$	GeV^{-1}	$\frac{\mu b}{GeV^2}$	$\frac{\mu b}{GeV^2}$	GeV^{-1}	GeV^{-1}	
H π^+	5.423	-5.007	1.276	-8.576	12.207	1.766	8.593	-20.98	2.299	-3.962	13.67	2.450	7.139	3.8
D π^+	7.076	-6.506	1.427	-11.17	21.66	2.009	12.70	-45.50	2.384	-6.554	31.44	2.444	7.030	6.8
H π^-	1.154	-0.319	1.395	-0.531	1.906	2.775	0.899	-8.877	2.796	-0.992	7.709	2.580	6.597	1.4
D π^-	2.300	-0.756	1.434	-2.224	6.456	2.698	3.386	-23.81	2.877	-2.432	19.37	2.783	6.463	1.3
H K^+	3.175	-3.254	1.565*	-10.19	9.396	1.565*	12.71	-6.862	1.565*	-5.284	-	-	6.662	1.4
D K^+	3.699	-4.187	1.875*	-10.18	10.99	1.875*	11.44	-7.277	1.875*	-4.523	-	-	6.542	1.3
H K^-	0.294	-0.281	2.076*	-0.082	0.372	2.076*	0.115	-	-	-0.167	-	-	6.444	1.3
D K^-	1.191	-1.126	1.874*	-1.402	1.178	1.874*	2.529	-	-	-1.959	-	-	6.944	3.1
H p	0.130	-10.43	2.008*	45.82	11.26	2.008*	-69.34	-	-	36.77	-	-	7.527	1.3
D p	2.078	-16.64	1.652*	78.33	13.33	1.652*	-115.0	-	-	62.73	-	-	7.571	1.2
H $\bar{p}$	2.223	-5.774	1.339*	17.39	7.890	1.339*	-15.34	-	-	-	-	-	8.599	1.5
D $\bar{p}$	0.104	-31.34	3.953*	37.51	40.49	3.953*	-30.30	-	-	-	-	-	8.386	1.2

Table XI. Fitted slope parameters for 18 GeV invariant cross sections for $\gamma p \rightarrow c\ X$ at $x=0.2$, $\mu > 0.5$ GeV/c. Fits were of the form

$$E \frac{d^3\sigma}{dp^3} = A e^{b\mu}$$

c	slope b $(GeV/c)^{-1}$	χ^2/d.f.
π^+	-6.570+/-0.033	15/6
π^-	-6.518+/-0.034	3/6
K^+	-6.336+/-0.128	9/9
K^-	-6.368+/-0.122	3/9
p	-7.384+/-0.096	4/9
$\bar{p}$	-9.189+/-0.240	7/9

Table XII. Relative signs of Regge exchange amplitudes of isospin I, G-parity G, and charge conjugation C, for the inclusive photoproduction reactions (i,j), where i=p,n designates the target and j=+,- designates the charge of the detected particle.

Amplitude	IG(C)	(p,+)	(p,-)	(n,+)	(n,-)
P,f	0+(+)	+	+	+	+
ω	0-(-)	+	-	+	-
ρ	1+(-)	+	-	-	+
A_2	1-(+)	+	+	-	-

Table XIII. Fitted parameters for $\gamma p \longrightarrow c\ X$ at x=0.2, $p_\perp \geqslant 0.5$ GeV/c, from the constituent interchange model. The fit was of the form

$$E\frac{d^3\sigma}{dp^3} = \frac{\epsilon^{P_f}}{\left(p_\perp^2 + M^2\right)^N}$$

Reaction	f	P	N	M	χ^2/d.f
π^+	77.	0.71+/-0.09	6.2+/-0.2	0.97	19/11
π^-	38.	1.17+/-0.09	5.5+/-0.2	0.90	29/13
K^+	10600.	0.80+/-0.33	8.7+/-2.1	1.52	10/8
K^-	72.	1.80+/-0.30	5.9+/-1.2	1.19	22/10
$\bar{p}$	66.	1.84+/-0.37	7.1+/-2.0	1.18	7/8

FIGURE CAPTIONS

Fig. 1. Schematic of the photon beam line and experimental layout. The 1.6 and 8 GeV/c spectrometers were not used in this experiment.

Fig. 2. Effective beam energy spectrum after subtraction. $B(E_0,k)$ is the bremsstrahlung function normalized such that the number of photons per GeV per equivalent quantum at energy k for a bremsstrahlung beam of endpoint energy E_0 is given by $B(E_0,k)/k$.

Fig. 3. Plan and elevation views of the SLAC 20 GeV/c spectrometer. The magnet arrangement is shown at the bottom of the figure with the symbols B, Q, and S representing dipole, quadrupole, and sextupole magnets respectively.

Fig. 4. Calculated trajectories through the spectrometer for selected initial values of horizontal and vertical angle (θ and ϕ), horizontal position (x), and momentum deviation (δ).

Fig. 5. Detector arrangement in spectrometer hut. The missing mass hodoscope (MM) was present but not used in the experiment.

Fig. 6. Peyrou plot showing c.m. kinematics for which the 18 GeV pion data were taken.

Fig. 7. 18 GeV invariant cross section at a fixed value of x vs. transverse momentum $p_\perp$ for photoproduction of $\pi^\pm$, $K^\pm$, p, and $\bar{p}$ from hydrogen.

Fig. 8. 18 GeV invariant cross section vs longitudinal mass μ for production of pions and kaons from hydrogen at fixed values of x. Squares and circles have been used for alternate values of x for clarity. The solid lines represent an exponential fitted to the $\pi^+(K^+)$ data at x=0.2, $\mu \geqslant 0.5$ GeV/c. The fitted exponential at x=0.2 has been repeated for the other values of x for purposes of comparison. The pion result is also shown as the dashed curve on the kaon figure.

Fig. 9. 18 GeV invariant cross sections vs. longitudinal mass μ for p and $\bar{p}$ production off hydrogen for fixed values of x. The solid lines represent an exponential fitted to the x=0.15 GeV/c data. The dashed curves show the comparable result for detected π^+.

Fig. 10. 18 GeV invariant cross sections vs x for pion and kaon production off hydrogen for fixed values of transverse momentum $p_\perp$. The curves represent the empirical fits used in interpolating the data and in obtaining some of the corrections used in the analysis.

Fig. 11. 18 GeV invariant cross sections vs x for production of p and $\bar{p}$ from hydrogen for fixed values of transverse momentum $p_\perp$. See Fig. 10 for additional comments.

Fig. 12. Deuterium to hydrogen ratios for pion and kaon photoproduction at 18 GeV as a function of x and transverse momentum $p_\perp$.

Fig. 13. Deuterium to hydrogen ratios for p and $\bar{p}$ photoproduction at 18 GeV as a function of x and transverse momentum $p_\perp$.

Fig. 14. Particle to antiparticle ratios for pion and kaon photoproduction at 18 GeV from protons and neutrons as a function of x and transverse momentum $p_\perp$.

Fig. 15. p to p ratio at 18 GeV from protons and neutrons as a function of x and transverse momentum $p_\perp$.

Fig. 16. Mueller-Regge exchange diagram for $a + b \longrightarrow c + X$ in the beam fragmentation region.

Fig. 17. Separated exchange amplitudes A_i vs. "projectile frame" rapidity y_p for pion photoproduction at $p_\perp = 1.$ GeV/c. The amplitudes were formed by straight sums and differences of invariant cross sections as described in the text and Table XII. The sums have not been divided by 4 or otherwise renormalized.

Fig. 18. Separated ρ and ω exchange amplitudes vs. "projectile frame" rapidity for $\gamma N \longrightarrow \pi X$ and $\gamma N \longrightarrow K X$ at fixed transverse momenta.

Fig. 19. Deuterium to hydrogen ratios vs. transverse momentum for unsubtracted (see text) $K^{\pm}$, p, and $\bar{p}$ yields. The dashed lines show the average values obtained for K^- and $\bar{p}$ production.

Fig. 20. Invariant cross sections vs "projectile frame" rapidity y_p for pion photoproduction off hydrogen at fixed values of transverse momentum $p_\perp$. The 9, 13, and 18 GeV data are from this experiment. Additional data are from refs 5 (9.3 GeV), 12 (6 GeV), and 13 (9.85 GeV). The solid (dashed) curves are a calculation of the contribution from the quasi-two-body reaction $\gamma p \longrightarrow \rho p$ at 18 (6) GeV.

Fig. 21. Invariant cross sections vs "projectile frame" rapidity y_p for kaon photoproduction off hydrogen. The 9, 13 and 18 GeV data are from this experiment, while the 6 GeV data are from ref. 12. The solid (dashed) curves are a calculation of the contribution from the quasi-two-body reaction $\gamma p \longrightarrow \phi p$ at 18 (6) GeV.

Fig. 22. Invariant cross sections for p and $\bar{p}$ photoproduction vs laboratory (for p) or projectile (for $\bar{p}$) rapidity at fixed transverse momenta. The 6 GeV data are from ref. 12. The arrows indicate the values y_p=0. at 6 and 18 GeV.

Fig. 23. $\pi^+ - \pi^-$ and $K^+ - K^-$ invariant cross section differences, multiplied by $s^{\frac{1}{2}}$ to compensate for the expected energy dependence, plotted against "projectile frame" rapidity y_p at fixed transverse momenta. The 6 GeV data are from ref. 12. The curves give the behavior expected from pp data in the central region using the Mueller-Regge model and factorization, neglecting meson-meson exchange (see text).

Fig. 24. Mueller-Regge exchange diagram for $a + b \longrightarrow c + X$ in the central region.

Fig. 25. Quark exchange diagram illustrating the expected suppression of meson-meson terms in the simple Mueller-Regge model for $\gamma p \longrightarrow K^+ X$. In this figure the photon has been shown as a ρ (or ω) meson. To the extent that the photon also acts as a ϕ meson ($\lambda\bar{\lambda}$ pair), the argument fails.

Fig. 26. Summary of fits to the constituent interchange model of ref. 47. The blocked areas show the values of N and P, as defined in the text, allowed by the model. The solid squares give the values most preferred by the data, while the hatched areas show the range of values consistent with the data.

Fig. 27. Comparison of the measured invariant cross section vs transverse momentum $p_\perp$ for $\gamma p \longrightarrow \pi^- X$ at $x \simeq 0.2$ with the best fit values obtained from the constituent interchange model of ref. 46.

Fig. 28. Invariant cross sections for $\pi^\pm$, $K^\pm$, and $\bar{p}$ photoproduction at $x \simeq 0.2$ and $p_\perp = 1.0$ GeV/c, plotted against E^*/E^*_{max}, where E^* is the c.m. energy of the observed particle and E^*_{max} is its maximum value. The curves show the behavior of ϵ^P for different values of P, where $\epsilon = 1. - E^*/E^*_{max}$. The 6 GeV data are from ref. 12.

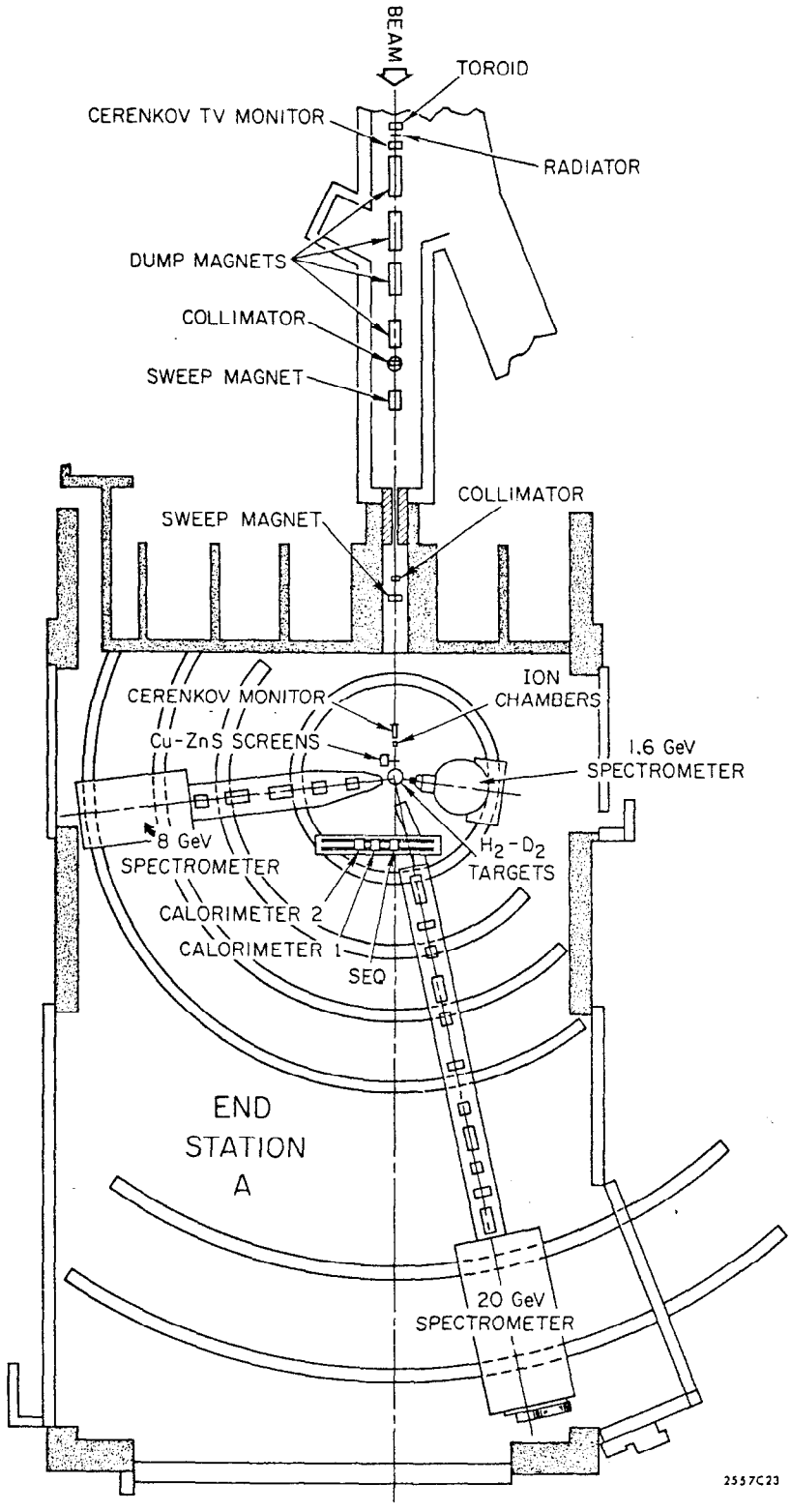
BEAM
TOROID
CERENKOV TV MONITOR
RADIATOR
DUMP MAGNETS
COLLIMATOR
SWEEP MAGNET
COLLIMATOR
SWEEP MAGNET
ION
CHAMBERS
CERENKOV MONITOR
Cu-ZnS SCREENS
1.6 GeV
SPECTROMETER
8 GeV
SPECTROMETER
H_2-D_2
TARGETS
CALORIMETER 2
CALORIMETER 1
SEQ
END
STATION
A
20 GeV
SPECTROMETER
2557C23

Fig. 1

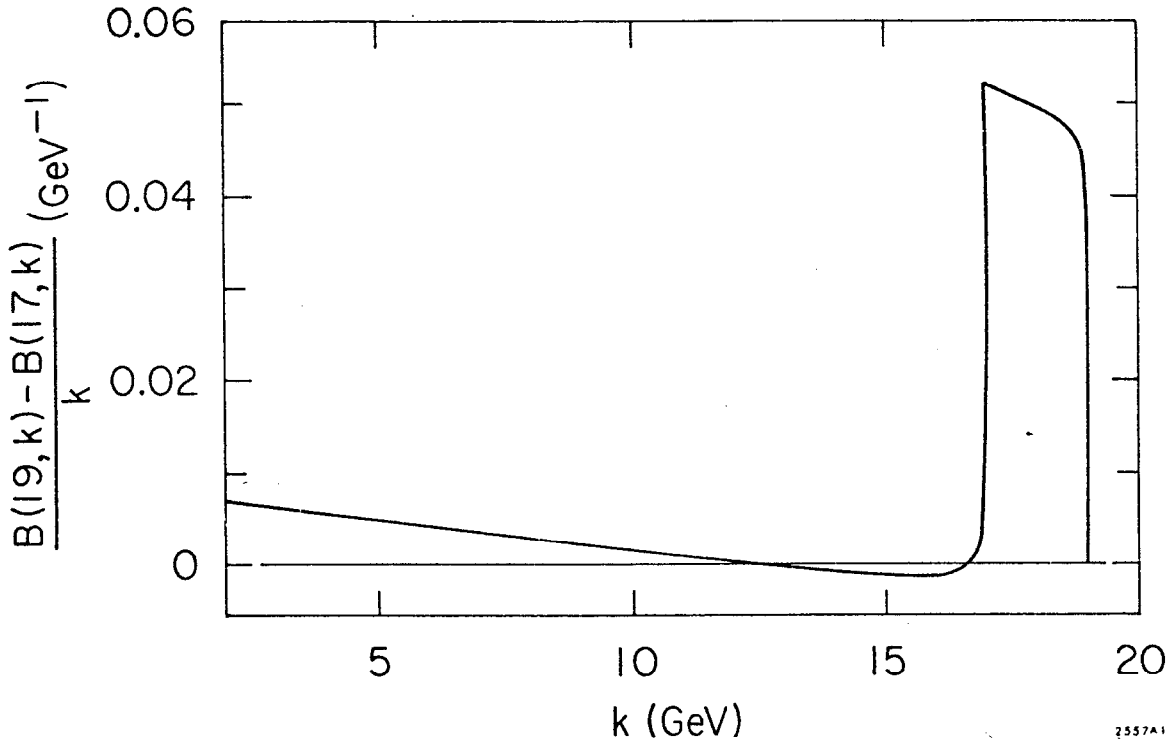
0.06
0.04
0.02
0
$\frac{B(19,k)-B(17,k)}{k}$ (GeV^{-1})
5
10
15
20
k (GeV)
2557A1

Fig. 2

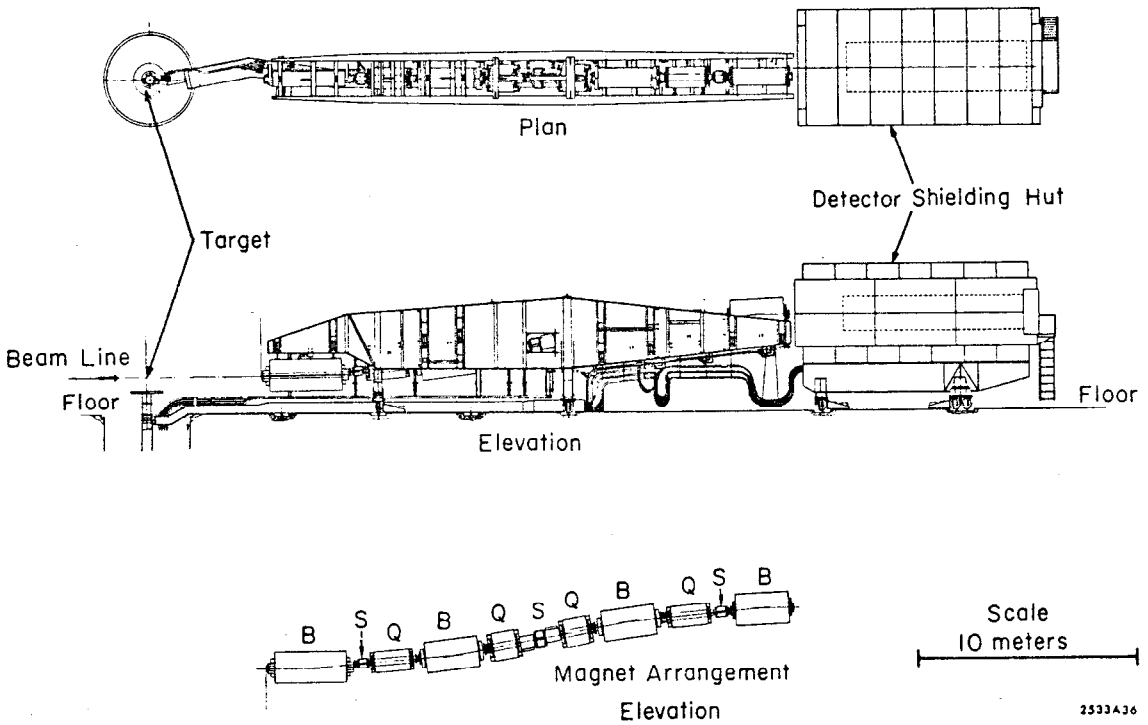
Plan
Detector Shielding Hut
Target
Beam Line
Floor
Floor
Elevation
B
S
Q
B
Q
S
Q
B
Q
S
B
Magnet Arrangement
Elevation
Scale
10 meters
2533A36

Fig. 3

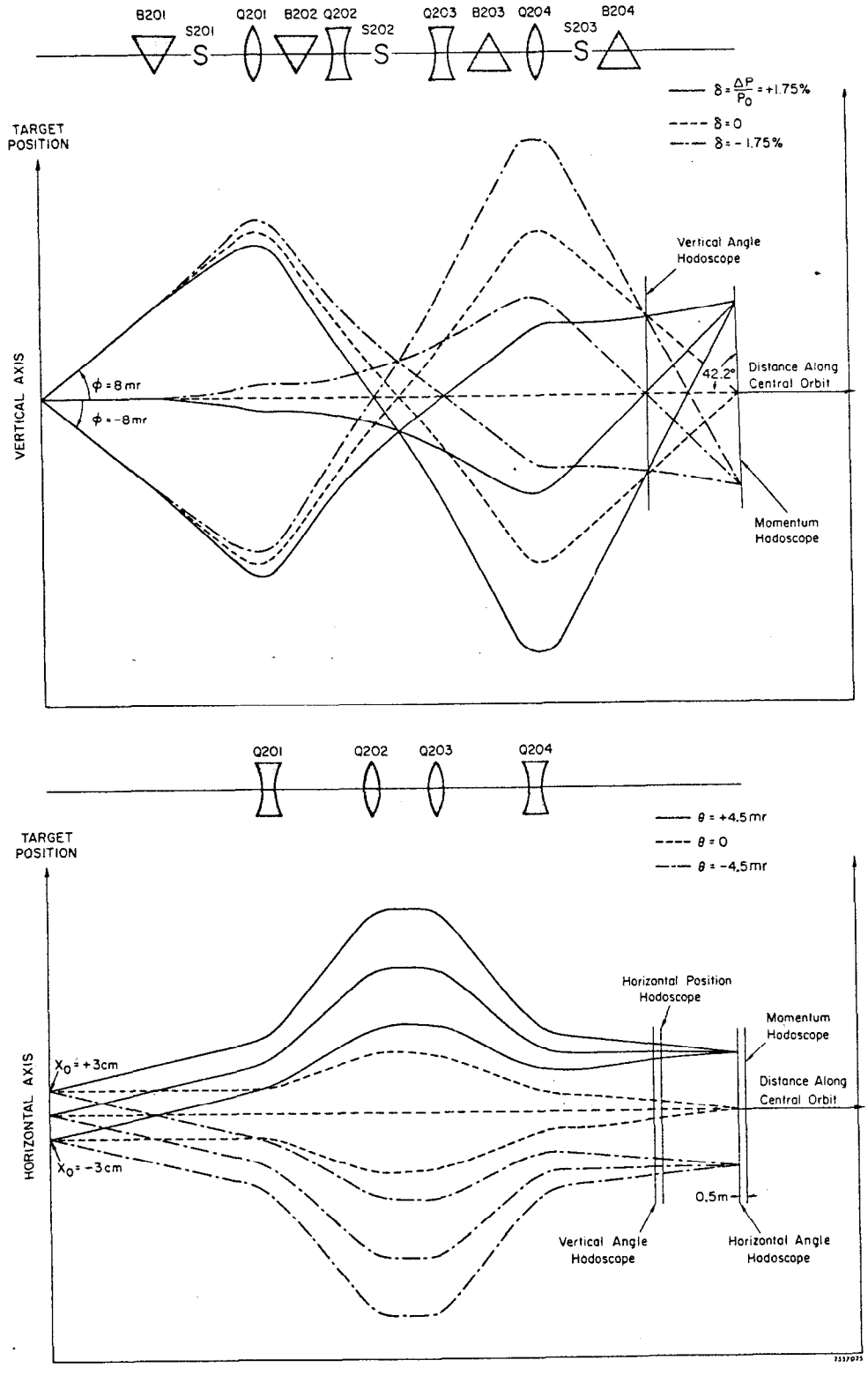
B201
S201
Q201
B202
Q202
S202
Q203
B203
Q204
S203
B204
δ = ΔP/P0 = +1.75%
δ = 0
δ = - 1.75%
TARGET POSITION
VERTICAL AXIS
Vertical Angle Hodoscope
φ = 8 mr
φ = -8 mr
42.2°
Distance Along Central Orbit
Momentum Hodoscope
Q201
Q202
Q203
Q204
θ = +4.5 mr
θ = 0
θ = -4.5 mr
TARGET POSITION
HORIZONTAL AXIS
Horizontal Position Hodoscope
Momentum Hodoscope
X0 = +3cm
Distance Along Central Orbit
X0 = -3cm
0.5m
Vertical Angle Hodoscope
Horizontal Angle Hodoscope

Fig. 4

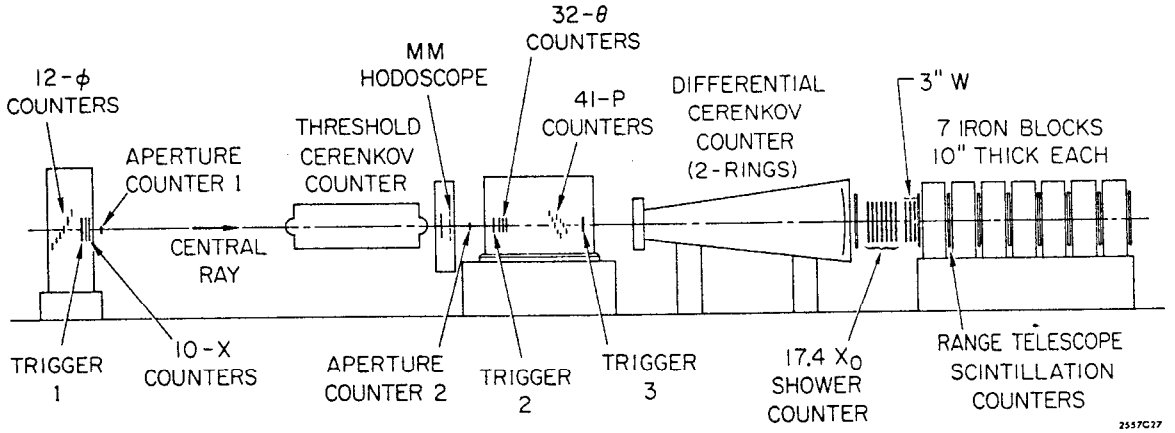
12-φ COUNTERS
APERTURE COUNTER 1
CENTRAL RAY
THRESHOLD CERENKOV COUNTER
MM HODOSCOPE
32-θ COUNTERS
41-P COUNTERS
DIFFERENTIAL CERENKOV COUNTER (2-RINGS)
3" W
7 IRON BLOCKS 10" THICK EACH
TRIGGER 1
10-X COUNTERS
APERTURE COUNTER 2
TRIGGER 2
TRIGGER 3
17.4 X0 SHOWER COUNTER
RANGE TELESCOPE SCINTILLATION COUNTERS
2557C27

Fig. 5

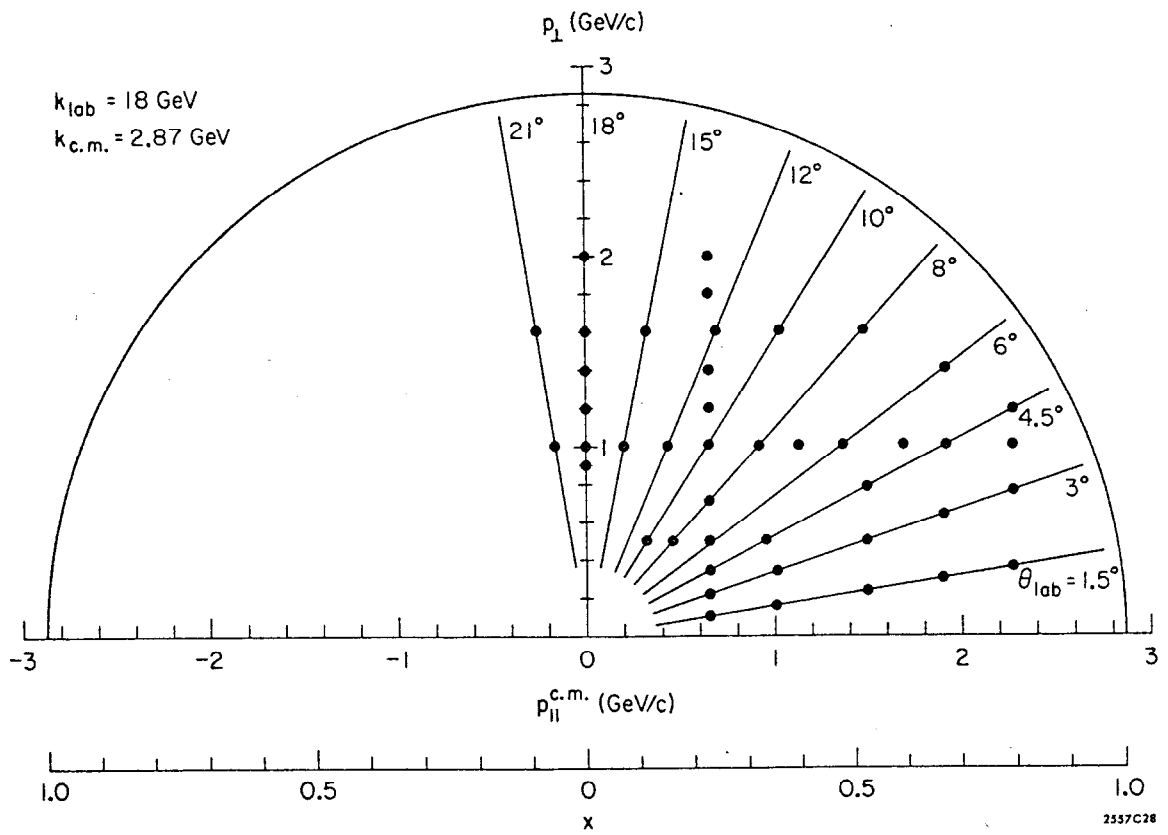
p⊥ (GeV/c)
klab = 18 GeV
kc.m. = 2.87 GeV
21°
18°
15°
12°
10°
8°
6°
4.5°
3°
θlab = 1.5°
3
2
1
-3
-2
-1
0
1
2
3
p∥c.m. (GeV/c)
1.0
0.5
0
0.5
1.0
x
2557C28

Fig. 6

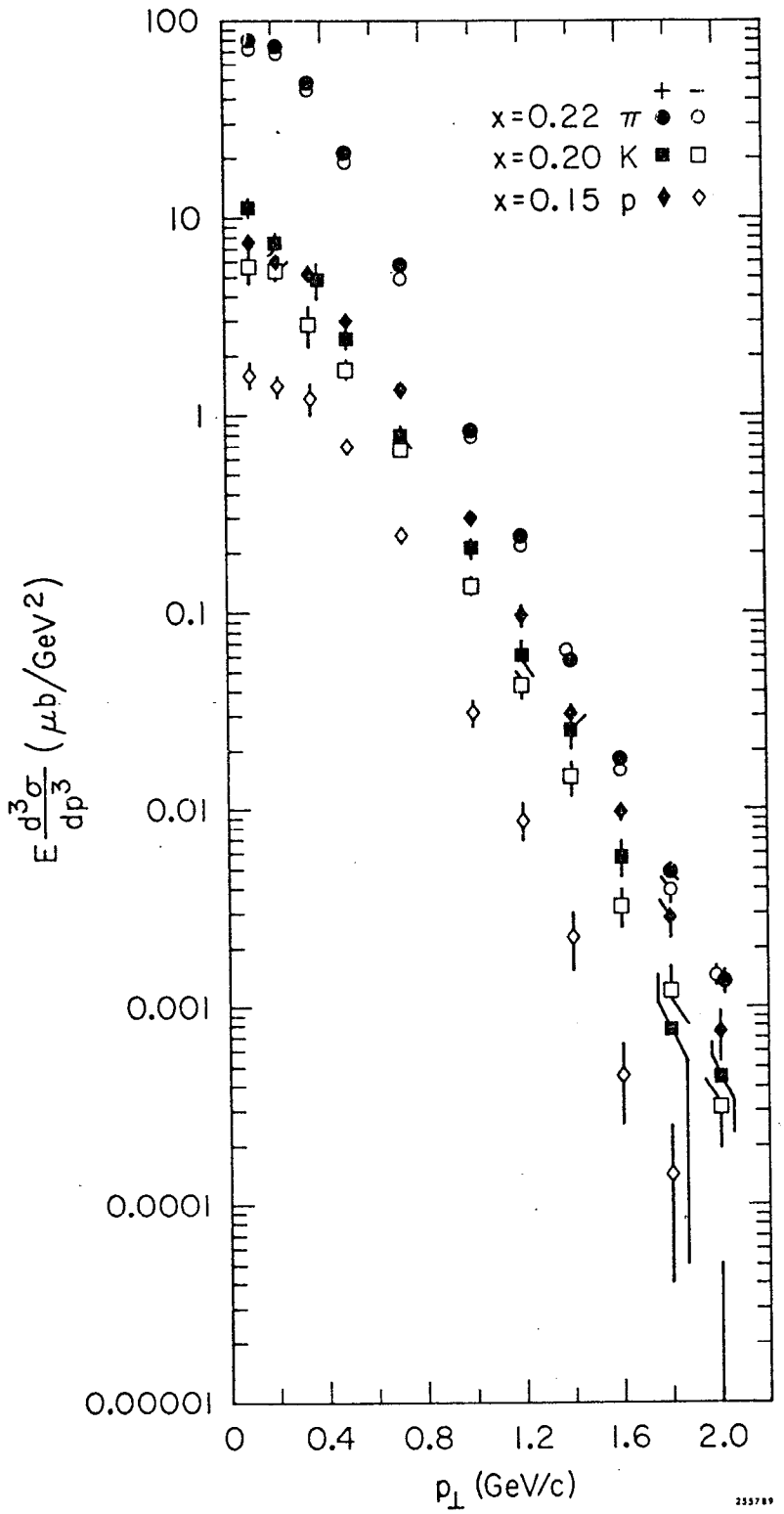
100
10
1
0.1
0.01
0.001
0.0001
0.00001
0
0.4
0.8
1.2
1.6
2.0
$p_\perp$ (GeV/c)
$E\frac{d^3\sigma}{dp^3}$ (μb/GeV^2)
x=0.22 π
x=0.20 K
x=0.15 p
+
−

Fig. 7

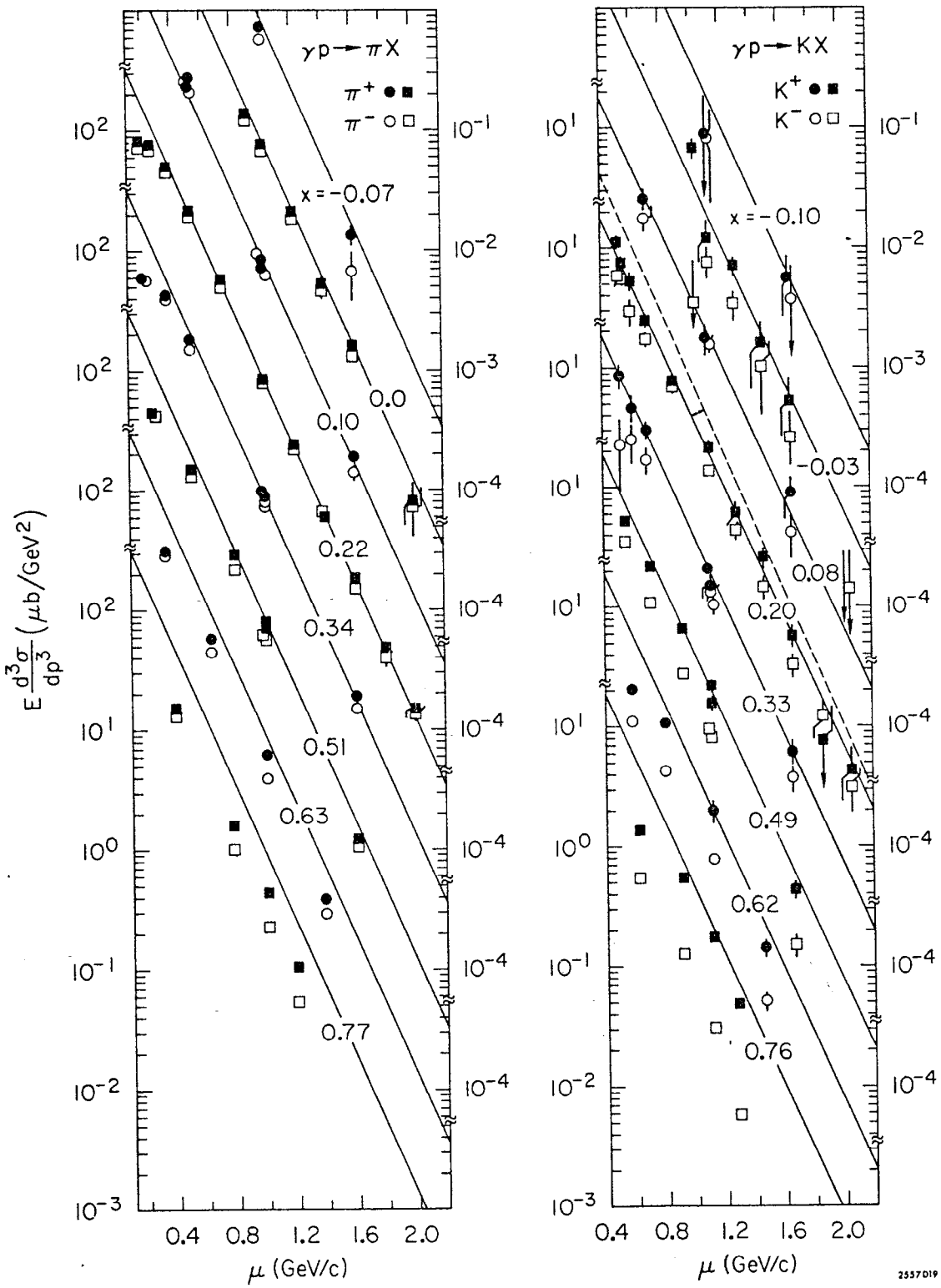
γp → πX
π+ ● ■
π− ○ □
x = −0.07
0.0
0.10
0.22
0.34
0.51
0.63
0.77
γp → KX
K+ ● ■
K− ○ □
x = −0.10
−0.03
0.08
0.20
0.33
0.49
0.62
0.76
E d³σ/dp³ (μb/GeV²)
μ (GeV/c)
2537D19

Fig. 8

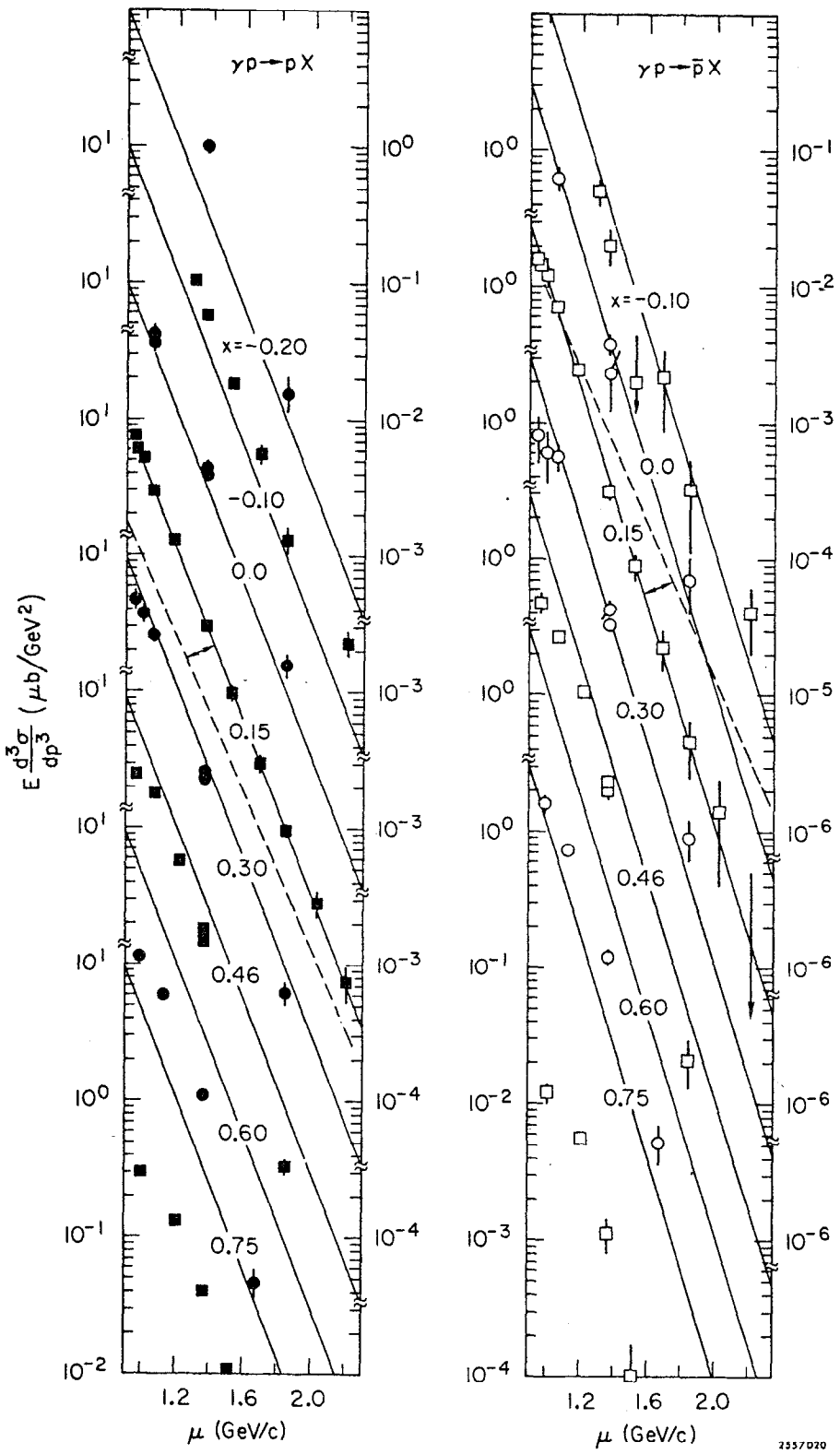
γp→pX
γp→p̄X
x=-0.20
-0.10
0.0
0.15
0.30
0.46
0.60
0.75
x=-0.10
0.0
0.15
0.30
0.46
0.60
0.75
E d³σ/dp³ (μb/GeV²)
μ (GeV/c)
1.2
1.6
2.0
2557D20

Fig. 9

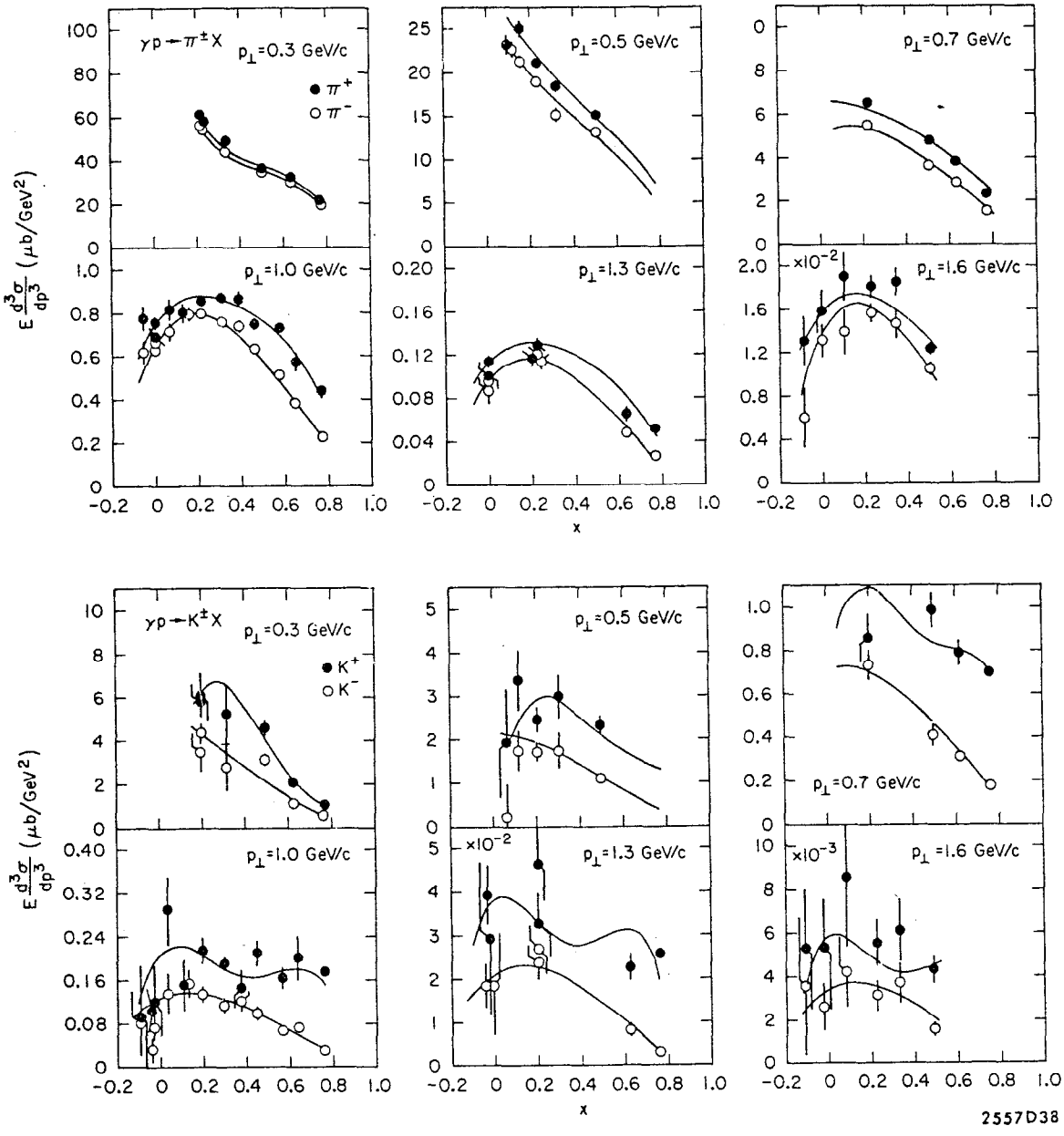
γp→π±X
p⊥=0.3 GeV/c
● π+
○ π−
p⊥=0.5 GeV/c
p⊥=0.7 GeV/c
p⊥=1.0 GeV/c
p⊥=1.3 GeV/c
×10−2
p⊥=1.6 GeV/c
E d3σ/dp3 (μb/GeV2)
x
γp→K±X
● K+
○ K−
×10−3
2557D38

Fig. 10

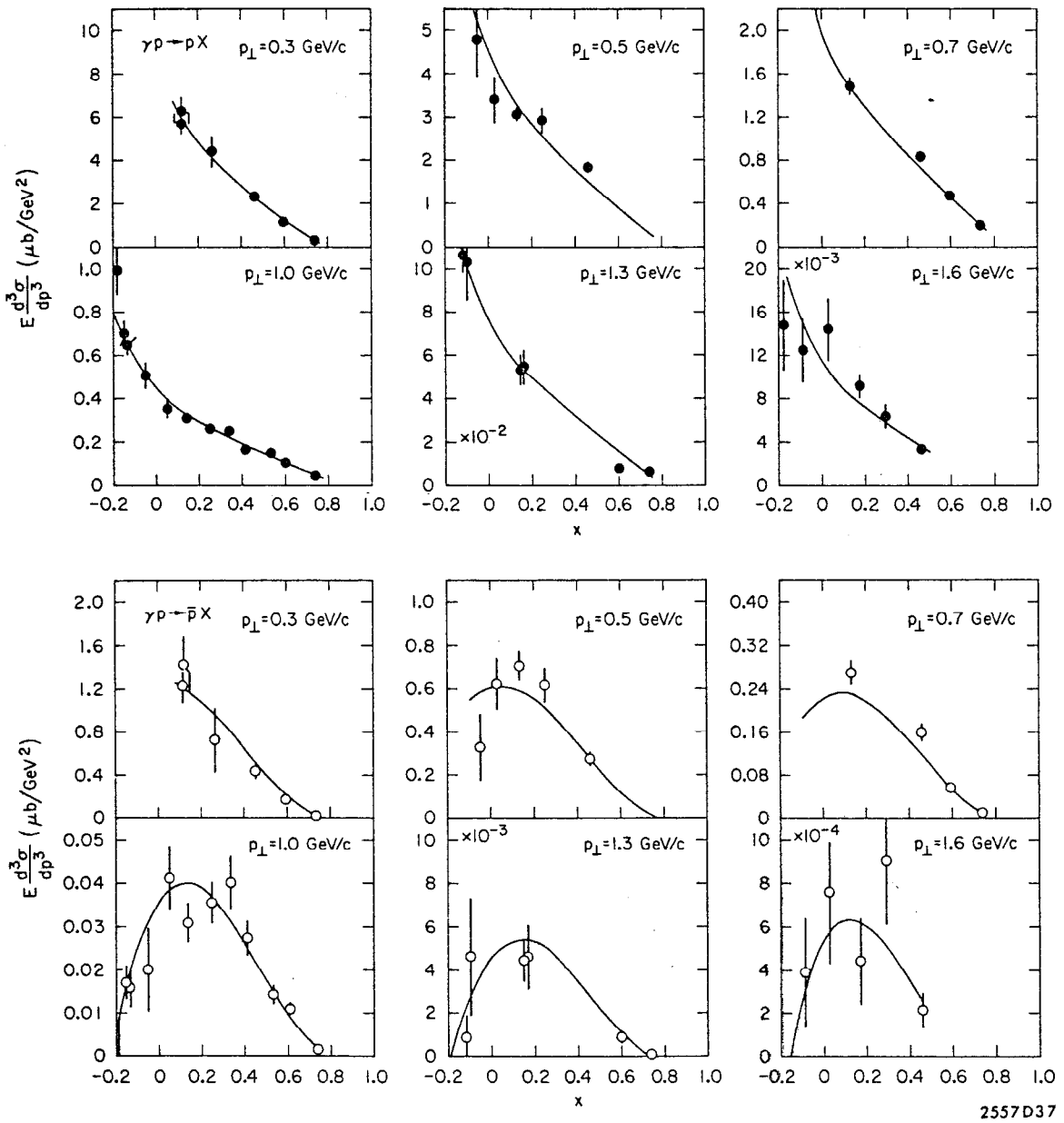
γp→pX
p⊥=0.3 GeV/c
p⊥=0.5 GeV/c
p⊥=0.7 GeV/c
p⊥=1.0 GeV/c
p⊥=1.3 GeV/c
p⊥=1.6 GeV/c
×10⁻²
×10⁻³
E d³σ/dp³ (μb/GeV²)
x
γp→p̄X
×10⁻⁴
2557D37

Fig. 11

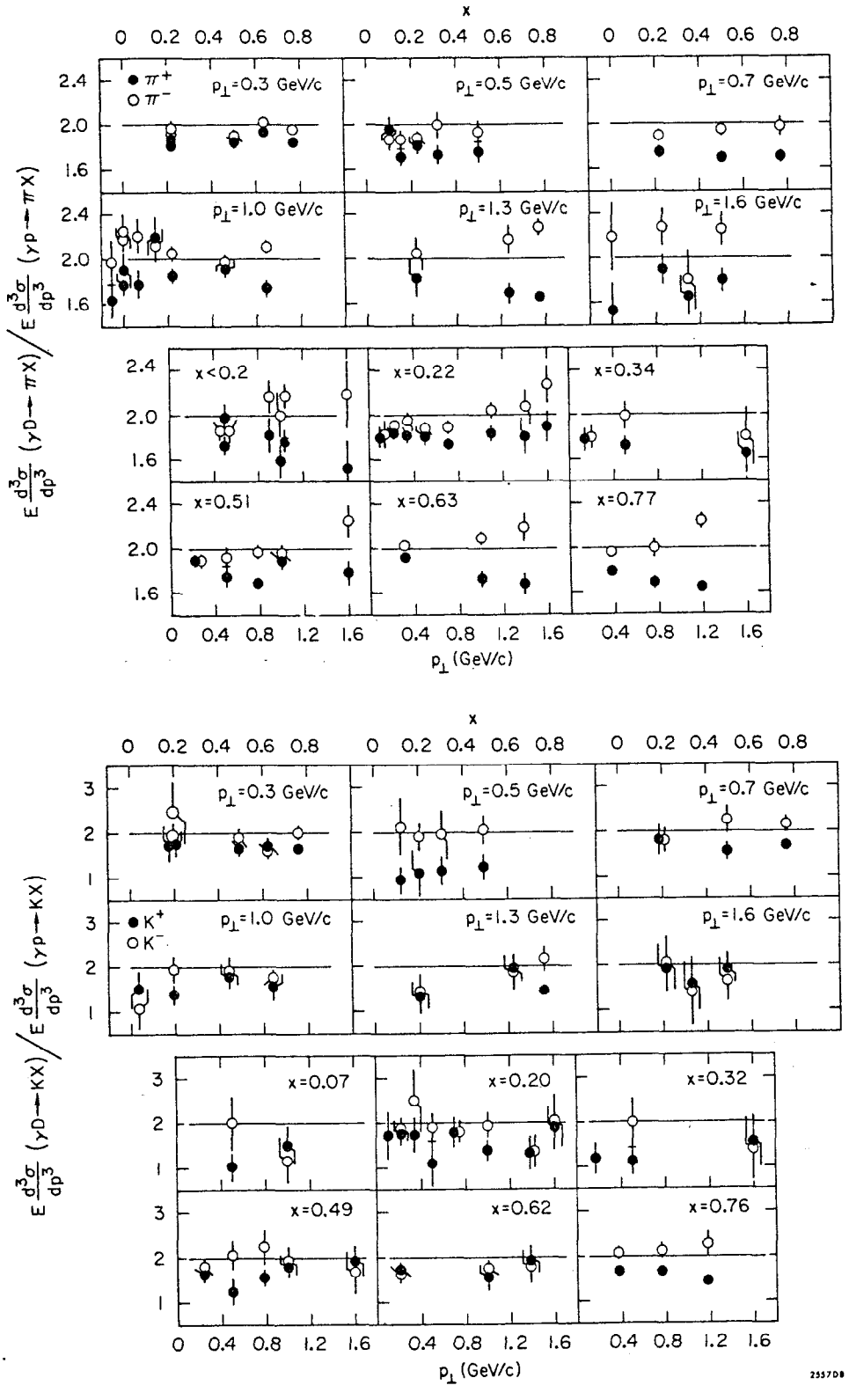
x
0 0.2 0.4 0.6 0.8
● π+
○ π−
p⊥=0.3 GeV/c
p⊥=0.5 GeV/c
p⊥=0.7 GeV/c
p⊥=1.0 GeV/c
p⊥=1.3 GeV/c
p⊥=1.6 GeV/c
x<0.2
x=0.22
x=0.34
x=0.51
x=0.63
x=0.77
E d³σ/dp³ (γD→πX) / E d³σ/dp³ (γp→πX)
p⊥ (GeV/c)
● K+
○ K−
x=0.07
x=0.20
x=0.32
x=0.49
x=0.62
x=0.76
E d³σ/dp³ (γD→KX) / E d³σ/dp³ (γp→KX)
2557D8

Fig. 12

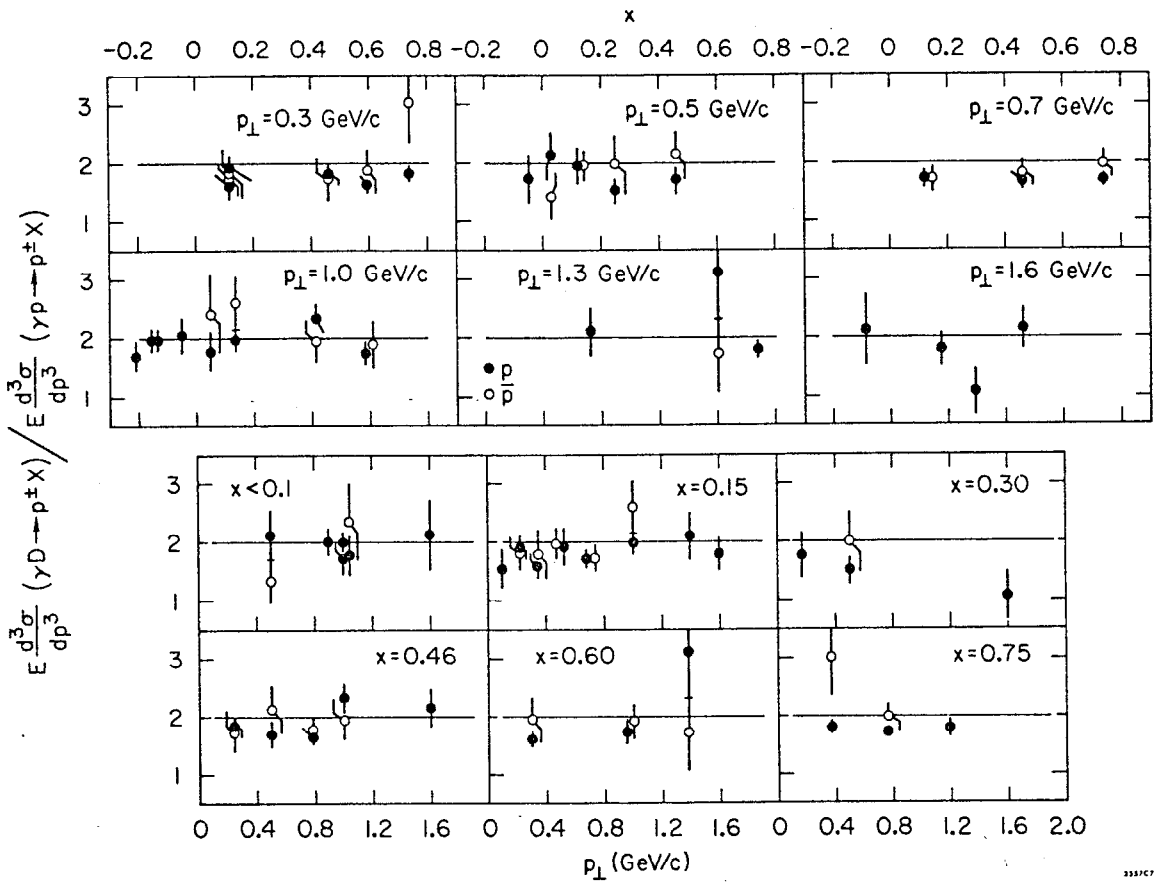
x
-0.2 0 0.2 0.4 0.6 0.8
p⊥=0.3 GeV/c
p⊥=0.5 GeV/c
p⊥=0.7 GeV/c
p⊥=1.0 GeV/c
p⊥=1.3 GeV/c
p⊥=1.6 GeV/c
● p
○ p̄
x<0.1
x=0.15
x=0.30
x=0.46
x=0.60
x=0.75
E d³σ/dp³ (γD→p±X) / E d³σ/dp³ (γp→p±X)
0 0.4 0.8 1.2 1.6 2.0
p⊥ (GeV/c)

Fig. 13

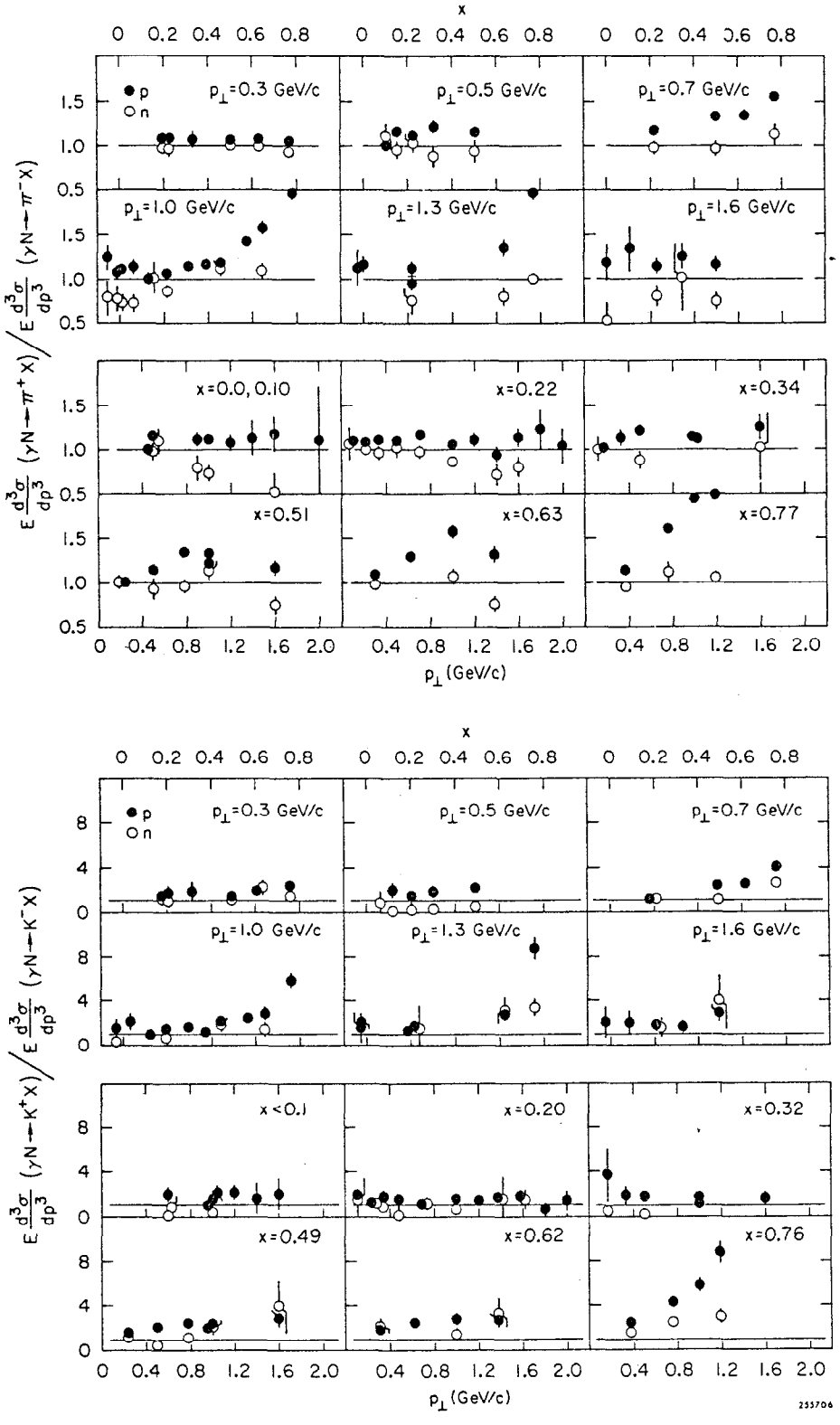
x
0 0.2 0.4 0.6 0.8
● p
○ n
$p_\perp$=0.3 GeV/c
$p_\perp$=0.5 GeV/c
$p_\perp$=0.7 GeV/c
$p_\perp$=1.0 GeV/c
$p_\perp$=1.3 GeV/c
$p_\perp$=1.6 GeV/c
$E\frac{d^3\sigma}{dp^3}(\gamma N\to\pi^-X)$
x=0.0, 0.10
x=0.22
x=0.34
x=0.51
x=0.63
x=0.77
$E\frac{d^3\sigma}{dp^3}(\gamma N\to\pi^+X)$
0.5 1.0 1.5
0 0.4 0.8 1.2 1.6 2.0
$p_\perp$ (GeV/c)
$E\frac{d^3\sigma}{dp^3}(\gamma N\to K^-X)$
x<0.1
x=0.20
x=0.32
x=0.49
x=0.62
x=0.76
$E\frac{d^3\sigma}{dp^3}(\gamma N\to K^+X)$
0 4 8
255706

Fig. 14

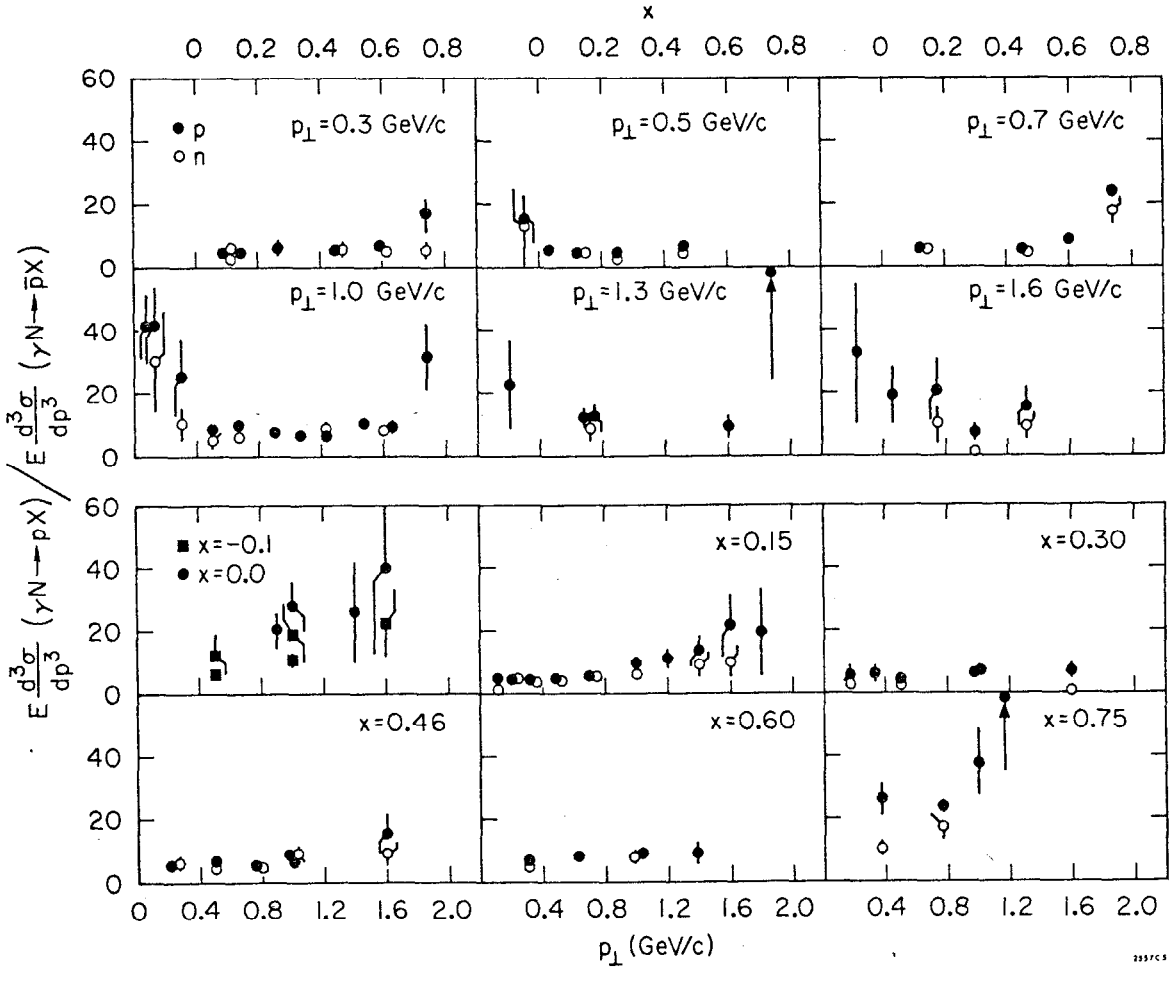
x
0 0.2 0.4 0.6 0.8
p
n
$p_\perp$=0.3 GeV/c
$p_\perp$=0.5 GeV/c
$p_\perp$=0.7 GeV/c
$p_\perp$=1.0 GeV/c
$p_\perp$=1.3 GeV/c
$p_\perp$=1.6 GeV/c
x=-0.1
x=0.0
x=0.15
x=0.30
x=0.46
x=0.60
x=0.75
$E\frac{d^3\sigma}{dp^3}(\gamma N \to \bar{p}X) / E\frac{d^3\sigma}{dp^3}(\gamma N \to pX)$
0 0.4 0.8 1.2 1.6 2.0
$p_\perp$ (GeV/c)

Fig. 15

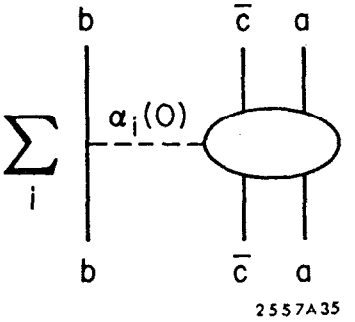
b
$\bar{c}$
a
$\sum_i$
$\alpha_i(0)$
b
$\bar{c}$
a
2557A35

Fig. 16

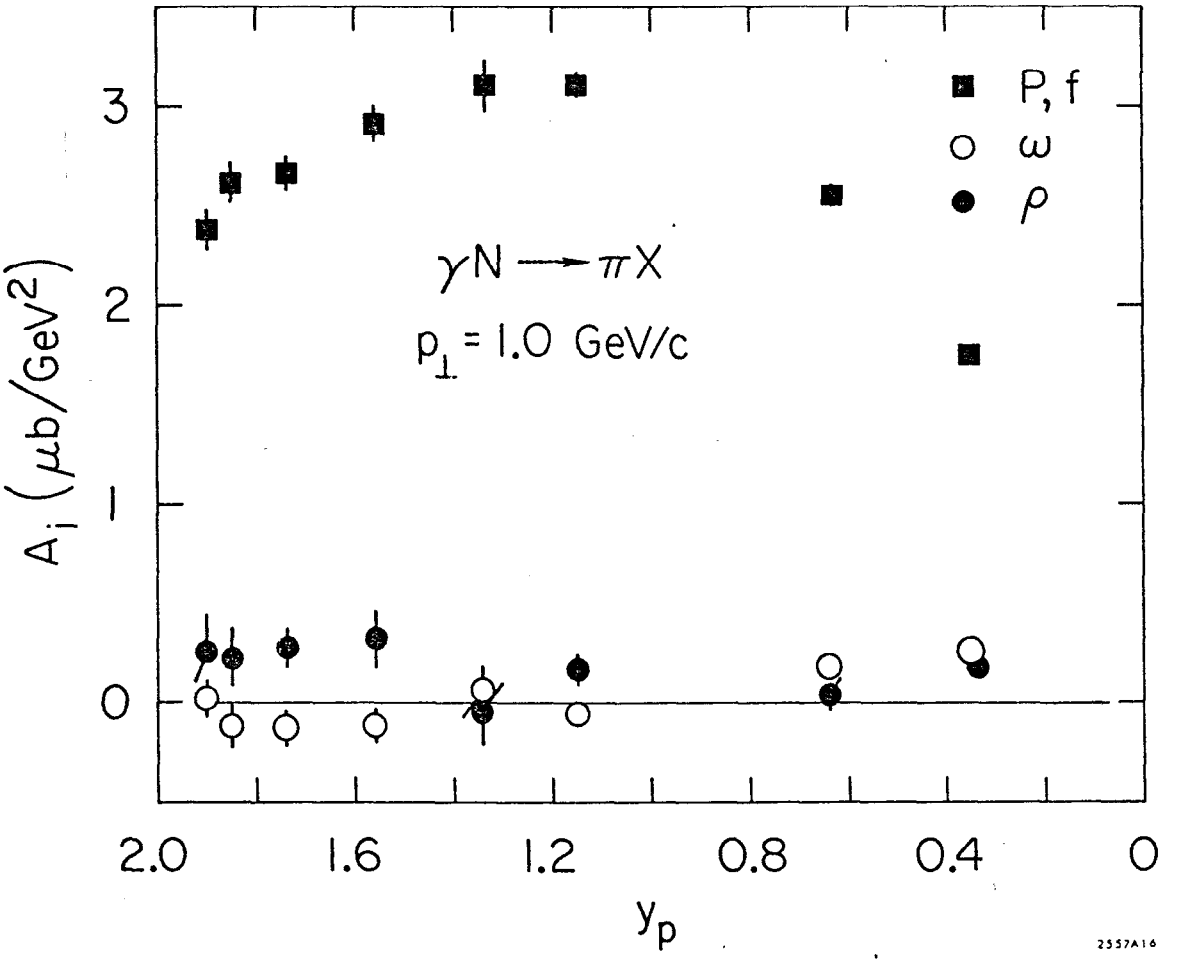
P, f
ω
ρ
$\gamma N \longrightarrow \pi X$
$p_\perp = 1.0$ GeV/c
A_i (μb/GeV^2)
3
2
1
0
2.0
1.6
1.2
0.8
0.4
0
y_p
2557A16

Fig. 17

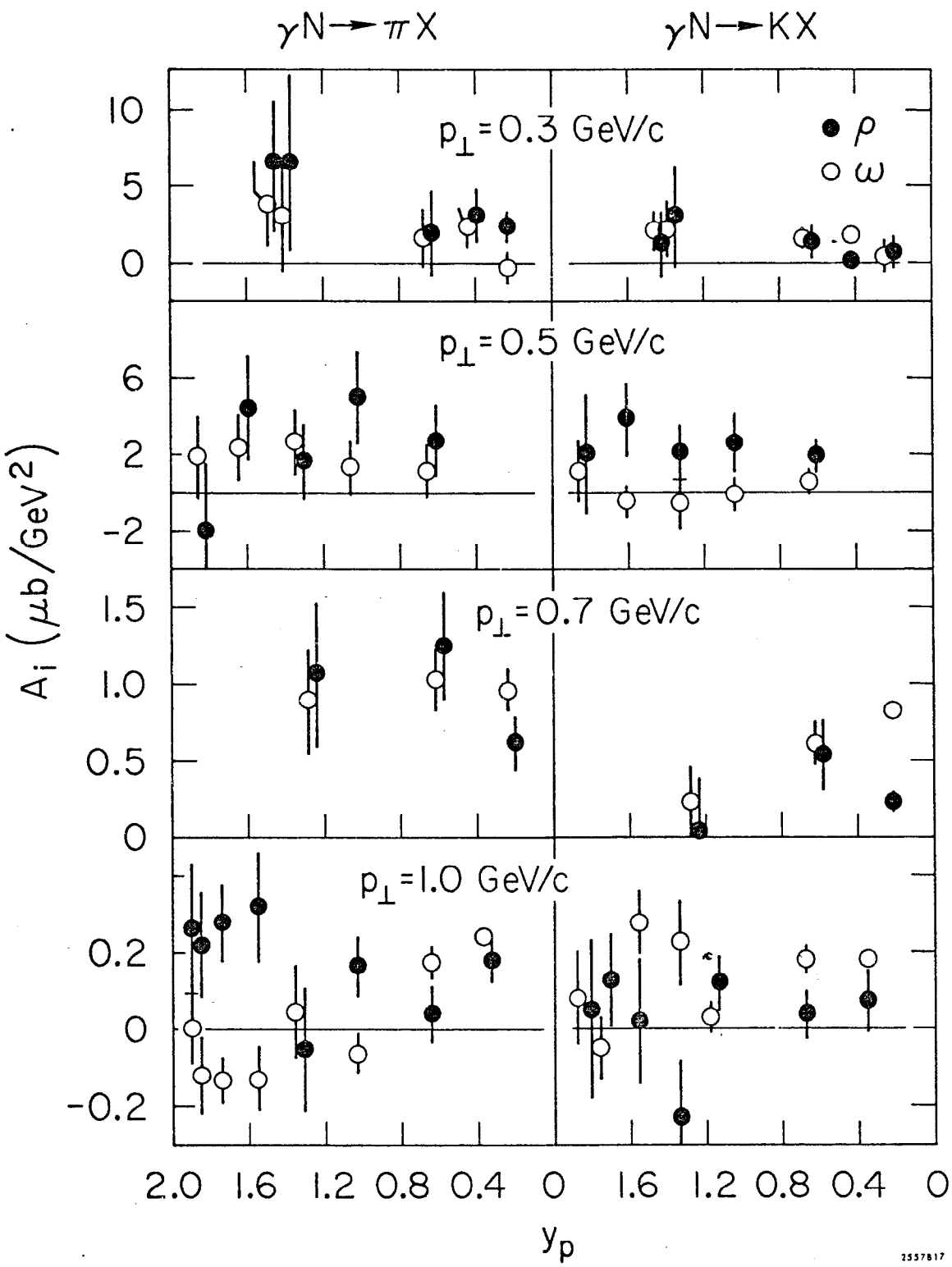
γN→πX
γN→KX
p⊥=0.3 GeV/c
ρ
ω
p⊥=0.5 GeV/c
p⊥=0.7 GeV/c
p⊥=1.0 GeV/c
Ai (μb/GeV²)
yp
2557817

Fig. 18

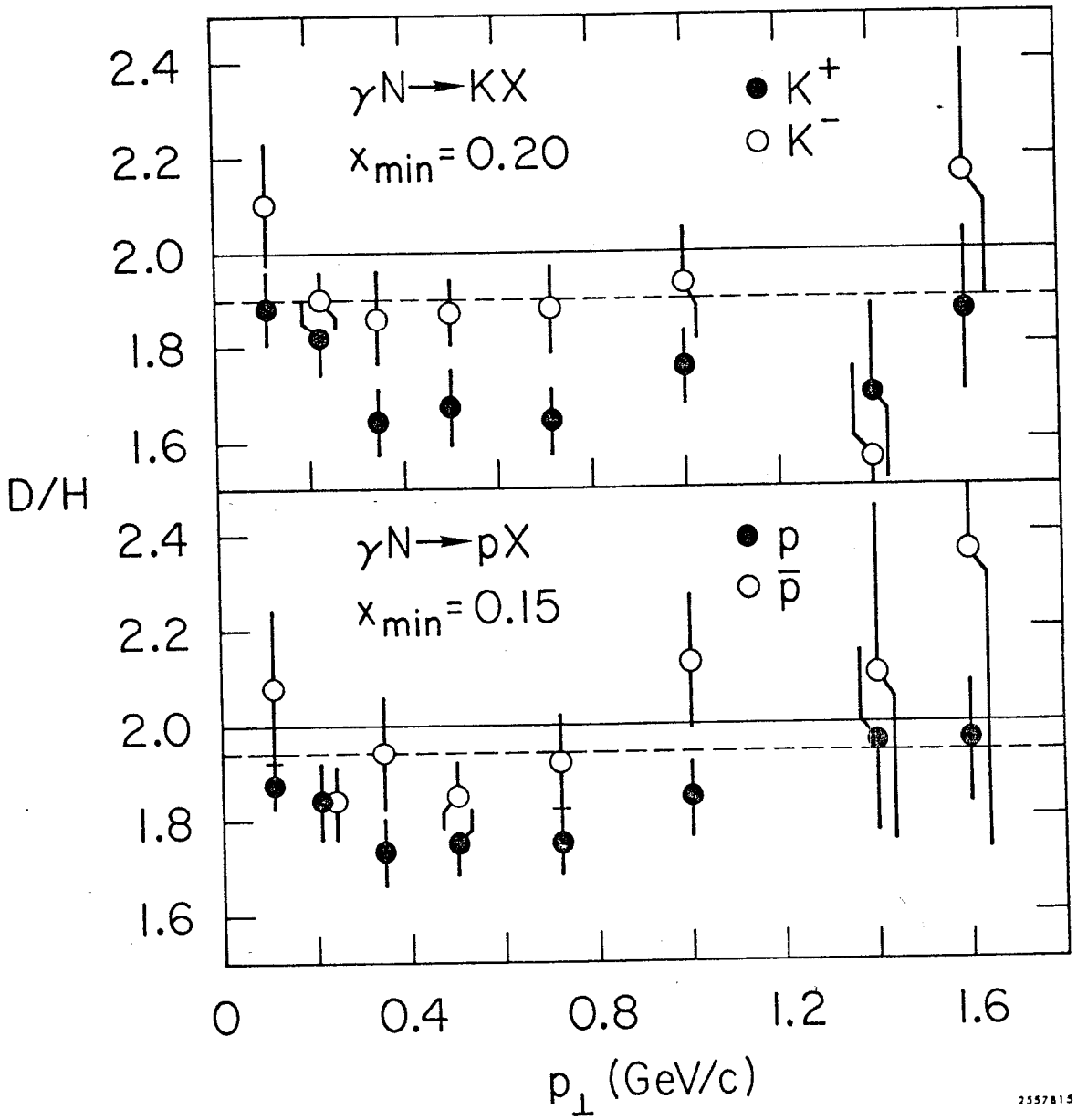
γN→KX
x_min = 0.20
K+
K−
γN→pX
x_min = 0.15
p
p̄
D/H
2.4
2.2
2.0
1.8
1.6
0
0.4
0.8
1.2
1.6
p⊥ (GeV/c)
2557815

Fig. 19

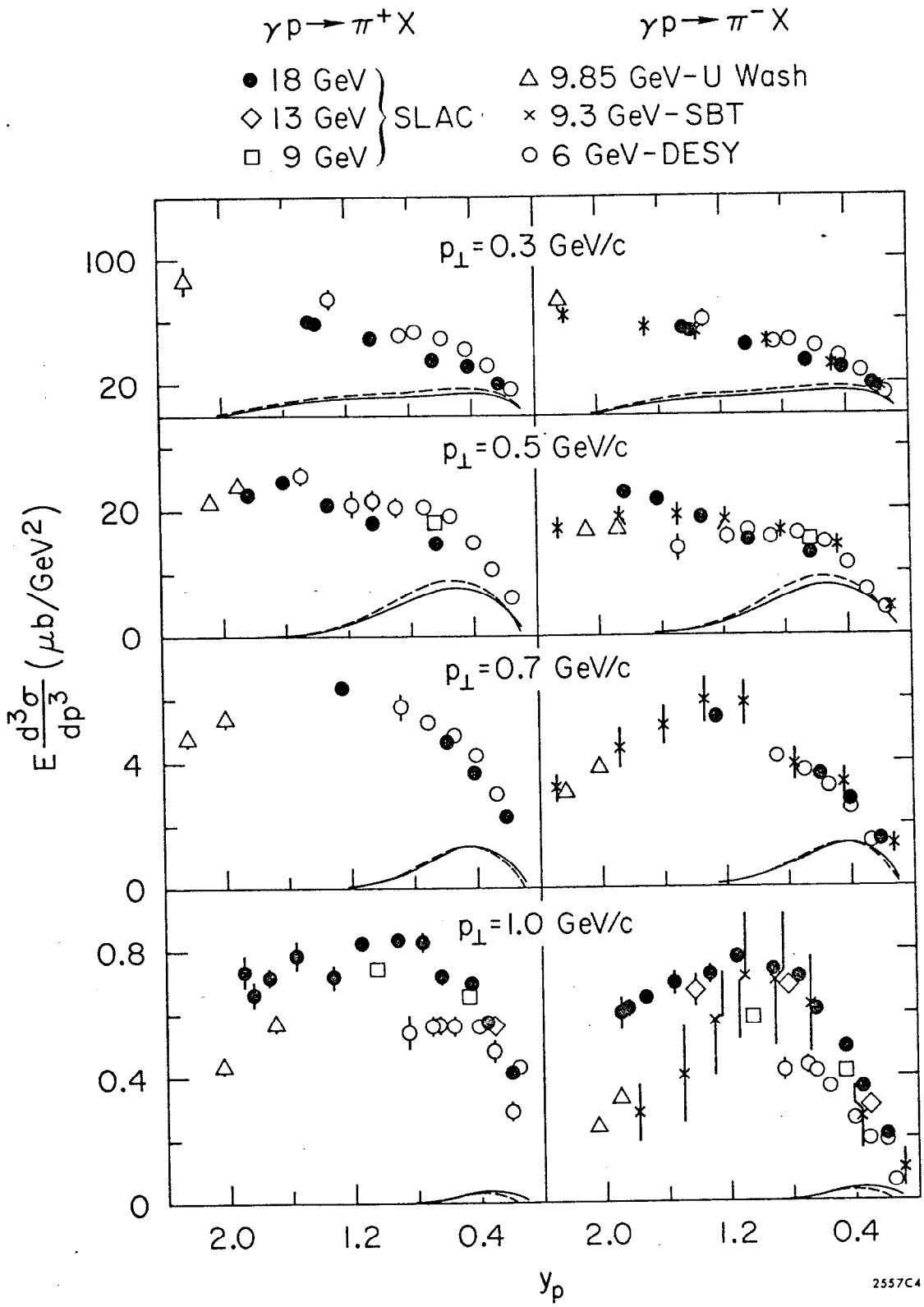
γp → π⁺X
γp → π⁻X
● 18 GeV
◇ 13 GeV
□ 9 GeV
SLAC
△ 9.85 GeV-U Wash
× 9.3 GeV-SBT
○ 6 GeV-DESY
p⊥=0.3 GeV/c
p⊥=0.5 GeV/c
p⊥=0.7 GeV/c
p⊥=1.0 GeV/c
E d³σ/dp³ (μb/GeV²)
100
20
20
0
4
0
0.8
0.4
0
2.0
1.2
0.4
2.0
1.2
0.4
y_p
2557C4

Fig. 20

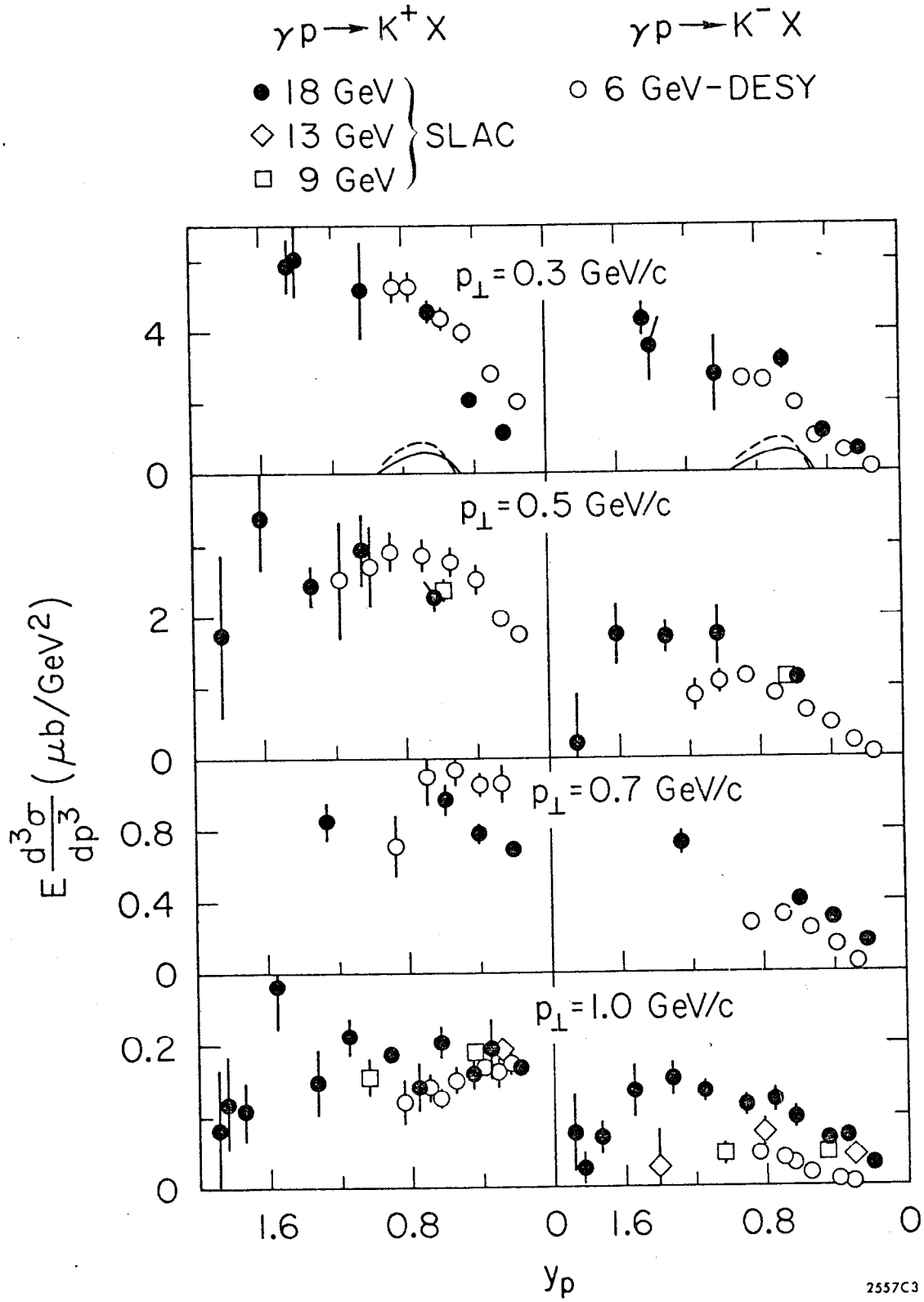
γp → K⁺X
γp → K⁻X
● 18 GeV
◇ 13 GeV
□ 9 GeV
SLAC
○ 6 GeV-DESY
p⊥ = 0.3 GeV/c
p⊥ = 0.5 GeV/c
p⊥ = 0.7 GeV/c
p⊥ = 1.0 GeV/c
E d³σ/dp³ (μb/GeV²)
4
0
2
0
0.8
0.4
0
0.2
0
1.6
0.8
0
1.6
0.8
0
yp
2557C3

Fig. 21

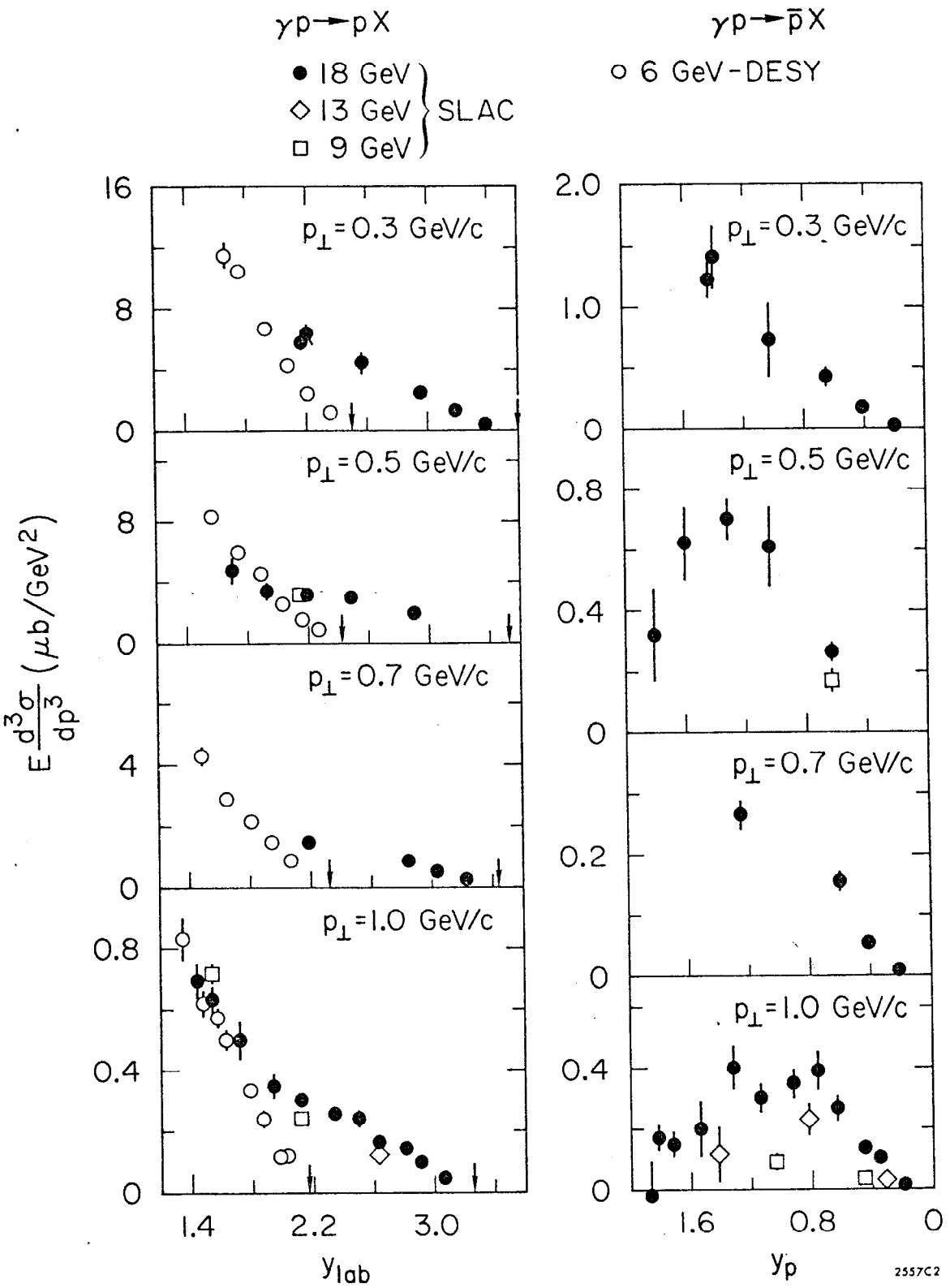
γp→pX
γp→p̄X
● 18 GeV
◇ 13 GeV
□ 9 GeV
SLAC
○ 6 GeV-DESY
p⊥=0.3 GeV/c
p⊥=0.5 GeV/c
p⊥=0.7 GeV/c
p⊥=1.0 GeV/c
E d³σ/dp³ (μb/GeV²)
y_lab
y_p
2557C2

Fig. 22

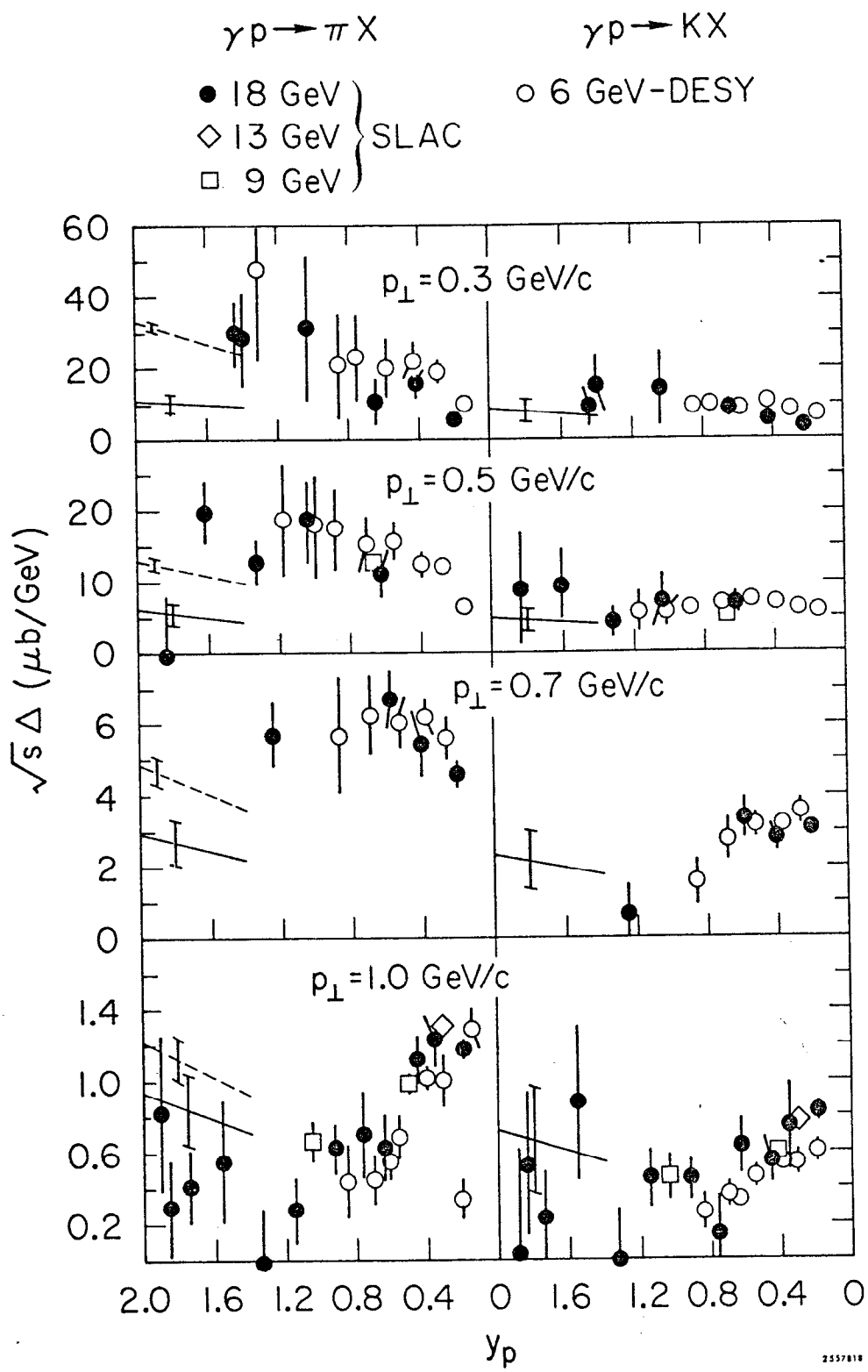
γp → πX
γp → KX
● 18 GeV
◇ 13 GeV
□ 9 GeV
SLAC
○ 6 GeV-DESY
p⊥=0.3 GeV/c
p⊥=0.5 GeV/c
p⊥=0.7 GeV/c
p⊥=1.0 GeV/c
√s Δ (μb/GeV)
yp
2557818

Fig. 23

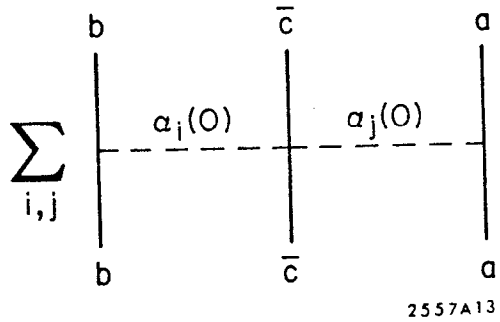
b
c̄
a
$\sum_{i,j}$
$\alpha_i(0)$
$\alpha_j(0)$
b
c̄
a
2557A13

Fig. 24

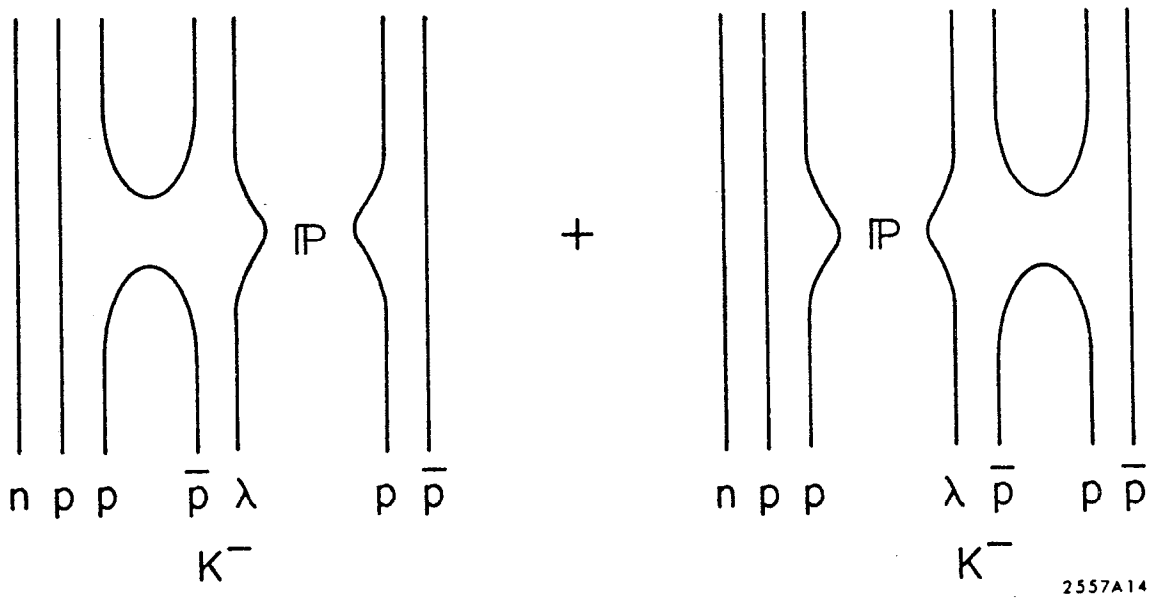
$\mathbb{P}$
+
$\mathbb{P}$
n p p p̄ λ p p̄
K⁻
n p p λ p̄ p p̄
K⁻
2557A14

Fig. 25

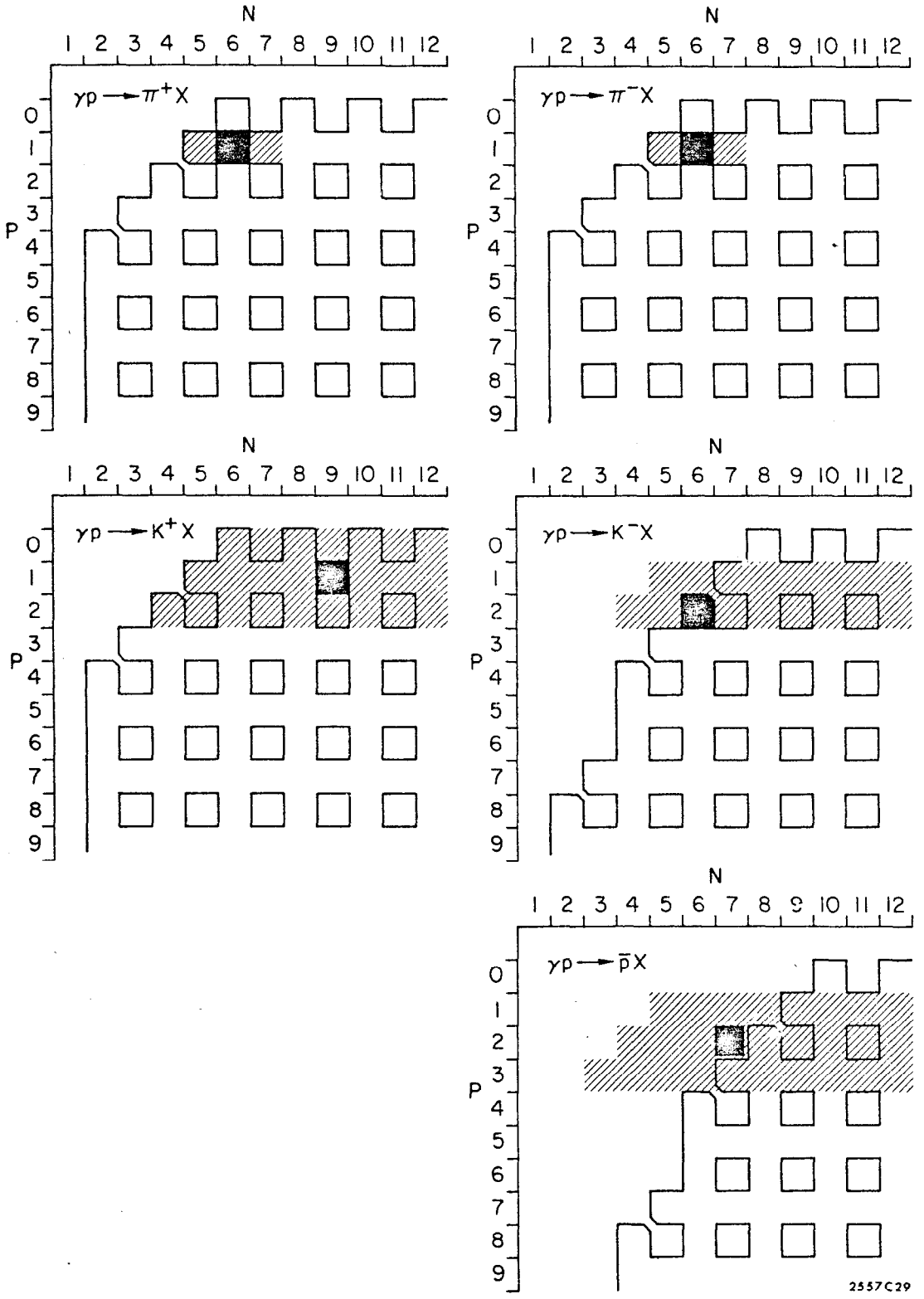
N
1 2 3 4 5 6 7 8 9 10 11 12
P
0 1 2 3 4 5 6 7 8 9
γp → π⁺X
γp → π⁻X
γp → K⁺X
γp → K⁻X
γp → p̄X
2557C29

Fig. 26

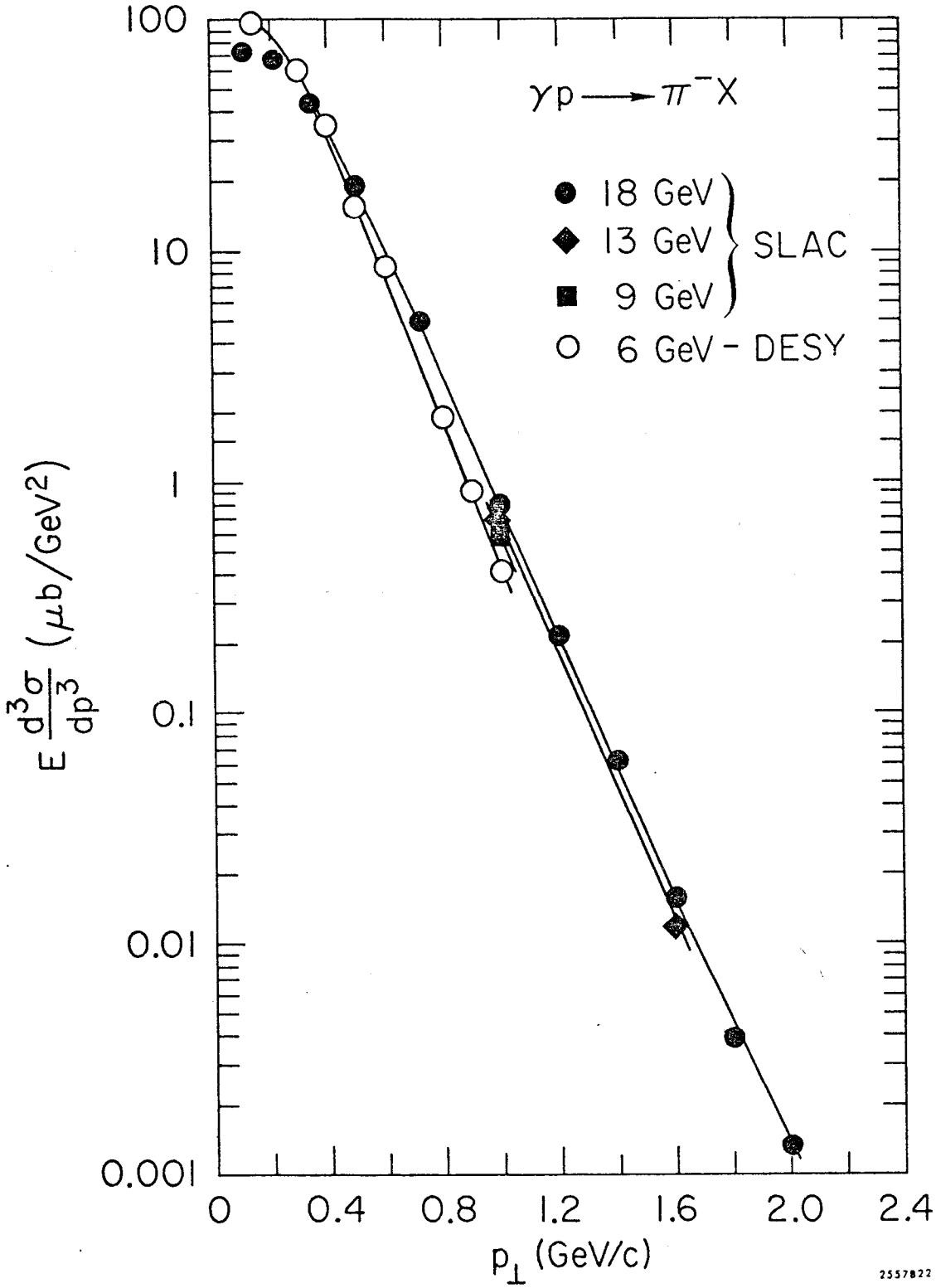
$\gamma p \longrightarrow \pi^- X$
18 GeV
13 GeV
9 GeV
SLAC
6 GeV - DESY
$E \frac{d^3\sigma}{dp^3}$ (μb/GeV^2)
100
10
1
0.1
0.01
0.001
0
0.4
0.8
1.2
1.6
2.0
2.4
$p_\perp$ (GeV/c)
2557B22

Fig. 27

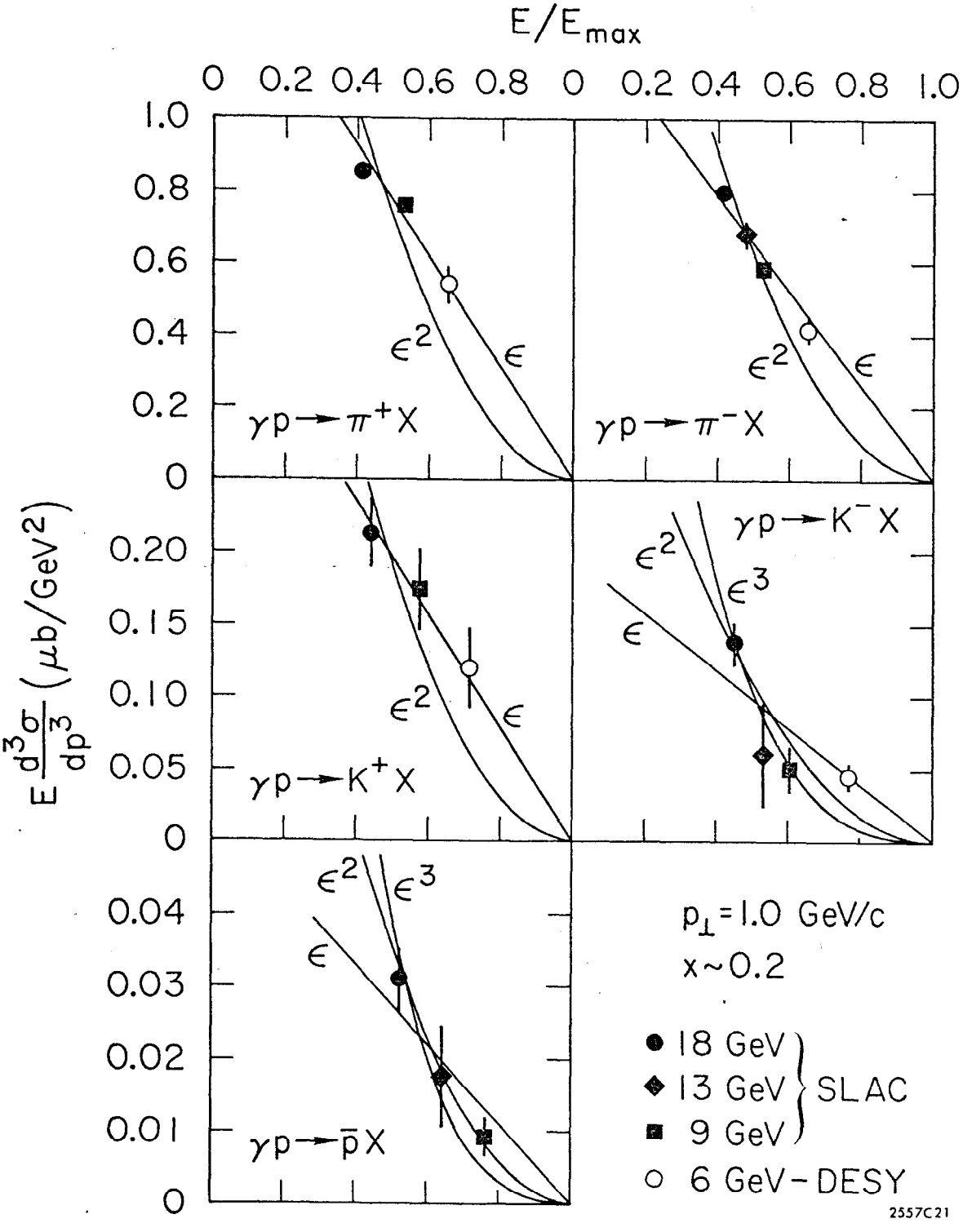
E/E_max
0 0.2 0.4 0.6 0.8 0 0.2 0.4 0.6 0.8 1.0
1.0
0.8
0.6
0.4
0.2
0
0.20
0.15
0.10
0.05
0
0.04
0.03
0.02
0.01
0
E d³σ/dp³ (μb/GeV²)
γp → π⁺X
γp → π⁻X
γp → K⁺X
γp → K⁻X
γp → p̄X
ε²
ε
ε³
p⊥ = 1.0 GeV/c
x ~ 0.2
18 GeV
13 GeV
9 GeV
SLAC
6 GeV - DESY
2557C21

Fig. 28

ADDENDUM

SLAC experiment E-66 was performed to measure inclusive charged particle photoproduction. From a physics viewpoint one is interested in cross sections for mono-energetic photons, whereas experimentally one uses a bremsstrahlung beam with a continuous energy spectrum. To obtain cross sections at the desired energy a subtraction technique was used which utilized bremsstrahlung beams with endpoints above and below the nominal energy. The purpose of this addendum is to present 18 GeV particle yields from the unsubtracted bremsstrahlung beam. These data should be of value to other experimenters doing electroproduction or photoproduction experiments.

To obtain the 18 GeV data, endpoints of either 17 and 19 GeV or 16 and 20 GeV were used. In order to present data for a single endpoint energy over the full kinematic range covered by the experiment, we have averaged the 16 and 20 GeV or 17 and 19 GeV yields and present these as approximating the yields from an 18 GeV bremsstrahlung beam. On the scale of the drawings presented, the error introduced by this simple averaging is negligible.

Figures A1-A5 show the measured laboratory yields per equivalent quantum, $\frac{d\sigma}{d\Omega dp}$, of $\pi^{\pm}$, $K^{\pm}$, p, and $\bar{p}$ using a hydrogen target. The data are plotted vs laboratory momentum, and lines have been drawn between points at the same laboratory angle to guide the eye. The error bars shown

include both statistical and estimated systematic uncertainties in the data. In addition to these, there is an overall 6% normalization error uncertainty not shown in the figures.

FIGURE CAPTIONS FOR ADDENDUM

Fig. A1. $\pi^{\pm}$ yields from hydrogen for an 18 GeV incident bremsstrahlung beam.

Fig. A2. K^{+} yields from hydrogen for an 18 GeV incident bremsstrahlung beam.

Fig. A3. K^{-} yields from hydrogen for an 18 GeV incident bremsstrahlung beam.

Fig. A4. Proton yields from hydrogen for an 18 GeV incident bremsstrahlung beam.

Fig. A5. $\bar{p}$ yields from hydrogen for an 18 GeV incident bremsstrahlung beam.

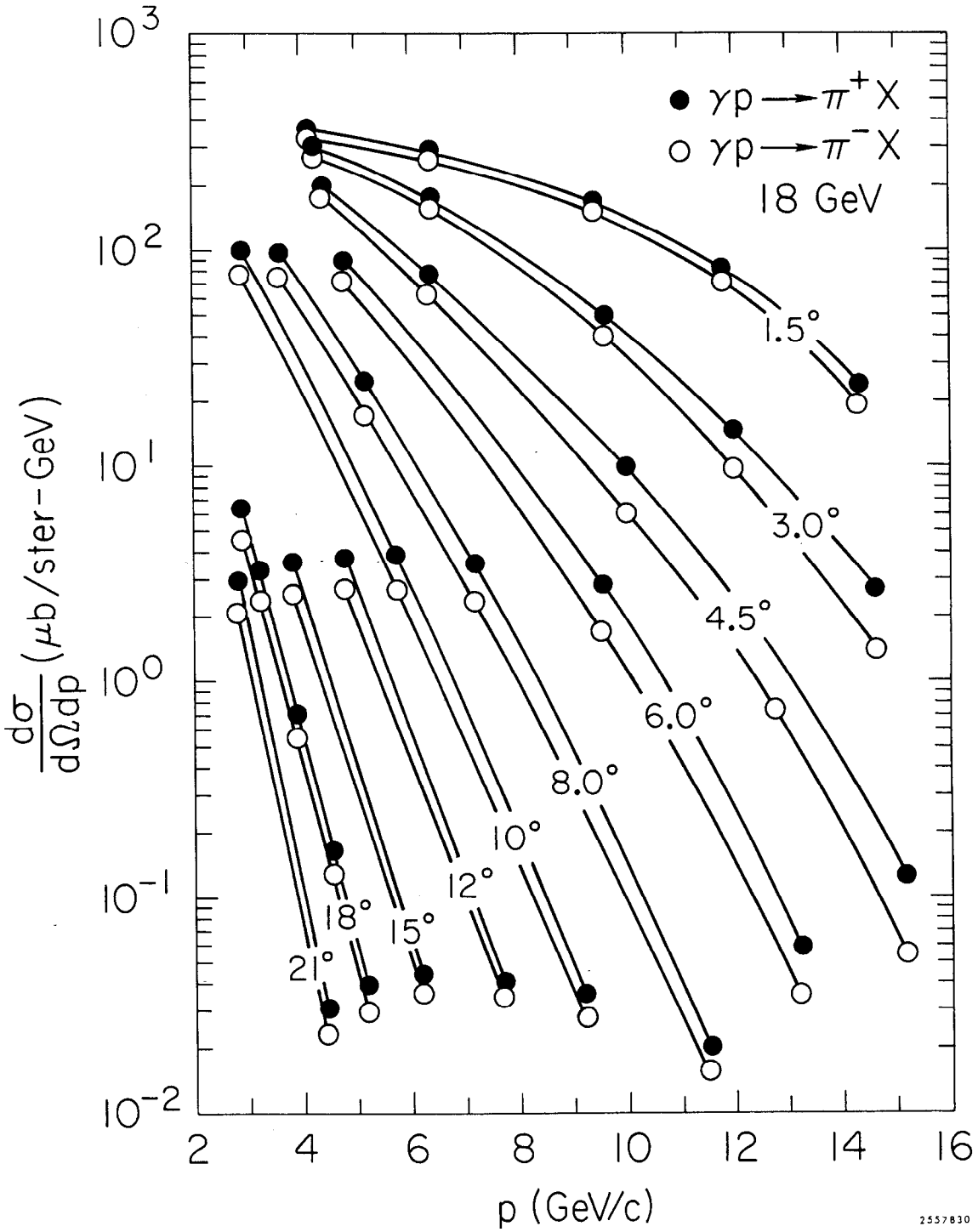
$\gamma p \rightarrow \pi^+ X$
$\gamma p \rightarrow \pi^- X$
18 GeV
1.5°
3.0°
4.5°
6.0°
8.0°
10°
12°
15°
18°
21°
$\frac{d\sigma}{d\Omega dp}$ (μb/ster-GeV)
p (GeV/c)
2557830

Fig. A1

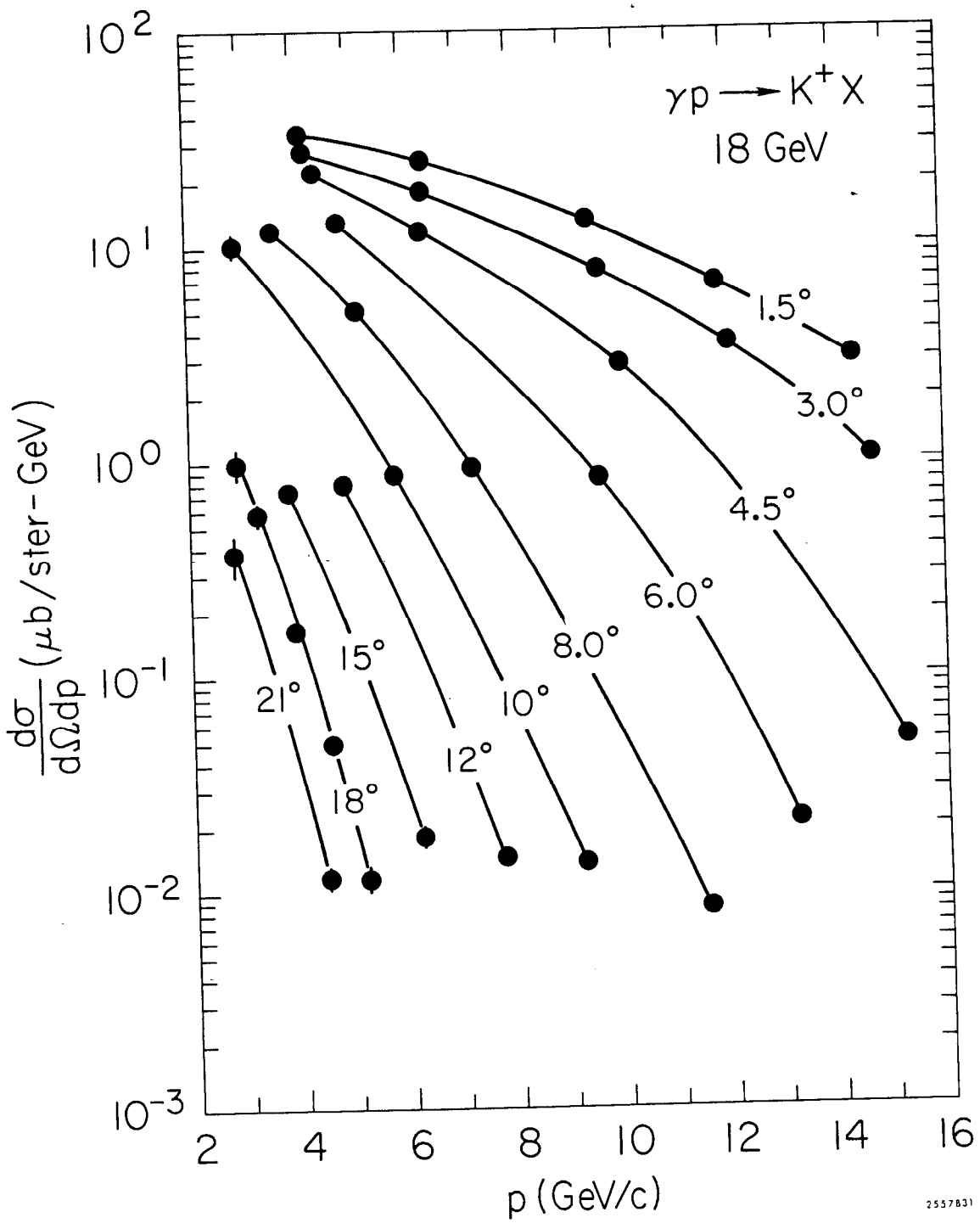
γp → K⁺X
18 GeV
1.5°
3.0°
4.5°
6.0°
8.0°
10°
12°
15°
18°
21°
dσ/dΩdp (μb/ster-GeV)
p (GeV/c)
2557B31

Fig. A2

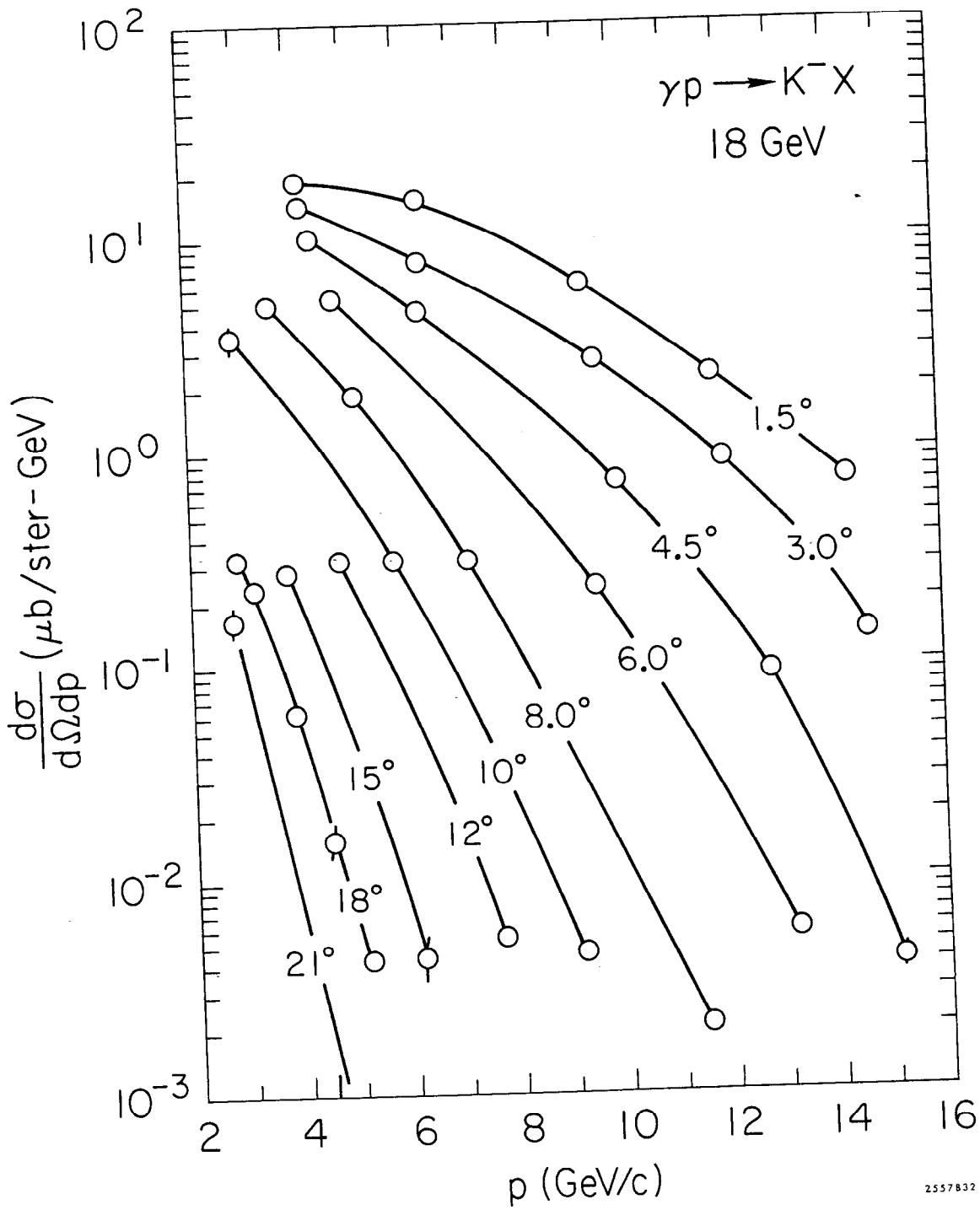
γp → K⁻X
18 GeV
1.5°
3.0°
4.5°
6.0°
8.0°
10°
12°
15°
18°
21°
dσ/dΩdp (μb/ster-GeV)
p (GeV/c)
2557832

Fig. A3

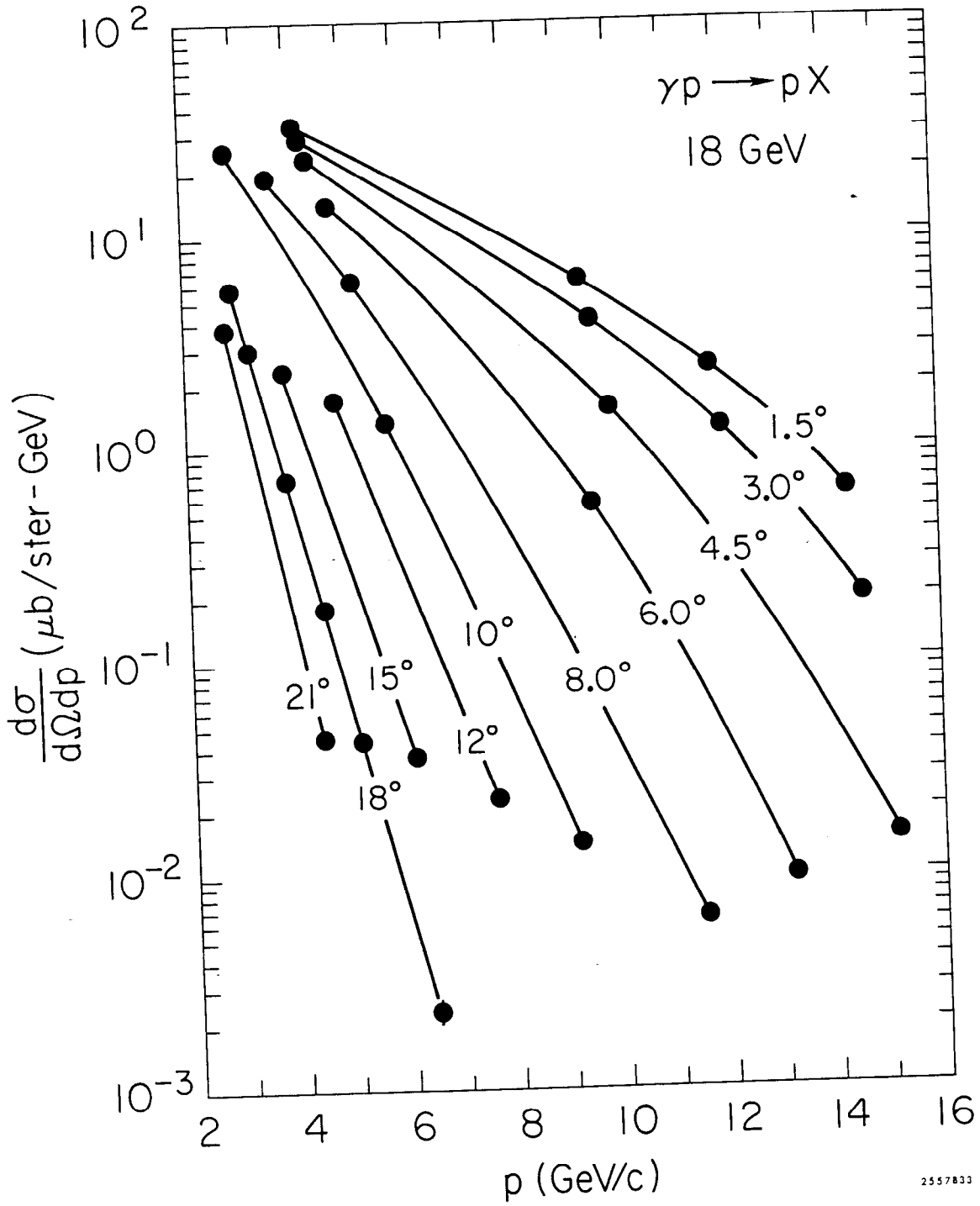
γp → pX
18 GeV
1.5°
3.0°
4.5°
6.0°
8.0°
10°
12°
15°
18°
21°
$\frac{d\sigma}{d\Omega dp}$ (μb/ster - GeV)
p (GeV/c)
2557833

Fig. A4

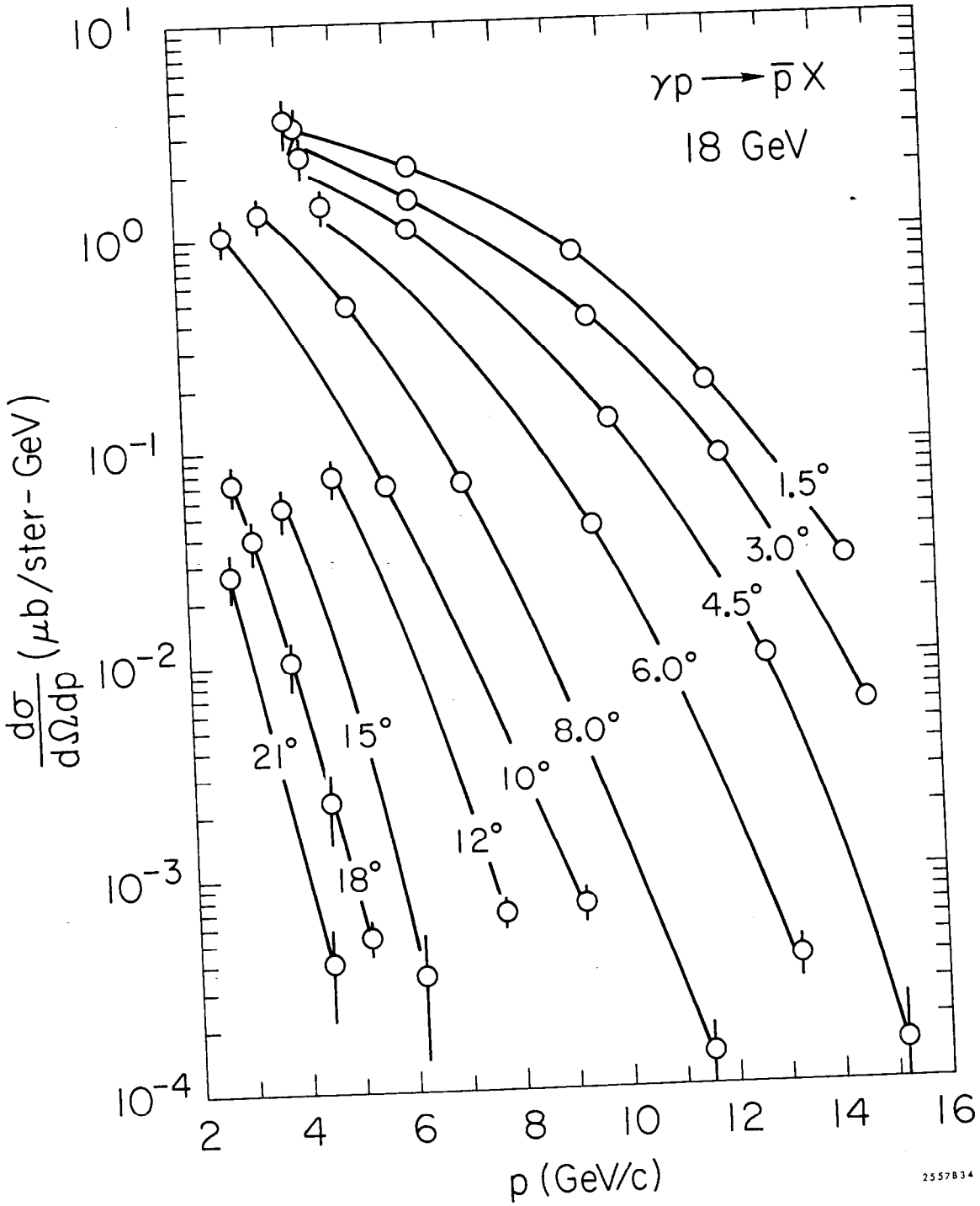
γp → p̄X
18 GeV
1.5°
3.0°
4.5°
6.0°
8.0°
10°
12°
15°
18°
21°
dσ/dΩdp (μb/ster-GeV)
p (GeV/c)
2557B34

Fig. A5